1-1-2012

# Photoacoustic Detection of Red Blood Cell Aggregation

Eno Hysi
*Ryerson University*

# PHOTOACOUSTIC DETECTION OF RED BLOOD CELL AGGREGATION

by

Eno Hysi

B.Sc., Ryerson University, 2010

A thesis

presented to Ryerson University

in partial fulfillment of the

requirements for the degree of

Master of Science

in the Program of

Biomedical Physics

Toronto, Ontario, Canada, 2012

## AUTHOR'S DECLARATION

I hereby declare that I am the sole author of this thesis. This is a true copy of the thesis, including any required final revisions, as accepted by my examiners.

I authorize Ryerson University to lend this thesis to other institutions or individuals for the purpose of scholarly research

I further authorize Ryerson University to reproduce this thesis by photocopying or by other means, in total or in part, at the request of other institutions or individuals for the purpose of scholarly research.

I understand that my thesis may be made electronically available to the public.

ENO HYSI

## ABSTRACT

Photoacoustic Detection of Red Blood Cell Aggregation

Eno Hysi

Master of Science, Biomedical Physics

Ryerson University, 2012

The potential of photoacoustic imaging for detecting red blood cell (RBC) aggregation is explored. Enhanced aggregation is observed in disorders such as diabetes impairing oxygen release into tissue. Simultaneous measurements of aggregation and oxygenation levels cannot be made using current tools. Photoacoustic detection of aggregation and assessment of oxygen saturation was investigated. A theoretical and experimental model of aggregation was developed using human and porcine RBCs. Frequency-domain analysis of the PA signals was used to derive the spectral slope and midband fit of the normalized power spectra for various hematorit and aggregation conditions. Oxygen saturation was assessed using multiple wavelengths of illumination. The experimental spectral slope (~0.3 dB/MHz) for non-aggregated samples agreed with the theory decreasing with increasing aggregate size. The midband fit increased by ~5 dB when the aggregate size reached the largest level while the oxygen saturation increased by > 20%. These results suggest that photoacoustic-radio-frequency-spectroscopic-parameters have the potential to monitor RBC aggregation and oxygenation level.

## ACKNOWLEDGMENTS

This project would have not been possible without the support and encouragement of multiple people. I would like to specifically highlight Dr. Ratan K. Saha for introducing me to theoretical modeling of red blood cells. This project would have simply never started had it not been for his conception of the theoretical model. I am grateful that I had the opportunity to spend many hours with him learning a great deal about the theoretical aspect of this project. Special thanks are due to Dr. Min Rui for introducing me to cell culturing. I would like to acknowledge Dr. Sankar Narasihman for introducing me to photoacoustic measurements. I am very grateful to Drs. Guy Cloutier and Julien Tripette for allowing me to confirm my experimental protocol at the Laboratoire de biorhéologie et d'ultrasonographie médicale. I would like to give special thanks to Jennifer Barry of Sunnybrook Health Sciences Center for providing me with porcine blood. Drs. Raffi Karshafian and Yuan Xu are gratefully acknowledged for being part of my supervisory committee. Their challenging and guiding questions during the committee meetings genuinely helped move this project forward and taught me the importance of being skeptical of your own data at all times. I would also like to thank Dr. Jahan Tavakkoli for acting as the external examiner at my defense and Dr. Juliana Carvalho for chairing the examination. The members of the Kolios Lab (past and present) are recognized for their help and support throughout the years and for creating an enjoyable working environment. I would like to highlight Arthur Worthington for always being an invaluable resource in the lab. In addition I would like to thank all of the faculty members in the Department of Physics that I had the privilege of interacting with during my tenure at Ryerson. I truly believe that choosing Ryerson was one of the best decisions that I have ever made...

I consider myself very fortunate to have had the opportunity to encounter a teacher like Dr. Michael Kolios at the earliest stages of my career. During my 6 years at Ryerson, I had the privilege of spending 4 of them in the presence of someone who for me personally, was an unlimited source

of inspiration. I seldom encountered an individual who had the unique ability to guide and motivate while teaching even the most difficult concepts. Over the years I benefited greatly from his lessons and learned that "back-of-the-envelope" calculations are often all you need to get started. I am thoroughly grateful to him for allowing me to independently advance my projects and ideas even though at times I was destined to hit a block from the start. This has allowed me to build up the necessary confidence to pursue research. Furthermore, I am very thankful that I got the chance to attend many scientific conferences early during this project. I would also like to thank him for supporting my aspirations to get into medical school by giving me the much needed space to study for the MCAT and write numerous letters of recommendations to satisfy the requirements of every school I applied to. I attribute much of my success in that regard to the opportunities that I was given while working with him. I hope to one day to be a tiny fraction of the mentor that he was to me to someone else...

Lastly but most importantly, I would like to acknowledge my parents and brother. I am forever in debt with their constant support, never-ending love and belief in me. I would be nowhere close to typing these words if it wasn't for their sacrifices which granted me the opportunity to pursue my interests in life. This thesis is dedicated to them...

## TABLE OF CONTENTS

AUTHOR'S DECLARATION ..... ii
ABSTRACT ..... iii
ACKNOWLEDGMENTS ..... iv
TABLE OF CONTENTS ..... vi
LIST OF SYMBOLS AND ABBREVIATIONS ..... viii
LIST OF TABLES ..... ix
LIST OF FIGURES ..... x
Chapter 1 INTRODUCTION ..... 1
**1.1 Overview of blood** ..... 1
1.1.1 Plasma ..... 3
1.1.2 Platelets ..... 4
1.1.3 White cells ..... 4
1.1.4 Red cells ..... 5
**1.2 Red blood cell aggregation** ..... 9
1.2.1 Aggregation phenomenon ..... 9
1.2.2 Factors affecting RBC aggregation ..... 10
1.2.3 Mechanism of RBC aggregation ..... 15
**1.3 Methods for measuring RBC aggregation** ..... 19
1.3.1 Erythrocyte sedimentation rate ..... 19
1.3.2 Low-shear viscometry ..... 20
1.3.3 Optical aggregometry ..... 23
1.3.4 Ultrasound imaging ..... 25
**1.4 Impact of RBC aggregation** ..... 30
**1.5 Photoacoustics and its potential** ..... 32
1.5.1 Photoacoustic effect and the generation of photoacoustic signals ..... 32
1.5.2 Propagation of light and sound waves in tissue ..... 35
1.5.3 Applications of PA in medicine ..... 37
1.5.4 US and PA radio-frequency spectroscopy ..... 39
**1.6 Thesis motivation, hypothesis and specific aims** ..... 42
**1.7 Thesis outline** ..... 44

Chapter 2 PA OF RBC AGGREGATION ..... 45
**2.1 Introduction** ..... 45
2.1.1 Theoretical model ..... 45
**2.2 Methods** ..... 47
2.2.1 Simulation methods ..... 47
2.2.2 Experimental methods ..... 48
**2.3 Results** ..... 51
2.3.1 Simulation results ..... 51
2.3.2 Experimental results ..... 53
**2.4 Discussion and conclusions** ..... 55
Chapter 3 ON THE POTENTIAL OF PA-RFS FOR DETECTING RBC AGGREGATION AND OXYGENATION ..... 59
**3.1 Introduction** ..... 59
3.1.1 Theoretical model ..... 59
**3.2 Methods** ..... 61
3.2.1 Simulation methods ..... 61
3.2.2 Blood sample preparation ..... 64
3.2.3 Experimental setup ..... 65
3.2.4 Data analysis ..... 66
3.2.5 Estimation of oxygen saturation ..... 67
**3.3 Results** ..... 67
3.3.1 Simulated power spectra ..... 67
3.3.2 Quantitative parameters for simulated samples ..... 69
3.3.3 Experimental SA and oxygenation level ..... 72
3.3.4 Experimental spectral parameters ..... 73
**3.4 Discussion and conclusions** ..... 74
Chapter 4 CONCLUSIONS AND FUTURE DIRECTIONS ..... 81
**4.1 Thesis conclusions** ..... 81
**4.2 Future directions** ..... 82
REFERENCES ..... 90

# LIST OF SYMBOLS AND ABBREVIATIONS

$P_{O_2}$ = Partial pressure of oxygen

$\tau_{th}$ = Thermal relaxation time

$d_c$ = Characteristic dimension of heated region

$D_T$ = Thermal diffusivity

$\tau_s$ = Stress relaxation time

$v_s$ = Speed of sound

$p$ = Photoacoustic pressure

$\beta$ = Isobaric thermal expansion coefficient

$C_P$ = Heat capacity per unit mass

$H$ = Thermal energy per unit time and volume

$\mu$ = Optical absorption coefficient

$\varpi$ = Modulation frequency of optical beam

$k$ = Wave number

$\hat{q}$ = Dimensionless frequency

$a$ = Radius of absorbing sphere

$\hat{\rho}$ = Dimensionless density ratio

$\hat{v}$ = Dimensionless speed of sound ratio

$\mu_s$ = Optical scattering coefficient

$\mu_s^{'}$ = Optical reduced scattering coefficient

$\phi$ = Fluence rate

$z$ = Depth

$\mu_{eff}$ = Effective optical attenuation coefficient

$\lambda$ = Optical wavelength

$\varepsilon$ = Molar extinction coefficient

$p_{collection}^{NBL}$ = Non band-limited pressure field

$N$ = Number of RBCs

$\vec{r}$ = Observation distance

$\vec{r}_n$ = Position vector of the n$^{th}$ RBC

$p_{collection}^{BL}$ = Band-limited pressure field

$\varpi_0$ = Center frequency of transducer

$\sigma$ = Width of Gaussian function

$R_g$ = Radius of gyration

$H$ = Hematocrit

$Cl$ = Number of RBC clusters

$N_{Cl}$ = Number of RBCs per cluster

$SO_2$ = Oxygen saturation

RBC = Red blood cells
Hb = Hemoglobin
OHb = Oxyhemoglobin
DHb = Deoxyhemoglobin
PBS = Phosphate buffered saline
ESR = Erythrocyte sedimentation rate
LR = Light reflectance
US = Ultrasound
BSC = Backscattering coefficient
SFSE = Structure factor size estimator
W = Clustering degree measure in SFSE
D = Aggregate size measure in SFSE
PA = Photoacoustics
RF = Radio-frequency
ROI = Region of interest
QUS = Quantitative ultrasound
SS = Spectral slope
MBF = Midband fit
UTC = Ultrasound tissue characterization
PA-RFS = Photoacoustic radio-frequency spectroscopy
SA = Signal amplitude
NBL = Non band-limited
BL = Band-limited
h-RBCs = Human RBCs
p-RBCs = Porcine RBCs
[Dex] = Concentration of Dextran-PBS
NAG = Non-aggregatedd
AG = Aggregated

# LIST OF TABLES

Table 1-1: Composition of blood (data collected from [3–5]). ..... 2

Table 1-2: Plasma proteins and their effect on RBC aggregation;↑ promotes aggregation; ↓ inhibits aggregation (adapted from reference [21]). ..... 11

Table 2-1: Physical constants and simulation parameters. ..... 48

Table 3-1: Absorption coefficients for oxygenated and deoxygenated RBCs. ..... 63

Table 3-2: Hematocrit and aggregation levels simulated in this study. ..... 63

Table 4-1: Summary of the SA and spectral parameters (SS and MBF) for the phantom experiments. ..... 87

# LIST OF FIGURES

Figure 1-1: The structure of Hb and the structural formula for heme (adopted from reference [14]). 6

Figure 1-2: The effect of pH on the oxyhemoglobin dissociation curve. The labelled arterial and venous points refer to the partial pressure of oxygen in the arteries and veins at each pH level (adopted from reference [17]). 8

Figure 1-3: A representative sample of human RBCs in autologous plasma showing the presence of rouleaux and non-aggregated cells (adopted from reference [19]). 9

Figure 1-4: Rouleaux formation in the post-capillary venules of a rat mesentery due to the infusion of (A) fibrinogen (0.7% g/g) and (B) dextran-500 (3% g/g) (adopted from reference [31]). 12

Figure 1-5: Effect of dextran molecular mass and concentration on the extent of RBC aggregation (adopted from reference [21]). 13

Figure 1-6: Correlations between plasma and polymer induced aggregation. The polymers used are: 3% Dextran 70 kDa, 0.5% polyvinylpyrrodoline (PVP) 360 kDa, 0.6% poly-l-glutamic acid 62.1 kDa and 6% heparin 17 kDa (adapted from reference [21]). 15

Figure 1-7: Illustration of the macromolecular bridging which brings adjacent RBCs into contact (adopted from reference [21]). 16

Figure 1-8: Schematic of the dynamics of rouleaux formation as postulated by the bridging hypothesis. In this figure, step I shows the macromolecular cross-linking of the two adjacent RBCs which can be enhanced from further bridges as shown in step II. The cells then rotate to allow for maximal area of contact as shown in step III (adopted from reference [21]). 17

Figure 1-9: Schematic of the dynamics of rouleaux formation as postulated by the depletion hypothesis. In step I, the polymers are depleted from the RBC surfaces causing an attraction developed (step II) when the depletion layers (dashed lines) overlap due to solvent displacement into the surrounding medium. The adjacent cells then slide along each other and maximize the loss in free energy (black arrows) eventually forming the close contact that leads to RBC aggregation (step III) (adopted from reference [21]). 18

Figure 1-10: Range of ESR (in mm/hour) as a function of hematocrit for normal RBCs in autologous plasma (adapted from reference [46]). 20

Figure 1-11: Measurement of the viscosity as a function of shear rate for three types of RBC suspensions at 40% hematocrit: RBCs in plasma (i.e. whole blood), RBCs in a protein-free isotonic buffer (saline) and rigid RBCs in an aldehyde fixed solution suspended in the same isotonic buffer. The RBCs in the buffer do not aggregate (adapted from reference [21]). 21

Figure 1-12: Interaction of light beams with (a) non-aggregated and (b) aggregated RBC suspensions. The direction of the arrow indicates the incident light beam direction (adapted from reference [21]). 23

Figure 1-13: The time course of the light reflected from a 300 μm thick blood film placed between two glass cylinders. The arrow indicates the time when the rotating cylinder was stopped (adapted from reference [21]). 24

Figure 1-14: Dependence of (a) W parameter and (b) D parameter (calculated by SFSE) on the shear rate for porcine RBC suspensions (adapted from reference [69]). 28

Figure 1-15: US BSC versus hematocrit for human RBCs under experimental stationary (squares) and stirred (triangles) conditions. The solid line represents the theoretical curve (adapted from reference [73]). 29

Figure 1-16: PA spectral power for two fluid spheres (radius 3 μm and 9 μm) with density and speed of sound ratios of (a) $\hat{\rho} = \hat{v} = 0.5$ and (b) $\hat{\rho} = \hat{v} = 1.0$ 34

Figure 1-17: Molar extinction coefficient of OHb (solid) and DHb (dashed) (adapted from reference [89]). ..... 36

Figure 1-18: Power spectra for (a) the RF signal obtained from tissue and the RF signal obtained from reflection off a glass plate and (b) normalized power spectrum obtained by subtracting the tissue spectrum from the glass plate spectrum and the linear fit over the transducer bandwidth (adapted from reference [112]) ..... 41

Figure 2-1: Effect of [Dex] on the viscosity of the h-RBC samples. The error bars (too small to be seen) represent the standard deviation of the viscosity measurements taken over 1 minute at a constant shear rate. ..... 49

Figure 2-2: Imagio PA imaging system components. ..... 50

Figure 2-3: Representative (a) NAG and (b) AG RBC configurations simulated in this study. For both cases the hematocrit is 40% and for the AG case Rg is 12.24 μm. ..... 51

Figure 2-4: Simulated NBL and BL average spectra for NAG and AG RBCs. The top row shows the h-RBCs spectra and bottom row shows the p-RBCs spectra: (a) + (d) NBL NAG, (b) + (e) NBL AG and (c) + (f) BL AG. ..... 53

Figure 2-5: Experimental SA ((a) h-RBC and (b) p-RBC) and mean spectral power ((a) h-RBCs and (d) p-RBCs). The error bars represent the standard deviation of 20 PA signals and spectra. ..... 54

Figure 2-6: Comparison between the PA SA and viscosity of h-RBCs measured at the lowest shear rate (0.05 $s^{-1}$) for all [Dex] used in this study (0, 1, 3 and 8%). The error bars indicate the standard deviation of 20 PA signals and 1 minute of viscosity measurements at 0.05 $s^{-1}$. ..... 55

Figure 3-1: (a) NAG p-RBCs suspended in PBS and (b) AG p-RBCs suspended in 3% [Dex]. The scale bar denotes 10 μm. ..... 64

Figure 3-2: Simulated power spectra for oxygenated NAG and AG RBC configurations illuminated at 750 nm. Top row: (a) NBL power spectra for NAG RBCs at 3 hematocrit levels, (b) BL and (c) normalized power spectra of (b). Bottom row: (d) NBL power spectra for AG RBCs at 3 aggregation levels and 40% hematocrit, (e) BL and (f) the normalized power spectra of (e). The lines on (c) and (f) represent the usable transducer bandwidth over which linear regression was performed. ..... 69

Figure 3-3: (a) SA, (b) SS and (c) MBF for the 750 nm laser exposure as a function of hematocrit, aggregate size and oxygenation level. The error bars (too small to be seen in (a)) denote the standard deviation for 250 PA signals or spectra. ..... 70

Figure 3-4: (a) SA, (b) SS and (c) MBF for the 1064 nm laser exposure as a function of hematocrit, aggregate size and oxygenation level. The error bars (too small to be seen in (a)) denote the standard deviation for 250 PA signals or spectra. ..... 71

Figure 3-5: Experimentally measured PA SA and $SO_2$ levels for all RBC samples. The error bars denote the standard deviations of 20 PA signals. Top row: PA SA for the (a) 750 nm and (b) 1064 nm exposures. Bottom row: (c) $SO_2$ for all RBC samples illuminated at both wavelengths. ..... 73

Figure 3-6: Experimentally measured SS and MBF for all RBC samples. The error bars denote the standard deviations of 20 PA spectra. Top row: SS for the (a) 750 nm and (b) 1064 nm exposures. Bottom row: MBF for the (c) 750 nm and (d) 1064 nm exposures. ..... 74

Figure 4-1: Representative PA signals for (a) 1 μm and (b) 10 μm black polystyrene phantoms along with (c) average power spectra and (d) normalized power spectra and the respective linear fits .The phantoms shown here had a 0.3% (v/v) bead concentration. ..... 86

# Chapter 1 INTRODUCTION

## 1.1 Overview of blood

The human body is a highly evolved machinery of specialized cells that depend on one another for maintaining homeostasis. Since most cells are implanted firmly into tissues, they must have their oxygen and nutrients delivered to them while their waste products are periodically removed. A highly effective method of transporting materials within the body is required. That is accomplished through a special type of tissue that is blood. Blood is a connective tissue that consists of cells in a liquid extracellular matrix made up of non-living substances [1]. In an average human, 50-60% of the blood volume is composed of the extracellular matrix commonly referred to as plasma. The remainder of the blood volume consists of a variety of cells and cell fragments that are collectively referred to as the formed elements [2]. These include platelets, several types of white blood cells, and red blood cells.

An estimated 97,000 km of vessels throughout the body of an adult ensure that continued nourishment reaches each of the trillions of living cells while maintaining their homeostasis and protection [3]. The functions of blood can be broadly divided into three categories and **Table 1-1** summaries the component responsible for these functions:

a. Transportation: All substances essential for cellular metabolism are transported through blood. These include the respiratory gases that are transported through red cells between lungs and tissues, nutritive products that are absorbed by blood through the intestinal wall and excretory metabolic wastes that are carried by the blood to the kidneys.

b. Regulation: Blood is responsible for carrying hormones from their site of production to distant target tissues. In addition, blood regulates temperature by diverting from deeper to more superficial vessels or vice versa to increase or decrease the heat exchange.

c. Protection: Blood protects itself from loss of volume through the clotting mechanism of platelets and plasma proteins. In addition, white blood cells provide immune protection against foreign pathogens.

| | Component | Concentration | Function |
|---|---|---|---|
| **FORMED ELEMENTS** 40% of blood volume | | Number (volume %) | |
| | Platelets | $1.3\text{-}4 \times 10^5 / mm^3$ (1-3%) | Blood clotting |
| | White cells | $5\text{-}10 \times 10^3 / mm^3$ (0.3-0.5%) | Immune defence |
| | Red cells | $4\text{-}6 \times 10^6 / mm^3$ (35-45%) | Transport $O_2/CO_2$ |
| **PLASMA** 60% of blood volume | Water | 93% of plasma weight | Transport medium |
| | Inorganic ions | <1% of plasma weight | Maintenance of osmotic pressure; buffer; hemostatic system |
| | $Na^+$ | 145 mM | |
| | $K^+$ | 4 mM | |
| | $Ca^{2+}$ | 2.5 mM | |
| | $Mg^{2+}$ | 1.5 mM | |
| | $H^+$ | 0.0004 mM | |
| | $Cl^-$ | 103 mM | |
| | Main Proteins | 7% of plasma weight | Buffer; molecular transport; enzyme precursors; antibodies; hormones |
| | Albumin | 4.2 g/dl | |
| | Globulin | 2.8 g/dl | |
| | Fibrinogen | 0.3 g/dl | |
| | Other molecules | | Cell structure; protein functions; metabolism regulation; energy production |
| | Lipids | <160 mg/dl | |
| | Amino acids | 5.5-8.0 mg/dl | |
| | Carbohydrates | 75-115 mg/dl | |
| | Cholesterol | <200 mg/dl | |

Table 1-1: Composition of blood (data collected from [3–5]).

### 1.1.1 Plasma

Plasma is the straw-colored liquid phase of blood in which the cellular components are suspended. It is a complex solution of biological materials ranging in size from a few tens to millions of Daltons [6]. The solutes in plasma make up 8-9% of plasma by weight with the rest being water. The smallest of the solutes are the ions of the dissolved and dissociated inorganic salts, making up some 1% of the plasma by weight. The most concentrated is $Na^+$, largely derived from dissociated NaCl, thus it is the most important ion from an osmotic point of view. In case the body loses water, the plasma becomes excessively concentrated and its osmolarity increases. This has important consequences in the maintenance of a homeostatic blood pressure [2]. There are potent physiological mechanisms in place to ensure that the concentration of such ions is maintained within normal range. Another important ion is the bicarbonate anion which has an important role in controlling blood pH and maintaining it in a very narrow normal range of 7.38-7.44 which is vital to normal bodily functions [3].

The plasma proteins are all very large with molecular weights ranging from a few tens of thousands to millions of Daltons and making up about 7% of plasma by weight. They are necessary for transporting many vital materials, for the defence against infections and maintenance of hemostasis. For instance, albumins, the most abundant of the plasma proteins, are produced in the liver and provide the necessary osmotic pressure to draw water from the surrounding tissue fluid into the capillaries. Globulins serve as transporters of lipids and fat-soluble vitamins. Fibrinogen, which accounts for only about 4% of the total plasma proteins, is an important clotting factor which during clotting is converted into the insoluble clots of fibrin [7]. As will be discussed later in this chapter, fibrinogen plays a crucial role in the process of red blood cell aggregation. The plasma proteins are also very important from a hemorheological perspective. Due to their relatively high concentration in the plasma, their large size and often asymmetrical shapes, they have a large effect

on plasma viscosity. The normal range for the viscosity of the human plasma is 1.25±0.10 mPa.s at 37°C, while the viscosity of water is 0.69 mPa.s; the difference between the viscosity of water and plasma is almost entirely due to the presence of plasma proteins [8].

### 1.1.2 Platelets

Platelets or thrombocytes, are the smallest of the formed elements of blood. They are colorless, irregularly shaped with diameters of the order of 2-3 μm. They are actually fragments of large cells called megakarocytes, the bone marrow cells responsible for their production during hematopoesis [3]. The platelets enter circulation lacking nuclei and are incapable of moving on their own but are capable of amoeboid movement. Their count per cubic millimetre of blood ranges from 130,000 to 400,000 while it can vary greatly under different physiological conditions [9]. The average lifetime of platelets is about 5 to 9 days before destroyed by the liver and spleen.

The most important role that platelets play in blood physiology is in the formation of blood clots. The majority of the clot's mass is made up of platelets while the phospholipids in their membrane activate the clotting factors in the plasma that lead to the formation of fibrin threads which strengthen the platelet plug [7]. Specifically, during bleeding, platelets disintegrate and release thromboplastin which reacts with prothrombin and calcium to form thrombin. The thrombin then is capable of changing the plasma fibrinogen to fibrin. It is the fibrin which is capable of forming a network that traps the blood cells eventually forming a clot rendering blood incapable of escaping [10]. In addition, platelets also attach together in a clot and release serotonin which simulates constriction of blood vessels reducing the flow of blood to the injured area.

### 1.1.3 White cells

Leukocytes or white cells are the largest of the formed elements of blood but the least abundant. They are all derived from a mutlipotent cell in the bone marrow known as a hematopoietic stem cell

and on average live for about 3-4 days as part of blood and the lymphatic system. Their diameter ranges from 7 to 21 μm [11]. White cells contain nuclei, mitochondria and can move in an amoeboid fashion. The ability to move in this fashion allows them to squeeze through pores in the capillary walls into tissue space in a movement process referred to as extravasation. They are almost invisible under the microscope and are classified only when properly stained. The name "white cells" is derived from the fact that after centrifugation of a blood sample, leukocytes are found in a white layer known as the buffy coat containing a thin layer of nucleated cells. Based on the presence of granules in the cytoplasm which is revealed by eosin and basic staining, leukocytes are divided into granular and agranular leukocytes [2]. Granular leukocytes are made up of neutrophils, eosinophils and basophils while agranular leukocytes include lymphocytes and monocytes.

White cells are part of the immune system and their main functions are carried inside tissue rather than the bloodstream. They have evolved specialized adhesive and migratory capabilities to allow for their recruitment from the blood across the vascular endothelium into tissue in the presence of infection [12]. The leukocytes work together to prevent disease by actually destroying the invading bacteria, viruses or parasites through phagocytosis and by forming antibodies and sensitized lymphocytes which may destroy or inactivate the invader. In the presence of infection in tissue, the leukocyte count can increase from the average of 8,000/$mm^3$ of blood to more than 25,000/$mm^3$ [1].

### 1.1.4 Red cells

Red blood cells (RBCs) or erythrocytes are the most abundant of the formed elements of blood. They are shaped like disks, both sides of which are concave and have a diameter of about 7 μm with a thickness of approximately 2.2 μm. Their short circulating life span of ~120 days is attributed to a lack of nucleus and mitochondria forcing the RBCs to obtain energy through anaerobic respiration

[2]. RBCs are produced by the red marrow of bones such as the ribs, vertebrae, femur (in developing children) and skull. During development, RBCs do contain a large nucleus and are colorless. By the time they are ready to be released into the blood stream, they lose their nuclei. At the end of their life cycle, the red cells are destroyed by the liver or the spleen thus releasing valuable components into the blood stream which are used in the manufacturing of new RBCs [3].

As RBCs mature and lose their nucleus, they become filled with about 280 million of the oxygen-carrying molecule hemoglobin (Hb) [13]. Hb is a protein that consists of four polypeptide chains called globins and four iron-containing, disc shaped organic pigment molecules called hemes. Each of the four polypeptides is composed of two identical alpha chains (each 141 amino acids long) and two identical beta chains (each 146 amino acids long). The heme group is bound to each of the polypeptide chains. The center of each heme group has one atom of iron which can combine with one molecule of oxygen. **Figure 1-1** shows the structures of Hb and the heme group:

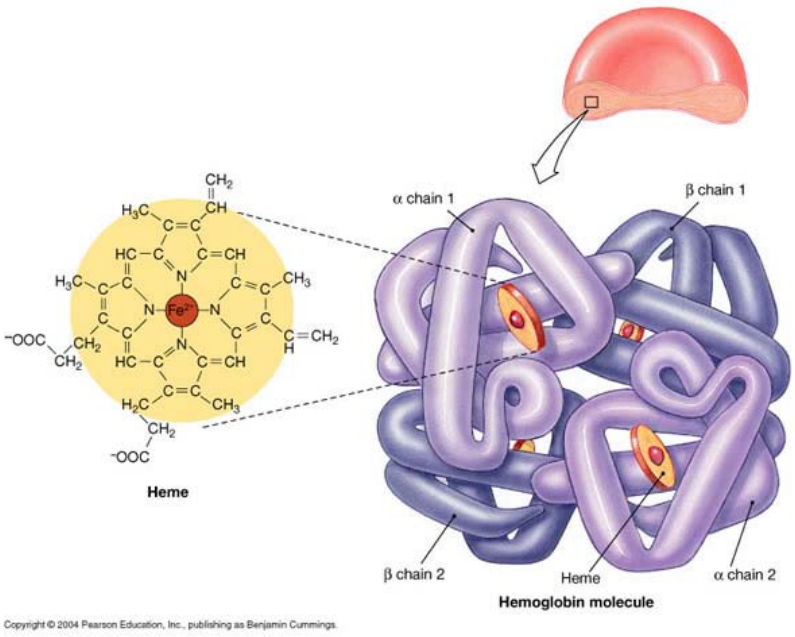


Figure 1-1: The structure of Hb and the structural formula for heme (adopted from reference [14]).

Depending on the state of the iron atom in the center of the heme groups, four forms of Hb have been identified [15]. The two normal states are oxyhemoglobin (OHb) and deoxyhemoglobin (DHb). When iron is in its reduced form, $Fe^{2+}$, it can share electrons and bind with oxygen to form OHb. This is known as the loading reaction and occurs in the lungs. The dissociation of oxygen from Hb leads to the formation of DHb. This is known as the unloading reaction and occurs in systemic capillaries. In addition, Hb also has two abnormal states, methemoglobin and carboxyhemoglobin. If Hb becomes oxidized, it is called methemoglobin with iron in an oxidized state ($Fe^{3+}$). In carboxyhemoglobin, the reduced heme is combined with carbon monoxide instead of oxygen. This form of Hb is particularly more dangerous if it occurs in excess since carbon monoxide can form a bond with Hb that is about 210 times stronger than the bond with oxygen leading to reduced oxygen transport to tissues.

The loading and unloading reactions can be shown as a reversible reaction:

$$DHb + O_2 \underset{\text{Tissue}}{\overset{Lungs}{\rightleftharpoons}} OHb \qquad (1\text{-}1)$$

The extent to which this reaction will go in each direction depends on the environmental partial pressure of oxygen $(P_{O_2})$ and on the bond strength between Hb and oxygen [1]. High $P_{O_2}$ will drive the equation to the right so that almost all DHb at the pulmonary capillaries can combine with oxygen. In the systemic arteries, blood has a percent OHb saturation of 97% (which means that 97% of the Hb is in the form of OHb) at a $P_{O_2}$ of 100 mmHg. In tissues, the $P_{O_2}$ levels are about 40 mmHg and it is this partial pressure difference that drives the unloading of $O_2$ from the OHb to tissue through diffusion. In addition to the changes in $P_{O_2}$, the loading and unloading reactions are influenced by the affinity of Hb by oxygen which is pH dependent [16]. The affinity is decreased when the pH is lowered and increased when the pH is increased; this is called the Bohr Effect.

When the affinity of Hb for oxygen is lowered, there is slightly less loading of the blood with oxygen in the lungs but greater unloading of oxygen in tissue with the net effect that tissues receive more oxygen when the blood pH is lowered. This oxygen loading and unloading ability of Hb as a function of pH can be illustrated graphically through the oxyhemoglobin dissociation curve (**Figure 1-2**), a sigmoid shaped curve that plots the percent saturation of Hb as a function of $P_{O_2}$:

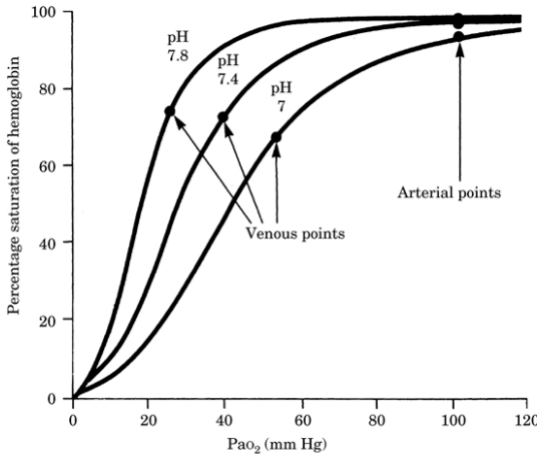


Figure 1-2: The effect of pH on the oxyhemoglobin dissociation curve. The labelled arterial and venous points refer to the partial pressure of oxygen in the arteries and veins at each pH level (adopted from reference [17]).

In addition to transporting and delivering of oxygen, RBCs also participate in the transport of carbon dioxide ($CO_2$) [18]. The majority of $CO_2$ (70%) produced by cellular respiration in tissue enters RBCs where it reacts with water to form carbonic acid. The build-up of carbonic acid inside RBCs favours its dissociation into protons and bicarbonate ions. The protons combine with deoxyhemoglobin while the bicarbonate is released into the plasma. The remainder of $CO_2$ (20%) binds to hemoglobin to form carbinohemoglobin or remains dissolved in the plasma (10%). In the lungs, oxygen enters the RBCs, converting DHb to OHb forcing the bound protons to be released within the RBC. This causes the bicarbonate from plasma to enter the RBC and form carbonic acid which is then converted to $CO_2$ and water causing the release of $CO_2$ into lungs.

## 1.2 Red blood cell aggregation

### 1.2.1 Aggregation phenomenon

The predisposition of RBCs to align against one another face-to-face and form linear structures that resemble a stack of coins is known as RBC aggregation. The individual linear stack of RBCs is referred to as rouleau (plural: rouleaux). A representative collection of rouleaux for normal human RBCs suspended in autologous plasma is shown in **Figure 1-3**:

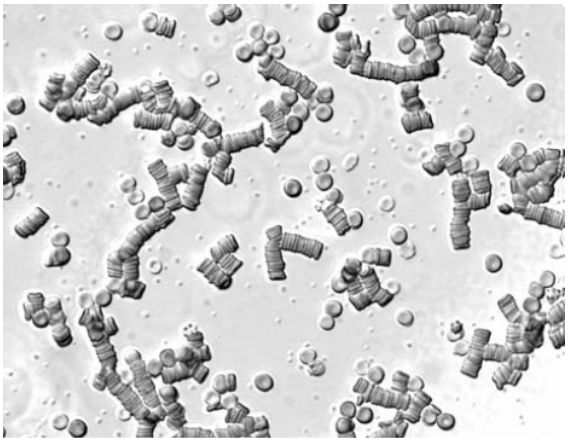

Figure 1-3: A representative sample of human RBCs in autologous plasma showing the presence of rouleaux and non-aggregated cells (adopted from reference [19]).

The number of RBCs per rouleax varies and that complex branching patterns can occur. While the rouleaux are represented in a 2D configuration in a microscope slide, it is possible to have clusters of rouleaux form under appropriate conditions [20]. It is important to note here that RBC aggregation refers to the process during which individual RBCs form rouleaux while RBC aggregability refers to the intrinsic tendency of RBCs to form aggregates. Aggregability is a cellular property which can be affected by several physiochemical factors. A mere measure of RBC aggregation as presented in **Figure 1-3** does not provide a basis for judging aggregability [21]. Furthermore, it is noteworthy to distinguish between RBC aggregation and blood coagulation, conditions that are confused due to the fact that fibrinogen is a major determinant in both. During

coagulation, fibrinogen remains insoluble in the plasma while it is entirely dissolved during RBC aggregation [22].

### 1.2.2 Factors affecting RBC aggregation

Observational studies on the occurrence of RBC aggregation suggest that aggregation is caused due to the presence of various macromolecules found in the plasma of whole blood. In addition, aggregation can also be induced with suspending media made out of solutions of high molecular mass water-soluble polymers such as dextran, polyethylene glycol or polyvynilpyrrolidone but cannot occur if the RBCs are suspended in simple salt solutions such as phosphate buffered saline (PBS) [23]. Despite these well-known suspending-medium requirements for RBC aggregation, it is also known that cell-specific factors influence the process. The later arises from comparisons of the extent of RBC aggregation in various populations in a well defined medium [24]. In addition, the biconcave shape of the RBCs is an important factor for the formation of rouleaux. Deviations from this shape resulting from isovolumic shape changes towards a creneated form (echinocytes) leads to abnormal and even abolished aggregation behaviour. This is seen with camelid RBCs which exhibit almost no aggregation and with cells undergoing shape changes due to osmotic pressure [25]. The hematocrit (volume fraction of RBCs in a suspension) also affects the aggregation processes. A greater number of cells leads to higher frequency of contact between adjacent RBCs. This eventually leads to increased aggregation time course [26].

RBC aggregation is thus the result of the forces that oppose aggregation and those that promote it. While the promoting forces (i.e. mechanisms of aggregation) are yet not well understood (section 1.2.3), the disaggregating forces are easier to define. One of these forces arises from the shear stresses that RBCs aggregates experience during flow. The presence of the shear forces created during flow disrupts existing RBC aggregates. For instance, non-pathologic blood aggregates are dispersed when subjected to rates higher than 20-40 $s^{-1}$ [27]. In addition, the net negative surface

charge density of RBCs prevents them from forming aggregates due to electrostatic repulsion. Finally, the strain of their membranes prevents the deformation of RBCs thus not allowing them to form an area of close contact which is required for aggregation [28]. Therefore, aggregation is modulated by both the suspending phase (medium) and the properties of the RBC itself.

The role of several types of macromolecules has been investigated for determining RBC aggregation. Proteins found in the blood plasma seem to have a significant impact on inducing RBC aggregation. Fibrinogen is generally accepted as the plasma protein that most contributes towards causing aggregation. With a physiological plasma concentration of ~150-300 mg/dl, fibrinogen is an acute phase protein whose concentration is enhanced during several cardiovascular diseases or inflammation [29]. As a result, fibrinogen has been shown to affect essentially all aspects of RBC aggregation from the size of aggregates to the viscosity of aggregated suspensions [30]. In addition to fibrinogen, several other large plasma proteins are known to affect RBC aggregation. These proteins and their effects on RBC aggregation are summarized in **Table 1-2**:

| Plasma protein | Molecular weight (kDa) | Plasma concentration (mg/ml) | Effect on aggregation |
|---|---|---|---|
| Fibrinogen | 340 | 1.5-3.0 | ↑ |
| Immunoglobulin G | 150 | 8 | ↑, no effect |
| Immunoglobulin M | 900 | 1.5 | ↑ |
| C-reactive protein | 25 | <0.01 | ↑ |
| Transferrin | 80 | 2.0-3.6 | no effect |
| Haptoglobin | 38 | 0.5-2.5 | ↑, no effect |
| Ceruloplasmin | 151 | 0.2-0.4 | no effect |
| $\alpha_1$-acid glycoprotein | 40 | 0.5-1.0 | ↑, no effect |
| Albumin | 66 | 20-50 | ↑, ↓, no effect |

Table 1-2: Plasma proteins and their effect on RBC aggregation; ↑ promotes aggregation; ↓ inhibits aggregation (adapted from reference [21]).

Even though the effect of most plasma proteins on RBC aggregation has been identified, there are several contradicting reports. This suggests that the aggregation process represents a complex

interaction between the various plasma components and the membrane of the RBCs for determining if a protein induces or prevents aggregation.

Dextran is a non-naturally occurring, neutral polyglucose that has a significant impact on the formation of RBC aggregation. This is shown in **Figure 1-4** which compares the *in-vivo* RBC aggregation induced from fibrinogen and dextran:

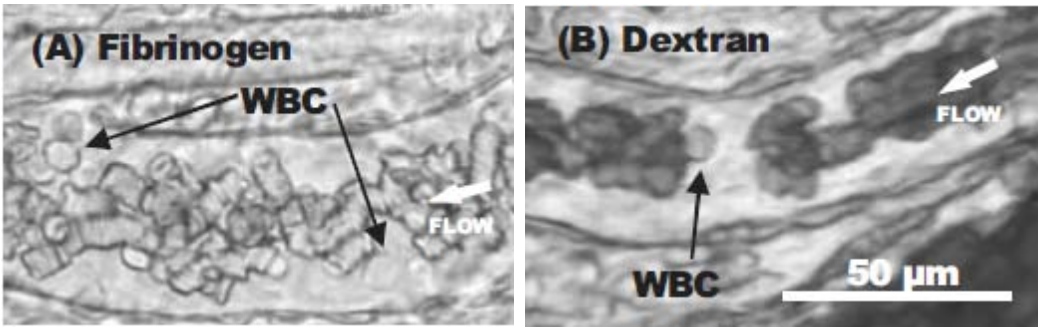


Figure 1-4: Rouleaux formation in the post-capillary venules of a rat mesentery due to the infusion of (A) fibrinogen (0.7% g/g) and (B) dextran-500 (3% g/g) (adopted from reference [31]).

It is clear that dextran is capable of inducing similar rouleaux clusters as is fibrinogen. The molecular mass of dextran is reported to heavily influence the occurrence/inhibition of aggregation. Dextran with molecular mass over 40 kDa induces aggregation while below this threshold it either has no effect on RBC aggregation or it reduces or inhibits the formation of rouleaux [32], [33]. Dextran is probably the most widely studied aggregant and two basic features of the effect of dextran on RBC aggregation are noticed: the extent of aggregation exhibits biphasic behaviour with dextran concentration and increases with dextran molecular mass [34]. The estimated degree of aggregation of normal RBCs induced by dextran as a function of molecular mass and concentration is shown in **Figure 1-5**:

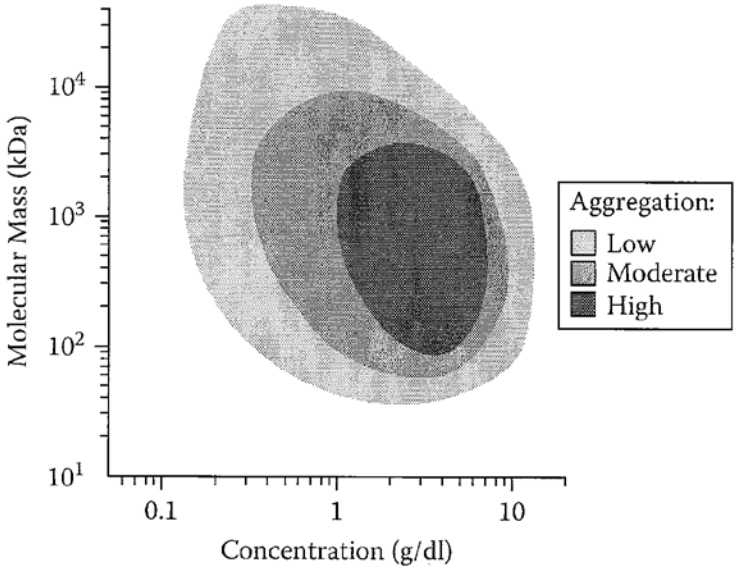


Figure 1-5: Effect of dextran molecular mass and concentration on the extent of RBC aggregation (adopted from reference [21]).

In this thesis, dextran with molecular weight of 70 kDa will be used to induce aggregation. In addition to dextran, a wide range of other polymers are capable of inducing RBC aggregation. This list includes polyhemoglobin, gelatine, ficoll, starches, polyethylene glycol, polyvinylpyrrolidone and various poloxamers [21]. While most of these molecules have very little in common, a general trend among them is that the ones with relatively high molecular masses induce aggregation while the low molecular mass species of the same polymer have no effect or even inhibit aggregation. It was also reported that the hydrodynamic size (radius) of the polymer can better classify which polymers are capable of inducing aggregation [35]. This study concluded that despite different structures, polymers with a hydrodynamic radius less than 4 nm inhibit aggregation while those with a radius greater than 4 nm promote aggregation.

While most studies have focused on the effect of the suspending phase macromolecules on RBC aggregation, accumulating evidence suggests that physical and biochemical attributes of the RBCs play an equally important role in the aggregation process. The first observation in this area reported that the age of the RBCs affects the degree of aggregation: older cells exhibit greater

aggregation than younger cells [36]. It is now well known that older cells decrease their levels of membrane sailic acid which contributes to the RBC surface charge density.

Moreover, differences in RBC aggregability were found between various healthy donors in both autologous plasma and solutions of 3% dextran-70 [28]. The study compared the degree of aggregation in each suspending medium between donors and found a large twofold range in the extent of aggregation in dextran solutions and a fivefold range in autologous plasma. These findings suggest that the cell and medium properties significantly contribute to the large range in the degree of aggregation of autologous plasma.

When clinical measurements of RBC aggregation are conducted, almost always whole blood or RBC-plasma suspensions are employed. Since changes in the aggregability of the RBCs from clinical conditions are reported, it is commonly believed that these alterations are due to the cell-specific changes that occur during the condition. Some of the clinical disorders where RBC aggregability has been reported to increase for RBCs suspended in polymer suspensions are: myocardial infarction, bacterial infection, type 2 diabetes, pregnancy-induced hypertension, normal tension glaucoma and sickle cell disease [21]. A more thorough discussion of the clinical conditions that impact RBC aggregation will be presented in section 1.4.

In order to demonstrate the significance of the cellular factors on RBC aggregation, Whittingstall and colleagues investigated RBC aggregation in isotonic suspensions of four different polymers that were known to induce aggregation [37]. The degree of aggregation (assessed by optical aggregometry, see section 1.3.3) was then compared to the autologous plasma for each sample and the correlation coefficient was computed as shown in **Figure 1-6**:

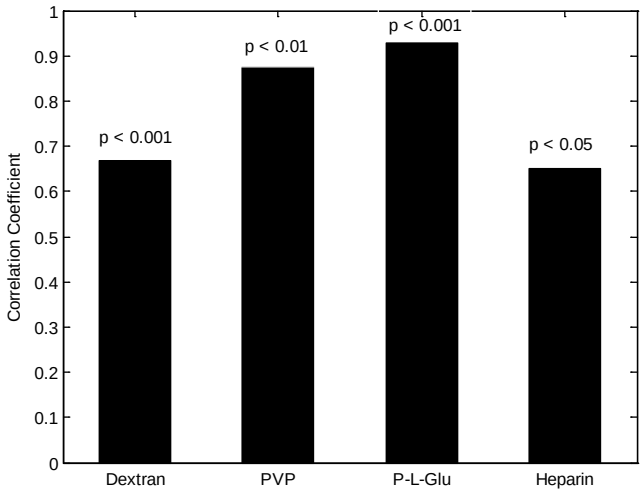


Figure 1-6: Correlations between plasma and polymer induced aggregation. The polymers used are: 3% Dextran 70 kDa, 0.5% polyvinylpyrrodoline (PVP) 360 kDa, 0.6% poly-l-glutamic acid 62.1 kDa and 6% heparin 17 kDa (adapted from reference [21]).

It is clear that regardless of the polymer size and charge, the polymer induced aggregation correlated well with the aggregation induced by the autologous plasma. This finding suggests that there is minimal dependence on the nature of the aggregant but rather strong dependence on the cellular factors of the RBCs. It is worth noting that these results cannot be observed when the aggregant either inhibits aggregation or produces extremely weak or strong aggregates since the sensitivity to subtle cellular changes is then reduced [21].

### 1.2.3 Mechanism of RBC aggregation

The previous chapters outlined the general agreement that exists between the elevated levels of fibrinogen or other large plasma proteins, the effects of the molecular mass and concentration of neutral polymers and the degree of RBC aggregation. In addition, cellular factors play an important role in RBC aggregability. However, to date, the exact mechanism responsible for the formation of RBC aggregates is not clear. Two seemingly contradicting hypotheses have been proposed to explain RBC aggregation, the bridging hypothesis and the depletion hypothesis.

The bridging hypothesis proposes the cross-linking of large macromolecules (i.e. plasma proteins) at the binding sites on adjacent RBCs as the potential mechanism for the formation of RBC aggregates [38]. If these bridging forces (due to the adsorption of macromolecules onto adjacent cells) exceed the disaggregation forces (due to electrostatic repulsion or mechanical shearing), RBCs will successfully aggregate. Measurements of the intracellular distance between adjacent cells have shown that the separation is less than the size of the macromolecule used to induce aggregation [39]. This is shown in **Figure 1-7**:

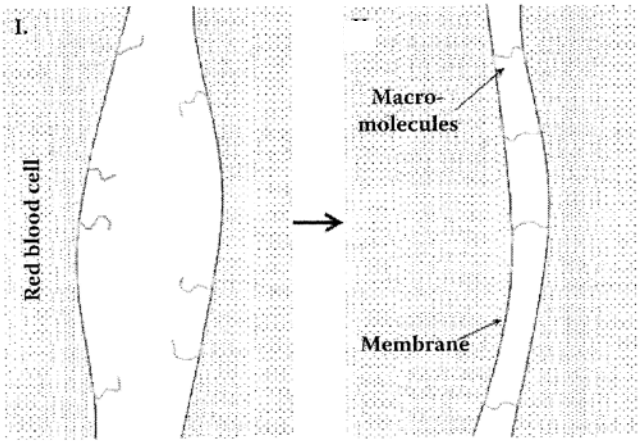


Figure 1-7: Illustration of the macromolecular bridging which brings adjacent RBCs into contact (adopted from reference [21]).

According to this model, the interaction between adjacent cells is formed due to the adsorption of the terminal end of the polymer onto the surface of each cell. The separation distance between adjacent RBCs increases with increasing polymer size but always remains smaller than the diameter of the polymer [40]. Furthermore, the bridging hypothesis also speculates on the dynamics of the rouleaux formation. It is assumed that two RBCs which have formed the cross-links in a few locations can form further bridges once in close proximity. Since the cells deform easily, they are capable of rotating and thus maximizing the area of close contact eventually forming rouleaux. This is demonstrated in a step-by-step process shown in **Figure 1-8**:

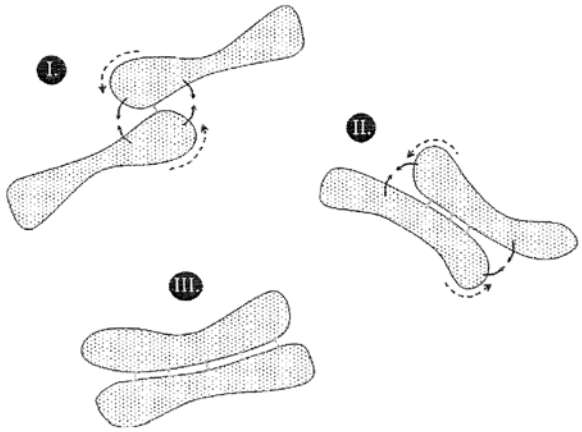


Figure 1-8: Schematic of the dynamics of rouleaux formation as postulated by the bridging hypothesis. In this figure, step I shows the macromolecular cross-linking of the two adjacent RBCs which can be enhanced from further bridges as shown in step II. The cells then rotate to allow for maximal area of contact as shown in step III (adopted from reference [21]).

The bridging hypothesis has been supported from studies which examined the effect of the dextran mass on the separation distance between adjacent cells. For instance, Chien and Jan measured the separation distance for RBCs aggregated with dextran 40 kDa and found it to be 19 nm while for dextran 2000 kDa the distance was 32 nm [32]. This is in expected since larger dextran molecules would cross link the cells with greater separation. The quantification of the binding of the macromolecule onto the RBC surface has also been used as support for the bridging hypothesis however the technique is quantitatively difficult to interpret due to artifacts such as the trapped fluid between cells which affects the measurement of polymer adsorption [41].

The depletion hypothesis proposes a mechanism of RBC aggregation which is opposite to the one proposed in the bridging hypothesis. In this model, the aggregation of RBCs is explained by the presence of polymers but without the requirement for surface adsorption [42]. Specifically, the concentration of the polymer near the cell surface is decreased compared to the suspending medium when a loss of configurational entropy is not balanced by positive interaction energy (i.e. adsorption). This results in the formation of a polymer depletion layer around the RBC where the polymer density decreases towards the surface. As a consequence, there is a decrease of osmotic

pressure between the intercellular polymer-poor depletion zone and the suspending medium which leads to the depletion interaction and the formation of an attractive force that tends to minimize the polymer-poor phase between the cells. Eventually, this results in rouleaux formation as shown by **Figure 1-9**:

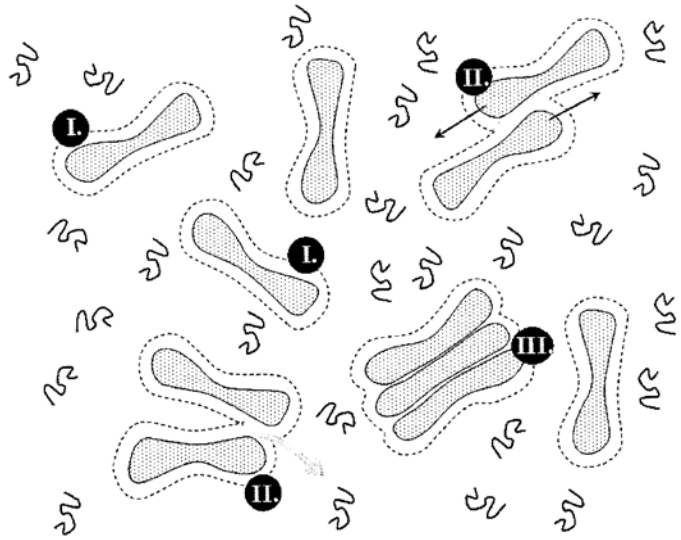


Figure 1-9: Schematic of the dynamics of rouleaux formation as postulated by the depletion hypothesis. In step I, the polymers are depleted from the RBC surfaces causing an attraction developed (step II) when the depletion layers (dashed lines) overlap due to solvent displacement into the surrounding medium. The adjacent cells then slide along each other and maximize the loss in free energy (black arrows) eventually forming the close contact that leads to RBC aggregation (step III) (adopted from reference [21]).

The difficulty in measuring the cross-linking between adjacent cells (which would support the bridging hypothesis) has prevented the experimental confirmation of the two competing hypotheses. Recently, several reports favoring the depletion hypothesis have been published [35], [42]. The theoretical model for depletion has been developed allowing the estimation of the depletion layer thickness as a function of polymer concentration, adhesion energy and electrostatic repulsion between RBCs. Particle electrophoresis has been used as means for experimentally quantifying the depletion layers around RBCs. General agreement between the model and experiments suggests that RBC aggregation is induced via a macromolecular depletion interaction [43].

## 1.3 Methods for measuring RBC aggregation

A number of techniques have been developed for assessing various aspects of the aggregation process. Depending on the technique, a specific aspect of RBC aggregation can be assessed such as the extent of aggregation or the time course of rouleaux formation. The techniques described here include: erythrocyte sedimentation rate, low-shear viscometry, optical aggregometry techniques and ultrasound imaging.

### 1.3.1 Erythrocyte sedimentation rate

As early as the 1890's it was observed that the rate of separation of RBCs from the plasma was increased in the blood of patients of various diseases when compared to healthy people. In addition, the magnitude of the increase determined the severity of the disease [21]. This led to the development of the erythrocyte sedimentation rate (ESR) which is now accepted as a non-specific indicator of inflammation. The ESR is a frequently used laboratory test and its results are interpreted in terms of the presence and severity of inflammation [21]. The measurement procedure involves anti-coagulated blood loaded into 300 mm tubes with inner diameter of 2.55 mm. The height of the plasma column that is RBC-free is read after 1 hour of blood settling. The normal range of ESR depends on gender and is typically higher in females (10 mm/hour for males and 12 mm/hour for females at 45% hematocrit) [44]. During RBC aggregation, the sedimentation rate is determined by the viscous fluid drag that is exerted on the particle (i.e. larger drag, smaller ESR) and the density of the RBCs. The drag is proportional to the surface area of the particles and since the overall surface area of the aggregates is smaller than the sum of the areas of individual RBCs making up the aggregate, the viscous drag decreases. This leads to the increase of ESR with increasing aggregation rate [45]. However, there are multiple factors which affect the ESR such as the mean cell volume and hematocrit. The cell volume affects the density of the cells which in turn affects the buoyancy and eventually ESR. The hematocrit a very important factor because if the hematocrit is low there is

less interaction between the cells leading to fewer aggregates. The relationship between ESR and hematocrit is shown in **Figure 1-10**:

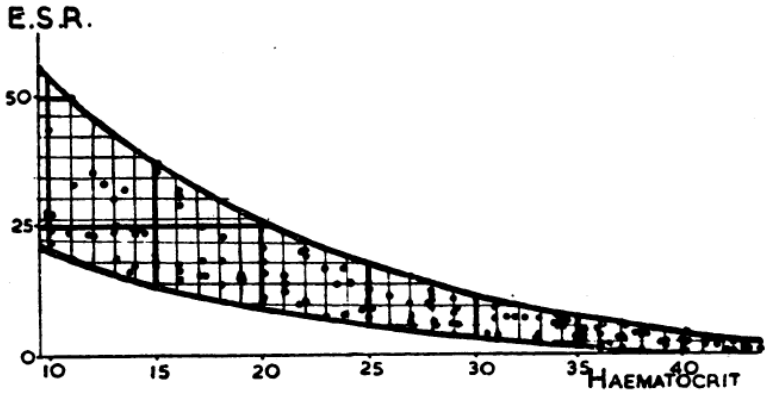


Figure 1-10: Range of ESR (in mm/hour) as a function of hematocrit for normal RBCs in autologous plasma (adapted from reference [46]).

The strong dependence on the hematocrit renders the ESR unable to differentiate between RBC aggregation and other conditions like anemia which have a strong hematocrit dependence [47]. In addition, the ESR measurement is time consuming requiring at least 1 hour which makes the technique impractical for rapid assessments of aggregation. Furthermore, the technique is limited by its ability to only provide an estimate of the degree of aggregation without providing information about the time course of the process which is believed to occur within minutes [48].

### 1.3.2 Low-shear viscometry

One of the most direct ways of demonstrating the effects of RBC aggregation on blood flow is to compare the flow behavior of a suspension containing aggregates (i.e. plasma) with one free of aggregates such as washed RBCs in protein-free isotonic buffer. This is shown from measuring the viscosity of RBC suspensions as a function of the shear rate as shown in **Figure 1-11**:

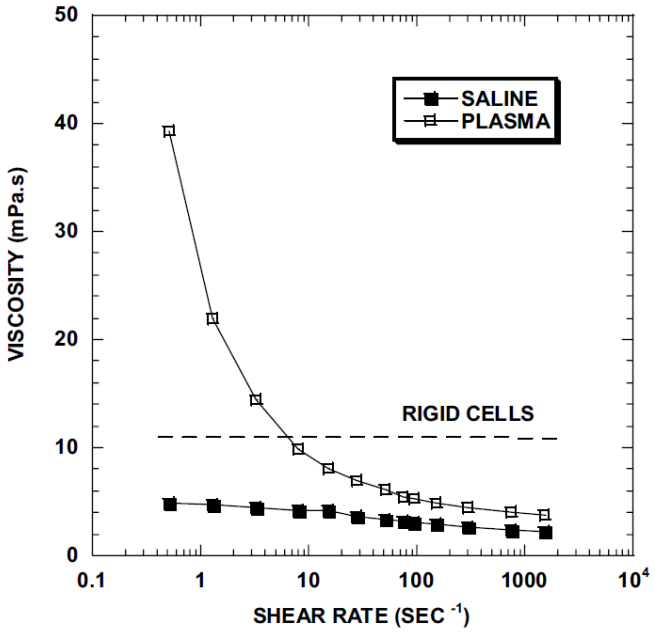


Figure 1-11: Measurement of the viscosity as a function of shear rate for three types of RBC suspensions at 40% hematocrit: RBCs in plasma (i.e. whole blood), RBCs in a protein-free isotonic buffer (saline) and rigid RBCs in an aldehyde fixed solution suspended in the same isotonic buffer. The RBCs in the buffer do not aggregate (adapted from reference [21]).

It is evident from the figure that shear rate has a clear effect on the viscosity of the suspensions. In the presence of RBC aggregation (i.e. RBCs suspended in plasma), the viscosity is increased by almost 11 fold at low shear compared to the high shear rates where the aggregates disperse leading to the viscosity curve approach the buffer suspension curve. The rigid cells are unable to form aggregates and do not deform in response to shear forces leading to a constant viscosity-shear rate relationship [49].

The results presented in **Figure 1-11** demonstrate that RBC aggregation is the main determinant of blood viscosity at low shear rates. For this reason, viscometry at low shear rates has been used as a method to assess the aggregation properties of suspensions of RBCs. The viscometer systems are capable of covering low ranges of shear rates ($< 1\ s^{-1}$) [50]. Two basic classes of instruments are commonly used in blood rheology studies: those in which blood is sheared by a moving surface such as a rotating cylinder or cone and those in which blood is flowed past

stationary walls commonly referred to as tube viscometers. One of the most commonly used rotating cylinder systems is the Couette viscometer where the blood is subjected to laminar and steady shear. The driving principle behind such a system is that the torque required to turn an object in contact with a fluid which is a function of the fluid viscosity. The inner or outer cylinder is rotated at a given rate and the shear stress is transmitted through the fluid in the gap with the resulting torque usually measured at the stationary cylinder [21]. For tube viscometers, the flow is measured at one or more pressure gradients and the pressure-flow data is used to obtain a term reflecting viscosity [51].

Despite the fact that the aggregation indexes based on low-shear viscometry calculations correlate well with the presence of aggregation quantified using other methods, there are several measurement conditions that affect the accuracy. The technique works well when the alterations in RBC aggregation due to changes in the suspending medium composition do not affect the morphology and deformability of RBCs [52]. When the deformability of RBCs is artificially altered (thus reducing RBC aggregation), the low-shear viscometry measurements are not capable of detecting the resulting alterations in RBC aggregation. This renders the interpretation of the results dependent on the suspending medium properties [53]. In addition several potential artifacts can affect the measurement process. The presence of plasma proteins in blood can form a film at the fluid-air interface since they are surfactants. The mechanical strength of this layer is capable of generating significant torque on the torque-measuring element of the viscometer thus affecting the viscosity measurements [54]. Furthermore, time-dependent sedimentation effects have been shown to affect the measurement since the separation of the RBCs from the plasma can change the torque of the measuring element at low shear rates where the aggregation is typically assessed [21].

### 1.3.3 Optical aggregometry

This family of techniques is based on the recognition that the interaction of light with blood is primarily determined by RBCs [55]. Light beams are either absorbed or reflected (i.e. backscattered) if they hit a RBC in a suspension. If gaps are created within the suspension, the light beams can be transmitted through a blood film. This occurs due to the presence of RBC aggregation where the formation of rouleaux leaves fluid gaps between the aggregates causing for increased transmittance of the incident light as shown in **Figure 1-12** for a sample of non-aggregated and aggregated RBCs:

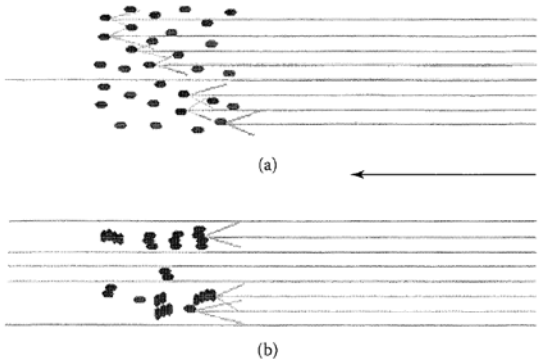


Figure 1-12: Interaction of light beams with (a) non-aggregated and (b) aggregated RBC suspensions. The direction of the arrow indicates the incident light beam direction (adapted from reference [21]).

These observations suggest that light transmittance or backscattering is a function of the size of the gaps and therefore can be used as an indicator of the degree of aggregation. Given a shearing condition, by monitoring the intensity of the transmitted or reflected light through a sample of blood one can monitor the time kinetics of the aggregation process. This has led to the development of a family of instruments known as photometric rheoscopes while the technique for measuring RBC aggregation using light is known as optical aggregometry.

The process of RBC aggregation is dynamic and typical time course which monitors the light reflectance (LR) as a function time is shown in **Figure 1-13**:

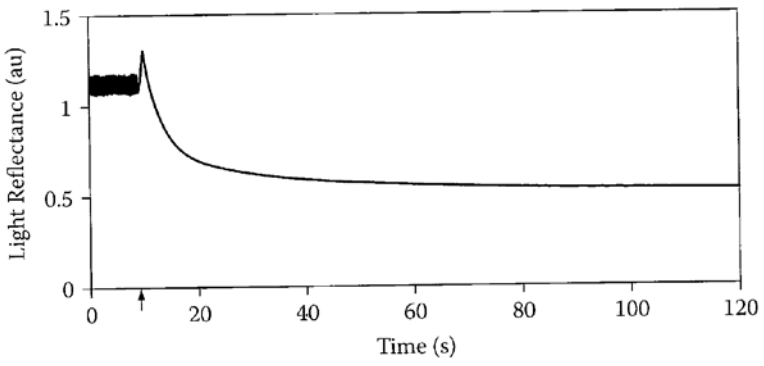


Figure 1-13: The time course of the light reflected from a 300 μm thick blood film placed between two glass cylinders. The arrow indicates the time when the rotating cylinder was stopped (adapted from reference [21]).

In this measurement, the blood was sheared between two concentric glass cylinders at a rate of 500 $s^{-1}$ for 10 s before the rotating cylinder came to an abrupt stop. While there are many techniques available to disaggregate the sample being investigated prior to the light intensity measurement, this procedure is typical of most optical aggregometry systems [56]. As can be observed in **Figure 1-13**, there is short-lasting (fast) increase in LR followed by a slower decrease. The increase in LR in the first phase represents the recovery of the shape of RBCs after the high rate shearing. The decreasing phase of the LR represents the RBC aggregation process. This second phase is also characterized by a fast change portion of LR during the first ~10 s of aggregation followed by the slower change for the remainder of the time course [57]. Such curves are known as syllectograms and can be analyzed mathematically in order to obtain a number of parameters related to the time course and magnitude of the aggregation process. In addition to measuring the extent and time course of aggregation, optical aggregometry has also been used to assess magnitude of the forces holding the aggregates together by measuring a parameter known as the disaggregation shear rate [56]. Furthermore, by changing the wavelength of the incident light beam, the degree of aggregation results have been shown to be affected by the oxygen dependent optical absorption of blood [58].

There have been significant advances in commercializing optical aggregometry instruments. Many leading laboratories have access to devices like the Myrenne Red Blood Cell Aggregometer (Myrenne GmbH, Roetgen, Germany), Laser-Assisted Optical Rotational Cell Analyzer (R&R Mechatronics, Hoorn, The Netherlands) and RheoScan-A (Rheomeditech, Seoul, South Korea). The parameters that these devices are capable of generating are either dimensionless indexes such as the aggregation index or capable of assessing the time kinetics of the aggregation while being dependent on the geometry of the measurement chamber. These parameters cannot be directly compared even though they are derived using the same mathematical approaches [59]. Furthermore, there have been reports comparing data from different laboratories using the same instruments by the same manufacturer which have yielded a wide distribution range thus limiting direct comparisons [60]. This is due to a lack of aggregation standards for calibrating these instruments since the aggregation parameters are not similar to blood chemistry parameters which have normal ranges worldwide. The experimental conditions in each laboratory (i.e. sample preparation or suspending medium) heavily influence the measurements performed using these instruments. In addition, there has currently been no direct correlation between the indexes of aggregation generated using such instruments and the *in-vivo* conditions of RBC aggregation [61].

### 1.3.4 Ultrasound imaging

Ultrasound (US) imaging is a non-invasive modality that became accepted for diagnostic imaging in the early 1970's when gray scale ultrasonography was first introduced [62]. Since then, the interaction of US waves with blood has received considerable interest. The propagation of US waves through inhomogeneous media such as biological tissue is characterized by the absorption of the energy carried by the US wave and its conversion into heat, by the reflection and refraction of the incident sound wave from tissue interfaces and by the scattering due to the components of tissue

[63]. The absorption of the sound wave is governed by the absorption coefficient of the medium dictated primarily from the composition of tissue. Reflection, refraction and scattering phenomena are dependent upon the size of the particles of the medium which scatter the incident US wave and the wavelength of that wave. When the size of the interfering particle is much larger than the wavelength, reflection/refraction phenomena govern the US propagation. When the opposite is true, scattering phenomena dominate. These interfering particles in the latter case are known as Rayleigh scatterers. In blood, the scattering of US waves is almost entirely due to the RBCs because they are much more numerous than the slightly larger white cells and significantly larger and more numerous than the platelets [3].

Rayleigh scattering theory has been the driving framework for understanding the physical mechanisms which generate the scattered signal from RBCs [64]. For diagnostic frequencies (2-30 MHz), the wavelength of the US beam is 770 μm and 51 μm, respectively. This does not allow for individual RBCs (8.2 μm diameter for human cells) to be resolved in an US image. Rayleigh scattering theory predicts that the scattering power of the RBCs increases with the fourth power of the US frequency and the square of the scatterer volume. This relationship changes when the RBCs aggregate and the size of the aggregate approaches the wavelength of the interrogating US wave. It was shown using porcine blood at low shear rates that the frequency dependence of the backscattering coefficient (BSC) was smaller than the forth power predicted by Rayleigh theory because of the presence of RBC aggregation [65]. The BSC is defined as the US power backscattered by a unit volume of scatterers per unit incident intensity, per unit solid angle [64]. Furthermore, the US BSC from suspensions of RBCs was shown to be affected by the concentration of fibrinogen or dextran present in the suspending medium which suggests that US is capable of correlating the BSC power measurements with degree of aggregation [66], [67].

The US signal received from moving scatterers has a different frequency compared to the transmitted ultrasonic signal. This change in frequency is known as the Doppler effect and the magnitude of the shift (Doppler frequency shift) is proportional to the axial velocity of the scatterers [62]. Such unique property has allowed for the detection and measurement of blood flow velocity. The effect of RBC aggregation on the magnitude of the Doppler signals has been extensively investigated. Using steady laminar flow inside a tube, the shear rate dependence of porcine RBC aggregation was investigated using the Doppler US technique for porcine RBCs [68]. It was found that the Doppler power was minimum close to the wall and maximum close to the center of the tune where the local shear rate was minimum. In addition, the backscattered Doppler power was increased by 12.4 dB when the flow rate was varied from 1500 to 125 ml/min. These results demonstrate the ability of US imaging to detect the presence of RBC aggregation in conditions where the local shear rate (i.e. as determined by the flow velocity) allows the formation of RBC aggregates.

In addition to measuring the BSC, Cloutier and colleagues developed the structure factor size estimator (SFSE) model based on the dependence of the BSC on US interrogation frequency [67], [69], [70]. This model relates two parameters to RBC aggregation: the packing factor (W) which increases with the clustering of the RBCs forming aggregates and the ensemble averaged aggregate isotropic diameter (D) which corresponds to an index of aggregate size in terms of the number of RBCs per aggregate. The dependence of these parameters on various shearing conditions can be seen from **Figure 1-14**:

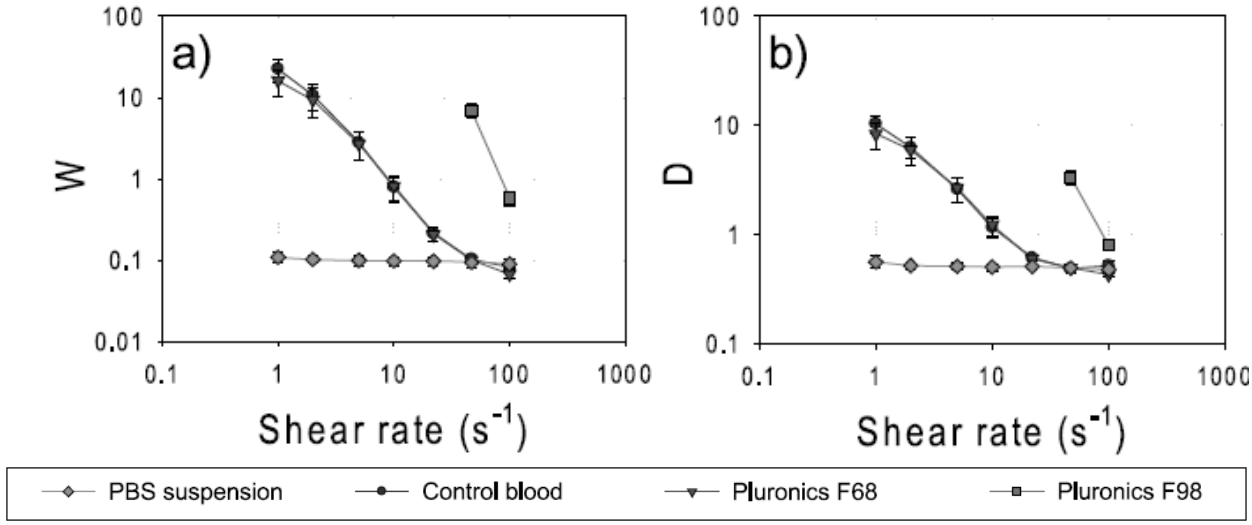


Figure 1-14: Dependence of (a) W parameter and (b) D parameter (calculated by SFSE) on the shear rate for porcine RBC suspensions (adapted from reference [69]).

As shown from both graphs in **Figure 1-14**, neither parameter was influenced by shear rate for RBCs suspended in PBS where no aggregation occurs. In the presence of aggregation (either normal or induced by Pluronic polaxamers), both parameters decreased with increasing shear rate. This suggest that as the shear rate increases, the clustering (W) and size (D) of the aggregates decreases since high shear rates disperse RBC aggregates. For the F98 group, both parameters were significantly higher than any other group. This is expected as this specific polaxamer has been shown to cause the formation of larger and stronger aggregates than most other polymers [69].

Although US imaging techniques seem promising for providing quantitative measurements of RBC aggregation, robust methods for *in-vivo* applications are yet to be developed. US imaging generally suffers from poor soft-tissue contrast due to similar acoustic impedances between most tissue types. Cardiovascular imaging relies on the introduction of ultrasound contrast agents to increase the signal-to-noise ratio from blood [71]. This is due to the fact that at clinical diagnostic US frequencies, RBCs cannot be resolved since the resolution of the imaging system depends on frequency. By increasing the interrogation frequency one can improve the resolution of the imaging system but the ability to penetrate deeper within the body is proportionally reduced. These common

disadvantages of US imaging might affect the ability to properly resolve RBC aggregation in physiologically relevant depths. Another important limitation faced by US imaging is the control of the shearing conditions during *in-vivo* studies thus making it extremely difficult to obtain parameters that could be compared with the control conditions during the same exam. Most BSC parameters developed were designed for *ex-vivo* cessation of flow using external manipulations [72]. Furthermore, the relationship between US BSC and hematocrit is a complex one as shown in the **Figure 1-15**:

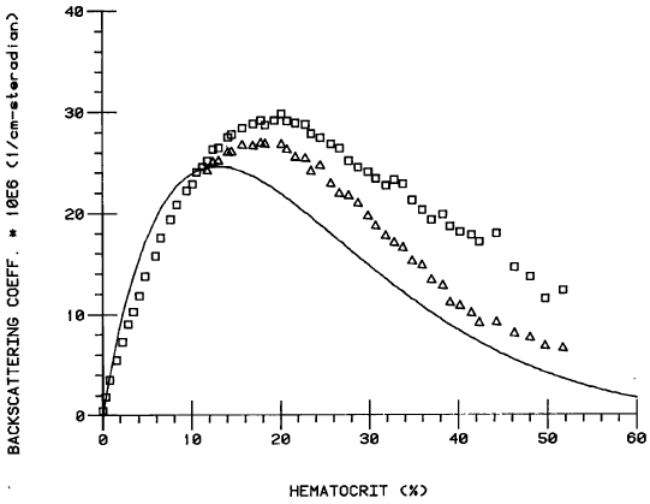


Figure 1-15: US BSC versus hematocrit for human RBCs under experimental stationary (squares) and stirred (triangles) conditions. The solid line represents the theoretical curve (adapted from reference [73]).

The BSC peaks at a certain hematocrit level depending on the US interrogation frequency and decreases thereafter. This phenomenon is well-known due to the fact that US waves scattered from RBCs may interfere constructively or destructively depending on the relationship between the spatial distribution of the RBCs and the US wavelength, in a manner somewhat similar to Bragg scattering [74]. In the presence of aggregation (which occurs during stationary blood as shown in **Figure 1-15**), the BSC vs. hematocrit relationship deviates even more from that of stirred blood (i.e. non-aggregated). This relationship makes it difficult for US imaging to assess RBC aggregation since the

process carries a very strong hematocrit dependence and it might not be possible to differentiate the presence of aggregation from other hematocrit-dependent disorders such as anemia [21].

### 1.4 Impact of RBC aggregation

RBC aggregation is a phenomenon with important physiological consequences. Aggregation is observed in the blood of most mammalian species at low shear rates and is primarily due to the effect of macromolecules such as fibrinogen [21]. The effect of aggregation on *in-vivo* hemodynamics is studied by examining flow resistance as a function of flow rate. Measurements of the venous vascular resistance as a function of blood flow in the venous microcirculation of the gastrocnemius muscle of a cat reveal that in the presence of RBC aggregation, there is a reduced dependence of flow resistance on flow rate [75]. This suggests that aggregation plays an important role in maintaining normal venous hemodynamics which are important determinants of capillary flow dynamics and tissue perfusion. In addition, the presence of RBC aggregation blunted the velocity profiles under slow flow conditions when the perfusion pressure is reduced by half compared to control conditions [76]. In another study where rat mesentery was infused with dextran-500 to induce aggregation, the blood flow (measured using intravital microscopy) decreased by 80% of the original flow while the viscosity increased [77]. This result provides hydrodynamic explanation for the higher flow resistance observed in the presence of RBC aggregation. A thorough analysis of the majority of experimental studies investigating the *in-vivo* effects of aggregation is presented in reference [21].

It should be noted that the "normal" range of aggregation is difficult to define due to the nature of the measured aggregation parameters as determined by the various approaches and instruments. This almost always requires the comparison of the results with the control measurements obtained using the same conditions. RBC aggregation has also been reportedly

influenced by certain physiological states and extreme conditions. There have been reports of gender differences in aggregation with healthy females exhibiting higher aggregation tendencies than males [78]. The subject's age has also been shown to alter RBC aggregation with older subjects exhibiting higher RBC aggregation levels as a result of increased concentrations of fibrinogen [79]. Moreover, enhancements of RBC aggregation have been reported during healthy pregnancies and labor. Along the same line, fetal blood also exhibited increased RBC aggregation [80], [81]. These changes were also attributed to increased fibrinogen concentration. Interestingly, physical exercise has been attributed to decrease RBC aggregation with reductions in RBC deformability being a potential cause [82].

Alterations of RBC aggregation due to pathological conditions have been extensively reported. A pathological state where RBC aggregation is increased is the acute phase reaction of infections [83]. This is an important reaction cause in response to infections, tissue injuries or immunological disorders. Increased plasma fibrinogen concentration due to acute phase reaction is related to observed increases in RBC aggregation. For this reason, ESR is a commonly used test conducted when inflammation is suspected due to infections or septic shock [84]. In addition, enhanced aggregation has been reported in patients with hypertension, atherosclerosis, myocardial ischemia and infarction, cerebral ischemia, stroke and diabetes etc [21]. Ongoing debate on whether aggregation is the "maker or marker" of these diseases persists [85]. It is postulated that RBC aggregation may simply be a reflection to the inflammation that characterizes atherosclerosis or it may play a role in the development of endothelial dysfunction that causes atherosclerosis. This highlights the importance for detecting and characterizing the phenomenon of RBC aggregation.

## 1.5 Photoacoustics and its potential

### 1.5.1 Photoacoustic effect and the generation of photoacoustic signals

The photoacoustic (PA) effect was first reported by Alexander Graham Bell in 1880 when he observed that chopped sunlight generated audio waves when incident upon a selenium cell [86]. For nearly a century, this effect was not exploited due to lack of appropriate sources until Kreuzer reported the detection of gas components using a laser-induced PA effect [87]. A more modern understanding of the process describes the PA effect as the generation of acoustic waves from the illumination by pulsed or modulated electromagnetic radiation in the form of optical, radio frequency or microwaves. In this thesis, the electromagnetic radiation source giving rise to the PA signals is in the optical regime unless otherwise noted.

Upon the optical illumination of an object, some of the energy is absorbed by the object and is converted into heat increasing the temperature of the object. The slight temperature rise (typically in the millikelvin range) causes thermal expansion to take place generating acoustic pressure waves in the medium [88]. It is important to note that the heating source (i.e. optical irradiation) must be time variant as a steady thermal expansion (i.e. time invariant heating) does not generate acoustic waves. In pulsed, laser-based heating, two important timescales exist [89]. The first one is the thermal relaxation time $\tau_{th}$ which is given by:

$$\tau_{th} = \frac{d_c^2}{4D_T} \tag{1-2}$$

where, $d_c$ is the characteristic dimension of the heated region (i.e. absorber size) and $D_T$ is the thermal diffusivity of the sample. The second timescale is the stress relaxation time $\tau_s$ which is given by:

$$\tau_s = \frac{d_c}{v_s} \tag{1-3}$$

where, $v_s$ is the speed of sound. In order to generate PA signal efficiently, the laser pulse width must be much shorter than $\tau_{th}$ (thermal confinement) leading to an excitation where the heat conduction is negligible during the laser pulse. In addition, the laser pulse width must also be shorter than $\tau_s$ (stress confinement) leading to negligible stress propagation during the laser pulse. Under these conditions, the PA pressure $(p)$ generated in an acoustically homogenous and non-viscous medium is given by the following equation:

$$\nabla^2 p - \frac{1}{v_s^2}\frac{\partial^2 p}{\partial t^2} = -\frac{\beta}{C_P}\frac{\partial H}{\partial t} \tag{1-4}$$

where, $\beta$ is the isobaric thermal expansion coefficient, $C_P$ is the heat capacity per unit mass and $H$ is the thermal energy deposited by the optical radiation per unit time and volume [90]. If the optical radiation with intensity $I_0$ propagates along the $x$ axis and varies sinusoidally with time, the heating function can be expressed as $H(x,t) = \mu I_0 \exp(-i\varpi t)$. Here, $\mu$ is the optical absorption coefficient of the illuminated medium and $\varpi$ is the modulation frequency of the optical beam. The steady state pressure field will then also vary sinusoidally for the heating function given above thus reducing **Eq. (1-4)** into a time independent form:

$$\nabla^2 p + k^2 p = \begin{cases} \dfrac{i\varpi\mu\beta I_0}{C_P} & \text{inside the aborber} \\ 0 & \text{outside the absorber} \end{cases} \tag{1-5}$$

where, $k$ is the wave number of the pressure wave. Using the appropriate boundary conditions, it possible to obtain analytical solutions of **Eq. (1-5)** for several simple geometries (layer, cylinder and sphere). It is common to work with frequency domain solutions of **Eq. (1-5)** for cases when the surrounding fluid (assumed to be optically transparent) and the optically absorbing object have different speed of sounds and densities [91]. For instance, the frequency domain solution for the PA

pressure from the uniform illumination of a single spherical absorber at a distance $r$ in the surrounding medium can be written as:

$$p_{\text{single}}(\hat{q}) = \frac{i\mu\beta I_0 v_s a^2}{C_P r} \times \frac{\left[\sin\hat{q} - \hat{q}\cos\hat{q}\right]\exp(ik_f(r-a))}{\hat{q}^2\left[(1-\hat{\rho})(\sin\hat{q}/\hat{q}) - \cos\hat{q} + i\hat{\rho}\hat{v}\sin\hat{q}\right]} \tag{1-6}$$

where, $\hat{q}$ is the dimensionless frequency defined as $\hat{q} = \varpi a / v_s$, $a$ is the radius of the absorbing sphere, $k_f$ is the wave number of the fluid medium and $\hat{\rho}$ and $\hat{v}$ are the dimensionless ratios of the sphere density and speed of sound to the surrounding fluid medium density and speed of sound. The subscripts $f$ and $s$ denote the properties of the fluid medium and the spherical absorber, respectively. The PA pressure in the frequency domain (i.e. spectral power) for two fluid spheres of varying sizes and physical properties is shown in **Figure 1-16**:

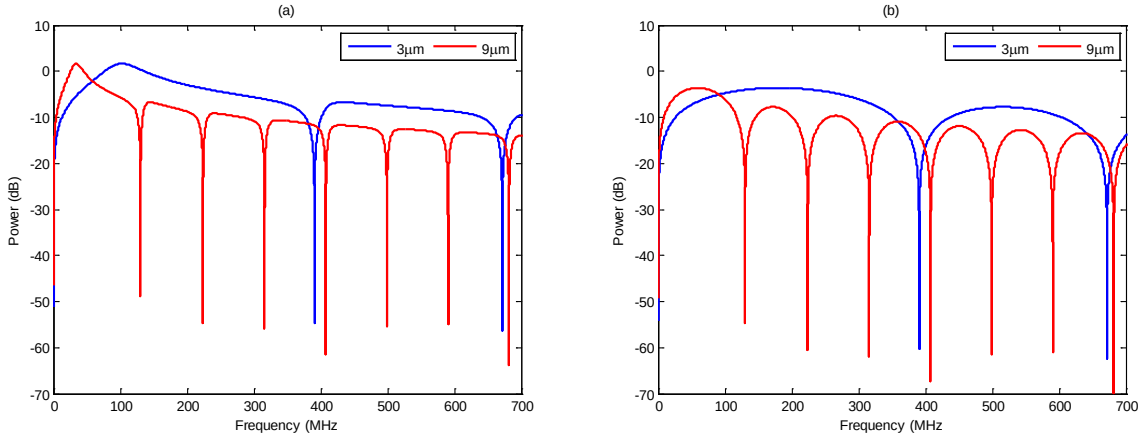


Figure 1-16: PA spectral power for two fluid spheres (radius 3 μm and 9 μm) with density and speed of sound ratios of (a) $\hat{\rho} = \hat{v} = 0.5$ and (b) $\hat{\rho} = \hat{v} = 1.0$.

The size of the optical absorber dictates the spectral features of the PA signal, as shown by **Figure 1-16**. The larger the size of the sphere, the lower is the frequency at which the first peak appears. The density and speed of sound ratios control both the shape of the power spectra as well as the spectral amplitude. The advantage of working in the frequency domain of the PA pressure is that direct information can be obtained about the size of the optical absorber as well as the physical

properties of that absorber and the surrounding fluid [90]. In addition, the time domain PA pressure can be obtained by taking in inverse Fourier Transform of **Eq. (1-6)**.

### 1.5.2 Propagation of light and sound waves in tissue

Most biological tissues are referred to as turbid media due to their strong scattering of optical irradiation. The scattering coefficient $(\mu_s)$ in tissue is typically in the order of ~100 $cm^{-1}$ and the reduced scattering coefficient $(\mu_s')$ is ~10 $cm^{-1}$ [92]. Another important concept is that of optical absorption which is quantified by the optical absorption coefficient $\mu_a$. Compared to scattering of light, the optical absorption of light photons is weak in the 400-1350 nm spectral region. Specifically, the mean free path of a photon between scattering events is in the order of 0.1 mm while the mean path length before photons are absorbed can extend to 10-100 mm [93]. Although the propagation of light in a media is usually modelled by the radiative transfer equation, the fluence rate in the ballistic and diffusive regime can be described by:

$$\begin{aligned} &\text{Ballistic regime: } \Phi(z) = \Phi_0 \exp(-\mu_a z) \\ &\text{Diffusive regime: } \Phi(z) \approx \Phi_0 \exp(-\mu_{eff} z) \end{aligned} \tag{1-7}$$

where, $\Phi_0$ is the illumination fluence, $z$ is the depth and effective attenuation coefficient is defined as $\mu_{eff} = \sqrt{3\mu_a(\mu_a + \mu_s')}$. Since tissue is a highly scattering media, the attenuation of light depends on both the scattering and absorption coefficients as shown by the dependence of the fluence rate in the diffusive regime. In biological tissue typical absorbers of optical irradiation are water, melanin and blood. The Hb molecule residing inside RBCs is the primary optical absorber of blood. Its optical absorption carries a strong dependence on the oxygenation state of the molecule. In biological tissue, blood is a mixture of both OHb and DHb and $\mu_a$ depends on both the

concentration of each state of the Hb molecule and their respective molar extinction coefficients $\varepsilon$. For a given optical wavelength $\lambda$, $\mu_a$ can be calculated by:

$$\mu_a(\lambda) = 2.303 \times \left[\varepsilon_{OHb}(\lambda)[OHb] + \varepsilon_{DHb}(\lambda)[DHb]\right] \quad (1\text{-}8)$$

In the visible and near infrared range of the electromagnetic spectrum, $\mu_s$ is significantly smoother while $\mu_a$ varies significantly with wavelength. **Figure 1-17** shows the variation of $\varepsilon$ for OHb and DHb as a function of the optical wavelength:

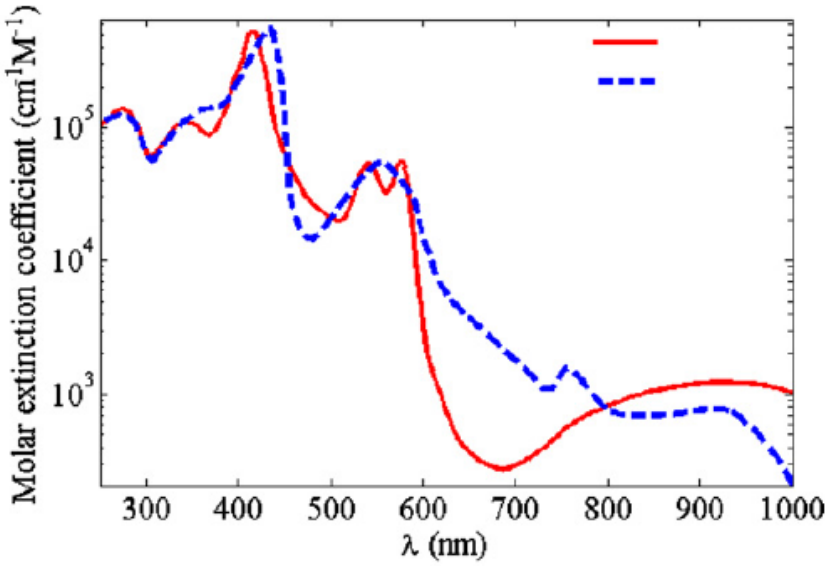


Figure 1-17: Molar extinction coefficient of OHb (solid) and DHb (dashed) (adapted from reference [89]).

As can be seen from **Figure 1-17**, the significant dependence of $\mu_a$ with $\lambda$ plays an important role in being able to detect PA signals from various depths in tissue. The absorption of water in tissue is lowest for the range ~500-1100 nm thus permitting PA techniques in targeting regions in tissue deeper than the ballistic regime (~1 mm in turbid tissue) [88].

The resulting acoustic waves produced from the thermo-elastic expansion due to optical absorption propagate through tissue and can be detected by transducers commonly used for US imaging operating in passive mode (i.e. do not transmit acoustic waves). The detection of these PA pressures becomes dependent on the acoustical properties of tissue. Unlike light where scattering

dominates during the propagation in tissue, the scattering of acoustic waves is 2-3 orders smaller [94]. The pressure waves propagate through tissue with magnitudes in the millibar range thus eliminating the occurrence of non-linear effects that are typically associated with conventional US imaging. In soft tissues, the scattering component of attenuation comprises ~10-15% of the total attenuation and it can be usually ignored when calculating total attenuation [88]. However, the attenuation of the sound waves due to absorption cannot be ignored especially when detecting high frequency waves or imaging deeply absorbing media such as the skull [95]. For diagnostic ultrasound frequencies (< 30 MHz), the attenuation coefficient of soft tissue can be estimated to be 0.3 dB/cm/MHz while for high frequency US imaging it can be as high as 3 dB/cm/MHz, depending on the tissue type [71]. In addition, the attenuation of US increases with frequency and the penetration depth decreases with frequency. The spatial resolution of PA imaging depends on the US bandwidth [96]. For instance, a ~1 mm spatial resolution can be achieved for PA signals detected with a 1 MHz bandwidth since the speed of sound in soft tissues is approximately 1.5 mm/μs. The resolution can be improved to ~0.1 mm when the bandwidth increases to 10 MHz at the expense of penetration depth. This results in temporal changes of the PA pressure waveform in addition to decreased amplitude due to attenuation. In contrast to US imaging, PA waves are only exposed to the attenuation of the surrounding tissue only once due to their one-way propagation.

### 1.5.3 Applications of PA in medicine

PA imaging breaks the optical diffusion limit that restricts the penetration depth of light photons by detecting the light-induced acoustic waves generated by the thermo-elastic expansion of tissue. By choosing the appropriate transducer bandwidth in the detection of the sound waves, PA enables the high resolution imaging of biological structures with sizes ranging from organelles to organs using the same contrast [97]. Using multiple wavelengths allows PA imaging to generate rich optical contrast according to the chemical composition of the tissue being irradiated. This is an advantage

of PA over other optical modalities (i.e. fluorescence imaging) since all tissue components absorb light at some optical wavelength while far fewer molecules are fluorescent [98]. Since the PA signal amplitude is directly proportional to the optical absorption in tissue, non-absorbing structures do not contribute to the background of PA images thereby enhancing the contrast. Despite the fact that both US and PA imaging are based on the detection of acoustic waves, US imaging measures only the mechanical contrast of tissues while PA imaging probes both the optical and thermo-elastic contrast [94].

Although PA was proposed as an imaging modality over 30 years ago, it did not fully develop until the past decade [99]. PA imaging has shown a significant amount of progress in providing simultaneous structural, functional and molecular information in preclinical studies. It has been shown that PA imaging can visualize tumors within tissue with the contrast of optical imaging and the resolution of ultrasound [100]. In addition to providing information on the vasculature of tumors, PA imaging has also been able to monitor angiogenesis [101], [102]. By using multiple wavelengths to probe the oxygen-dependent absorption of blood, PA can also obtain information on Hb concentration with high resolution and contrast without the use of exogenous contrast agents [103–105]. This is a significant advantage compared to other imaging modalities such as PET. In addition to oxygen dependent studies, PA imaging has also been explored as a tool for molecular imaging applications [106]. Gold nanoparticles with high optical absorption can be targeted to specific cancer biomarkers and thus can be used for the non-invasive detection and monitoring of cancer at the molecular level. Such targeting of nanoparticles helps in early detection of cancer due to the large difference in optical absorption between the particles and tissues. This enhances the contrast of PA images and in conjunction with US images can provide dual information about the structure and physiology of the tumors being targeted. Moreover, the potential of PA in detecting normal and abnormal vasculature has also been explored [107]. PA has also been used for

monitoring thermal therapy and estimating the thermo-mechanical properties of tissue [108], [109]. Recently, a new type of contrast agent was developed for simultaneous US and PA imaging and therapy (optical droplet vaporization) [110].

As it is still a fairly new imaging modality, PA is expected to find a wide range of applications in biomedicine. The preclinical applications include imaging circulation, drug response and brain function and clinical applications include melanoma cell detection, intravascular catheter imaging, breast cancer detection, guided biopsy for sentinel lymph node imaging and blood oxygenation imaging etc [97]. It is expected that the translation of PA imaging from small animals to humans will transform diagnosis and treatment of metabolic diseases while imaging of cells and metabolism with PA will provide a unique tool for understanding pathways down to the single cell level.

### 1.5.4 US and PA radio-frequency spectroscopy

PA images can be reconstructed by displaying the amplitude of the envelope-detected radio-frequency (RF) signals that are received from a passive US transducer as image brightness pixels. This approach is nearly identical to conventional US B-mode imaging with the exception that the RF signals represent the backscattered echoes formed due to the interactions of the incident US beam with structures within the region of interest (ROI) [63]. The major difference between US and PA imaging is the origin of the RF signals in PA, namely due to the interaction of incident optical irradiation with tissue chromophores (endogenous and exogenous). B-mode US imaging is capable of distinguishing larger-than-wavelength structures because tissue interfaces such as organ boundaries produce well-defined backscattered RF signals thus facilitating the envelope detection process and image formation. This has allowed US imaging to be extended outside of obstetrics into the diagnosis and therapy monitoring of cystic and fibrocystic breast masses as well as other types of carcinoma [111].

US images are degraded by phenomena that are usually not present in other imaging modalities [112]. The degradation of images usually occurs due to the coherent nature of ultrasound and complex spatial distribution of mechanical properties resulting from the internal microstructure of most biological tissues. RF backscattered signals from such structures contain the interference pattern arising from the proximity of the scatterers. These scatterers cannot be resolved in the B-mode images due to overlap in time and this leads to the appearance of speckle [71]. In addition, the speckle in the B-mode images is also affected by the instrument itself as well as the setting used during the exam. The resulting speckle pattern consists of bright and dark spots in the US images that are usually interpreted only on the basis of boundary geometry and texture without providing apparent information about the underlying tissue structure [113]. To overcome these limitations, many investigators have attempted to provide a framework for using US imaging as for quantitative tissue evaluations. These methods described here are commonly referred to as quantitative ultrasound (QUS) techniques are usually based on frequency-domain (spectral) analysis of the backscattered RF signals as opposed to the RF signal envelope [114–116]. In this approach, the power spectra of the RF signals from the ROI are first computed. The system dependence is taken into account by computing the power spectrum of the transducer pulse-echo response (typically obtained from a plane reflector) and subtracting it from the power spectrum of the ROI RF signals. This removes the artifacts that are associated with the system transfer function of the electronic transmitter/receiver and the operator dependent settings. The resulting spectrum (referred to as the normalized power spectrum) is often quasi-linear over the usable transducer bandwidth (frequency range that has been found to produce adequate signal-to-noise levels). The normalization procedure is shown in **Figure 1-18**:

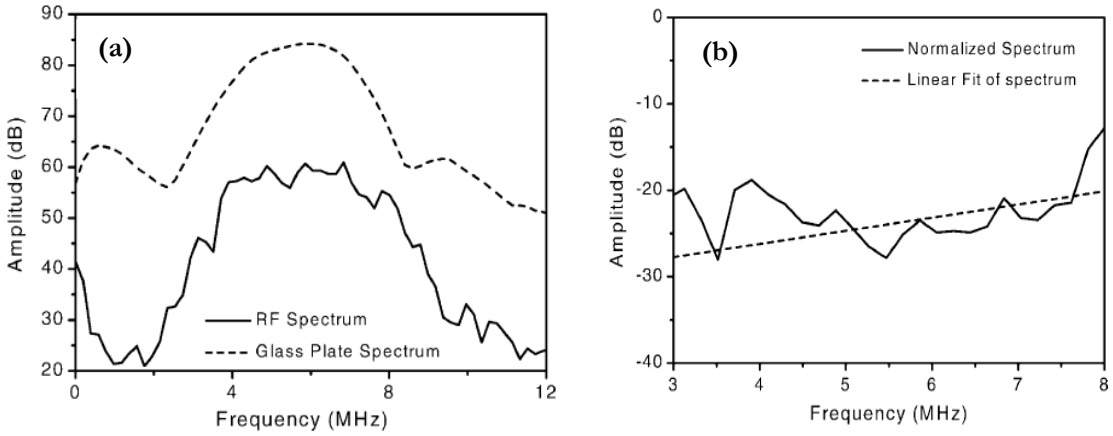


Figure 1-18: Power spectra for (a) the RF signal obtained from tissue and the RF signal obtained from reflection off a glass plate and (b) normalized power spectrum obtained by subtracting the tissue spectrum from the glass plate spectrum and the linear fit over the transducer bandwidth (adapted from reference [112]).

Linear regression analysis is often performed on the normalized spectrum and several parameters can be extracted. These parameters have been correlated with structural tissue properties and can be used for obtaining quantitative information about the size, shape and concentration of the acoustic scatterers [115]. The spectral slope (SS) of the line of best fit with respect to frequency is an indicator of the effective scatterer shape and size and a decrease in SS corresponds to an increase in the effective scatterer size. Another useful parameter is the midband fit (MBF) which is defined as the value of the regression line at the center frequency of the spectral band. This parameter is numerically equal to the average value of the spectrum over the measurement bandwidth and is a measure of US backscatter that depends on the scatterer size, shape, acoustic impedance and concentration. The spectral analysis techniques relying on the abovementioned parameters have been broadly classified as ultrasonic tissue characterization techniques (UTC) and have proven effective in identifying changes due to the state of prostate, breast and have even been applied for real-time tissue typing [117]. In addition, QUS techniques have been applied to monitoring the morphological changes that occur during chemotherapy treatments of various tumor models [118].

It is well established that in PA, the size of the optical absorber dictates the frequency content of the power spectrum of the RF signals [90], [119]. We postulate that based on this, the

spectral analysis of PA RF signals (photoacoustic radio-frequency spectroscopy or PA-RFS) will provide information about the structure of the optical absorber. It is reasonable to expect that information about the size and concentration of the optical absorbers will be manifested in the PA RF power spectra and can be extracted from the SS and MBF parameters of the normalized power spectra. It would be worthy to investigate the potential of PA-RFS for monitoring changes in the size and concentration of PA spherical sources.

## 1.6 Thesis motivation, hypothesis and specific aims

The study of the aggregation of RBCs dates back to the works of ancient Greek physicians such as Hippocrates who recognized the mixture of four fluids that were believed to be the constituents of blood vessels [21]. By allowing whole blood (without an anticoagulant) to settle inside a cylindrical container and by measuring the amount of each layer, a diagnostic tool was developed. Although not quite recognized at the time, RBC aggregation affects the rate of this separation. It wasn't until Robin Fahraheus showed that the speed with which RBC sediment differs in various physiological and pathological conditions that the importance of RBC aggregation was recognized [120]. Ever since, many studies have attempted to detect, quantify and characterize the presence of RBC aggregates in normal and diseased subjects. Blood with increased levels of RBC aggregates has been associated with conditions ranging from sepsis and severe trauma to normal, uncomplicated pregnancies [121]. Although it is still not yet conclusively established what role the RBC aggregates play in the disorders where they are reportedly increased, significant efforts has been invested in attempting to quantify the presence of RBC aggregation and make clinical decisions based upon the measured levels of aggregation. However, most of the techniques that have been used to detect and quantify the presence of RBC aggregation require the invasive withdrawal of blood outside the body and are heavily dependent on the measurement conditions. Furthermore, there is no direct correlation between the parameters measured with these techniques and the presence of RBC

aggregation *in-vivo*. This thesis was motivated by the shortcomings of current aggregation detection methods and the use of PA is proposed as a potential method for detecting RBC aggregation. PA is a non-invasive technique that generates acoustic signals based on the selective absorption of optical irradiation. Since RBCs are the dominant optical absorbers in circulation, it is expected that the PA signals recorded will depend upon the RBC configuration. PA is capable of providing not only structural information about the absorbers of blood but also functional information about their oxygenation state which controls the optical absorption of blood.

The hypothesis guiding this investigation is that PA techniques can be used to detect and monitor the presence of RBC aggregation. Specific objectives set forward for this work include:

1. To improve an already developed theoretical model of the PA of RBC aggregation. This will be accomplished by incorporating the effect of a finite transducer bandwidth for more realistic comparisons with experiments. The effect of the transducer bandwidth will be investigated in the power spectra from non-aggregated and aggregated RBCs. Also, the effect of the oxygenation level of the RBCs will be simulated by in order to examine the simultaneous effect of RBC aggregation and oxygenation on the simulated PA signals and power spectra. In addition, this model will also be extended from human to porcine RBCs in for various hematocrit and aggregation levels.
2. To determine experimentally how the presence of aggregation (in human and porcine RBCs) affects the measured PA signals and their respective power spectra. Specifically, the effect of the size of aggregates on the power spectra will be investigated as a means for detecting the presence of RBC aggregates.
3. To develop PA-RFS techniques and generate spectral parameters that could potentially be related to the size and concentration of aggregates. This will be performed under varying

hematocrit and aggregation conditions. In addition, multiple wavelength laser illumination will be used for monitoring the oxygenation level of the samples.

## 1.7 Thesis outline

This thesis is organized in four chapters. An introduction of the phenomenon of RBC aggregation, current measurement methods and its clinical significance are introduced in Chapter 1. An overview of PA, PA-RFS and the potential for detecting RBC aggregation is also presented in the same chapter. In Chapter 2 a theoretical model is developed to simulate PA signals from non-aggregated and aggregated samples and *in-vitro* work using human and porcine RBCs is presented to investigate the potential of PA techniques for detecting and monitoring RBC aggregation. This chapter forms the basis of a paper to be submitted to Biomedical Optics Express and some of the results have been published in Proceedings of the SPIE (vol. 8222 and 8223) and Journal of Biomedical Optics (vol. 17(5)). Chapter 3 applies PA-RFS to the theoretical model and experimental results for porcine RBCs. Spectral parameters related to the size and concentration of RBC aggregates are extracted for varying aggregation and hematocrit conditions. The oxygen saturation of aggregating RBCs is also computed using multiple illumination wavelengths. This chapter forms the basis of a paper to be submitted to Journal of Biomedical Optics. The thesis summary and future directions are presented in Chapter 4.

# Chapter 2 PA OF RBC AGGREGATION

## 2.1 Introduction

In this study, the feasibility of detecting RBC aggregation with PA imaging is investigated theoretically and experimentally using human and porcine RBCs. The theoretical PA spectra will be simulated for various hematocrit and aggregation conditions. In addition, the effect of a finite transducer bandwidth will also be taken into account. Experimental conditions will also emulate various hematocrit and aggregation levels. The objective of this study is to demonstrate the potential of spectral analysis of PA RF signals for differentiating the PA signals produced from non-aggregated (NAG) and aggregated (AG) RBCs.

### 2.1.1 Theoretical model

The theoretical model used in this study was originally reported in two recent publications by our group [122], [123]. In order to compute the PA pressure field from NAG and AG RBCs (approximated as spheres), the analytical solution for the time-independent wave equation for spheres was solved in the frequency domain [90]. The solution to this equation assumes uniform optical irradiation with intensity $I_0$ which propagates along the $x$ axis and varies sinusoidally with time. The frequency-domain pressure for the uniform illumination of a single spherical absorber at a distance $r$ in the surrounding medium is:

$$p_{\text{single}}(\hat{q}) = \frac{i\mu\beta I_0 v_s a^2 \left[\sin\hat{q} - \hat{q}\cos\hat{q}\right]\exp(ik_f(r-a))}{C_P r\hat{q}^2\left[(1-\hat{\rho})(\sin\hat{q}/\hat{q}) - \cos\hat{q} + i\hat{\rho}\hat{v}\sin\hat{q}\right]} \tag{2-1}$$

where, $\hat{q} = \varpi a / v_s$ is the dimensionless frequency and $a$ is the radius of the absorbing sphere. The dimensionless quantities $\hat{v} = v_s / v_f$ and $\hat{\rho} = \rho_s / \rho_f$ represent the ratios of the speed of sound $(v)$ and density $(\rho)$ for the spherical absorber $(s)$ and surrounding fluid medium $(f)$, respectively.

Moreover, $k_f$ is the wave number in the fluid medium for a pressure wave with frequency $\varpi$, $\beta$ is the isobaric thermal expansion coefficient, $C_P$ is the heat capacity per unit mass, $v_s$ is the speed of sound in the illuminated region and $\mu$ is the optical absorption coefficient of the illuminated absorbers. In order to compute the PA pressure field from multiple absorbers, the superposition of spherical waves generated by the RBCs was calculated. Such approach has been implemented for light and ultrasound scattering problems in random media. In particular, Yu and colleagues use a similar approach to investigate the dependence of US BSC on RBC aggregation [67], [69]. Here it is assumed that all the absorbers (RBCs) within the ROI are identically illuminated irrespective of their spatial positions with multiple scattering being negligible. The non band-limited (NBL) pressure field from a collection of *N* absorbers can be written as:

$$p_{collection}^{NBL}(\hat{q}) = \frac{i\mu\beta I_0 v_s a^2 \left[\sin\hat{q} - \hat{q}\cos\hat{q}\right]}{C_P r\hat{q}^2\left[(1-\hat{\rho})(\sin\hat{q}/\hat{q}) - \cos\hat{q} + i\hat{\rho}\hat{v}\sin\hat{q}\right]} \times \sum_{n=1}^{N} \frac{\exp(ik_f(\left|\vec{r}-\vec{r}_n\right| - a)}{\left|\vec{r}-\vec{r}_n\right|} \qquad (2\text{-}2)$$

Here, $\vec{r}_n$ is the position vector of the n$^{th}$ absorber. If the observation distance $\vec{r}$ is large compared to the size of the ROI, the term $k_f\left|\vec{r}-\vec{r}_n\right|$ can be approximated as $k_f r - \vec{k}_f \cdot \vec{r}_n$ and the term $\left|\vec{r}-\vec{r}_n\right|$ can be approximated as $r$. The final expression is given by:

$$p_{collection}^{NBL}(\hat{q}) = \frac{i\mu\beta I_0 v_s a^2 \left[\sin\hat{q} - \hat{q}\cos\hat{q}\right]\exp(ik_f(r-a))}{C_P r\hat{q}^2\left[(1-\hat{\rho})(\sin\hat{q}/\hat{q}) - \cos\hat{q} + i\hat{\rho}\hat{v}\sin\hat{q}\right]} \times \sum_{n=1}^{N} \exp(-i\vec{k}_f \cdot \vec{r}_n) \qquad (2\text{-}3)$$

**Eq. (2-3)** does not take into account the finite nature of ultrasonic transducers used for PA experiments. In this model the finite bandwidth of the transducer was modeled as a Gaussian function which resembles the frequency response of typical ultrasound transducers [71]. The band-limited (BL) pressure then becomes:

$$p_{collection}^{BL}(\hat{q}) = p_{collection}^{NBL}(\hat{q}) \times \exp\left[-(\varpi - \varpi_0)^2 / 2\sigma^2\right] \qquad (2\text{-}4)$$

where, $\varpi_0$ is the center frequency of a transducer with the width of the Gaussian function $\sigma$ related to the -6 dB receiving bandwidth of the transducer (chosen to be 60%) by

$2\sigma\sqrt{2\log(2)} = 0.6\varpi_0$. The time-dependent PA pressure can be obtained by the Fourier transform of **Eq. (2-3)** for the NBL case and **Eq. (2-4)** for the BL case.

## 2.2 Methods

### 2.2.1 Simulation methods

The detailed description of the simulation methods used for generating PA signals from NAG and AG RBCs were presented in two recent publications by our group [122], [123]. The framework of these simulations will be discussed here in brief. For this study, 2D simulations were performed to determine the dependence of PA signals and power spectra on NAG and AG human and porcine RBCs, h-RBCs and p-RBCs, respectively.

NAG RBC samples were generated using a Monte Carlo method known as the random sequential adsorption technique. This allowed the coordinates of the cells to be randomly chosen within the ROI with the restriction that the cells must be separated by a distance equal to or more than their diameters and was repeated until the coordinates of all RBCs at a particular hematocrit (defined in this simulation as the ratio of the area occupied by the cells to the total area of the ROI) were set. Once the positioning of the RBCs within the ROI was completed, the Fourier Transform of **Eq. (2-3)** was evaluated to obtain the PA RF line for that particular configuration. Aggregation of RBCs was simulated by employing a hexagonal close packing scheme. RBC clusters (representing an aggregate) were formed by positioning individual RBCs in a hexagonal packing arrangement relative to one another. The aggregate was then randomly and repeatedly placed within the ROI and the coordinates of each RBC with respect to the center of the cluster were stored in order to evaluate the PA signal from **Eq. (2-3)**. For each cluster, the radius of gyration (Rg) was computed to quantify the mean cluster size. This was determined by using the square of the distances of the cells from the center of the cluster.

The physical constants and simulation parameters associated with NAG and AG conditions for h-RBCs and p-RBCs used in this study are summarized in **Table 2-1**:

| Physical Constants | | | Simulation Parameters | | | | |
|---|---|---|---|---|---|---|---|
| | h-RBC | p-RBC | | h-RBC | | p-RBC | |
| | | | | NAG | AG | NAG | AG |
| $a\ (\mu m)$ | 2.75 | 2.53 | $H\ (\%)$ | 2-50 | 40 | 5-50 | 40 |
| $\rho_f\ (kg/m^3)$ | 1005 | 1005 | $N\ (\#)$ | 34-842 | 674 | 99-994 | 795 |
| $\rho_s\ (kg/m^3)$ | 1092 | 1078 | $Cl\ (\#)$ | - | 54.8-11.8 | - | 50.2-12.1 |
| $v_f\ (m/s)$ | 1498 | 1498 | $N_{Cl}\ (\#)$ | - | 11.8-57.1 | - | 15.2-65.3 |
| $v_s\ (m/s)$ | 1639 | 1628 | $Rg(\mu m)$ | 2.13 | 7.6-15.4 | 1.96 | 7.7-15.4 |

Table 2-1: Physical constants and simulation parameters.

The physical constants were used to evaluate **Eq. (2-3)** and **Eq. (2-4)** for 200 μm x 200 μm ROI. In the simulation parameters column, $H$ stands for the hematocrit, $N$ is the number of total RBCs at the given hematocrit, $Cl$ is the number of clusters, $N_{Cl}$ is the number of RBCs per cluster.

2.2.2 Experimental methods

Proof of concept experiments were conducted using commercial h-RBCs extracted from a single donor (Innovative Research Inc., Novi, MI). Gentle centrifugation (1800 rpm, 6 minutes) was applied to remove any remaining plasma. Upon isolation, the RBCs were washed twice with phosphate buffered saline (PBS) and suspended in PBS at various hematocrit levels. The RBCs were aggregated using Dextran-70, a fibrinogen mimicking macromolecule (70,000 kDa molecular weight, Sigma-Aldrich Co., St. Louis, MO). This was achieved by suspending the RBCs in solutions of varying Dextran-PBS concentrations [Dex]. [Dex] of 1, 3 and 8% (wt/vol) were used to suspend the RBCs in order to induce varying aggregation levels at 40% hematocrit. The presence of aggregation was assessed by measuring the viscosity of each [Dex] using a low-shear viscometer (Contraves LS30, Zurich, Switzerland). The measurements were performed using h-RBCs and are shown in **Figure 2-1**. The viscosity measured at the lowest shear rate was compared to the PA SA measured for h-RBCs and the correlation coefficient along with the $p$ value was computed.

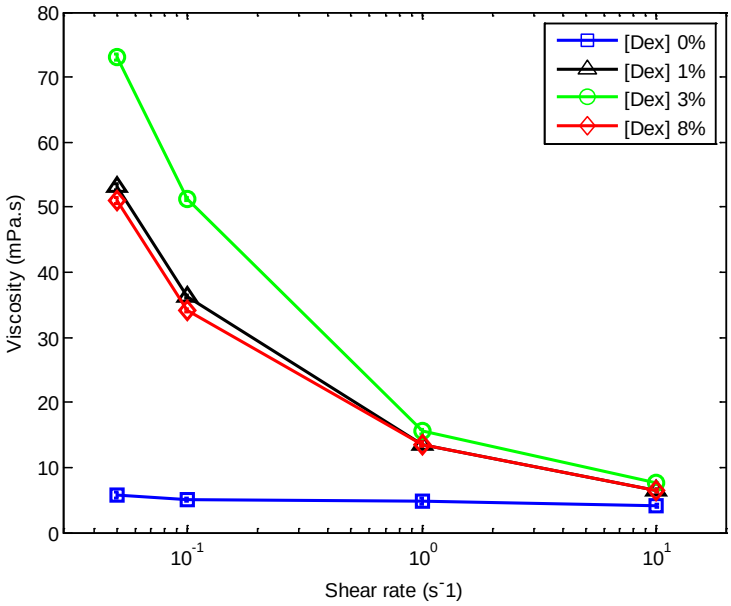


Figure 2-1: Effect of [Dex] on the viscosity of the h-RBC samples. The error bars (too small to be seen) represent the standard deviation of the viscosity measurements taken over 1 minute at a constant shear rate.

The validity of the technique was assessed using porcine blood extracted from the femoral vein of Yorkshire pigs (Comparative Research, Toronto, ON). The blood was collected into $K_2$-EDTA vacutaners (Becton, Dickinson and Company, Franklin Lakes, NJ). RBCs were separated from the plasma and white cells by centrifugation (2500 rpm, 6 minutes) and careful aspiration. The cells were then washed twice with PBS before being suspended in the same medium at 10, 20 and 40% hematocrit. For each hematocrit level, the NAG RBCs were suspended at 1, 3 and 8% [Dex] solution in order to induce aggregation. All experiments were completed within 4 hours of blood collection at room temperature.

PA measurements were performed using the Imagio small animal PA imaging device (Seno Medical Instruments Inc., San Antonio, TX) shown in **Figure 2-2**.

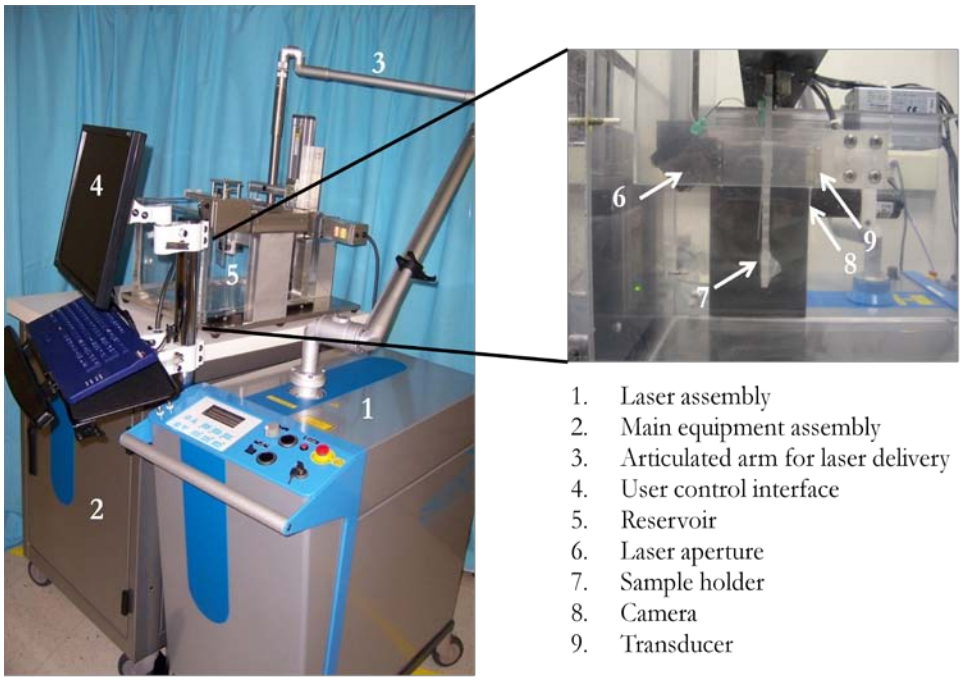


Figure 2-2: Imagio PA imaging system components.

This device consisted of a Q-switched Nd:YAG laser delivered through an articulated arm and a transducer mounted 60 mm coaxially to the laser for raster scanning the ROI. The pulsed laser (1064 nm) had a 9 mm beam diameter, 6 ns pulse width, 10 Hz pulse repetition rate and 25 $mW/cm^2$/pulse energy fluence. The transducer used to record the PA signals was a 4-channel annular array with center frequency of 5 MHz and a 60% -6dB bandwidth. The RBC samples were loaded into cylindrical tubes. For the h-RBCs, a 14 mm plastic Beral transfer pipette was used as a sample holder while a 0.5 mm inner diameter tygon tube (Norton Performance Plastic, Akron, OH) served as the sample holder for the p-RBC experiments. Both sample holders were placed at the focus of the ultrasonic transducer. A vertical raster scan was performed for each sample while the laser emitted 4 pulses at each location which were then averaged to generate 1 RF line. A total of 20 RF signals were recorded for each solution exposed corresponding to a total of 80 laser pulses that illuminated each RBC sample.

For each PA signal recorded, the PA SA was calculated by integrating the envelope of each signal. The average amplitude of 250 simulated and 20 measured PA signals was computed along with the standard deviation for each sample. The Fast Fourier Transform algorithm was used to compute the power spectrum. In order to minimize spectral leakage, a Hamming window was used. For each spectrum, the frequency at which the maximum peak of the RF power spectrum occurred was found. The mean spectral power in a -6 dB region around that peak was also computed. The average of the power spectra was then computed for both simulated and experimentally measured signals. The normality of the data was confirmed using a Shapiro-Wilk test with $W > 0.05$ used as the criterion for normality. An unpaired t-test was used to compare the PA SA and mean spectral power obtained from NAG and AG RBCs. A *p*-value of 0.05 or less was used to establish statistically significant differences.

## 2.3 Results

### 2.3.1 Simulation results

**Figure 2-3** demonstrates a representative 2D spatial organization of (a) NAG and (b) AG RBCs.

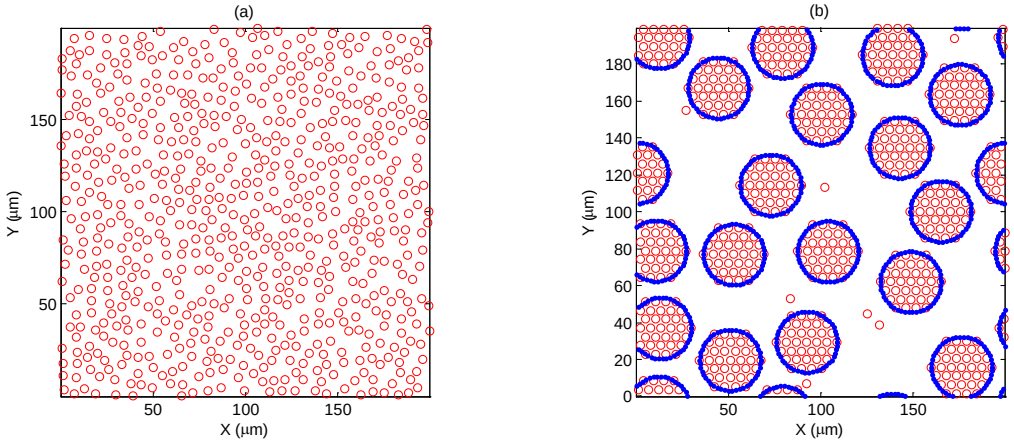


Figure 2-3: Representative (a) NAG and (b) AG RBC configurations simulated in this study. For both cases the hematocrit is 40% and for the AG case Rg is 12.24 μm.

The average of 250 simulated spectra for h-RBCs and p-RBCs are shown in **Figure 2-4**. For the NBL, NAG RBCs, the spectral power increases over all frequencies with increasing hematocrit

as shown in **Figure 2-4a** for h-RBCs and **Figure 2-4d** for p-RBCs. The peak of the RF power spectrum for h-RBCs occurred at ~230 MHz for all hematocrit levels (10, 20 and 40%). For the smaller p-RBCs, this peak was ~35 MHz higher. The mean spectral power at the peak was ~0.4 dB higher for p-RBCs compared to h-RBCs at all hematocrit levels.

**Figure 2-4b** and **Figure 2-4e** show the average NBL spectra for AG h-RBCs and p-RBCs, respectively. The AG samples had a 40% hematocrit level. For both cell types, as the size of the aggregates increased (characterized by increasing Rg), the peak frequency of the power spectra shifted towards the low frequency regime (< 30 MHz). At 15 MHz, the power spectrum of the 9.97 μm h-RBC aggregate increased by 9 dB compared to the NAG case for the same hematocrit level (40%). A similar increase was observed for p-RBCs.

The BL, AG spectra obtained by filtering the NBL AG spectra of **Figure 2-4b** and **Figure 2-4e** with a Gaussian function representing the frequency response of a 5 MHz center frequency transducer are shown in **Figure 2-4c** for h-RBCs and **Figure 2-4f** for p-RBCs. The shape of the power spectra resembled that of the transducer profile used to filter the NBL spectra generated from **Eq. (2-4)** with a peak frequency of 5 MHz for all aggregation levels. For both cell types, the mean spectral power increased by ~4 dB for the largest aggregate compared to the NAG case. The mean spectral power for p-RBCs was ~1.3 dB higher than h-RBCs for all aggregation levels.

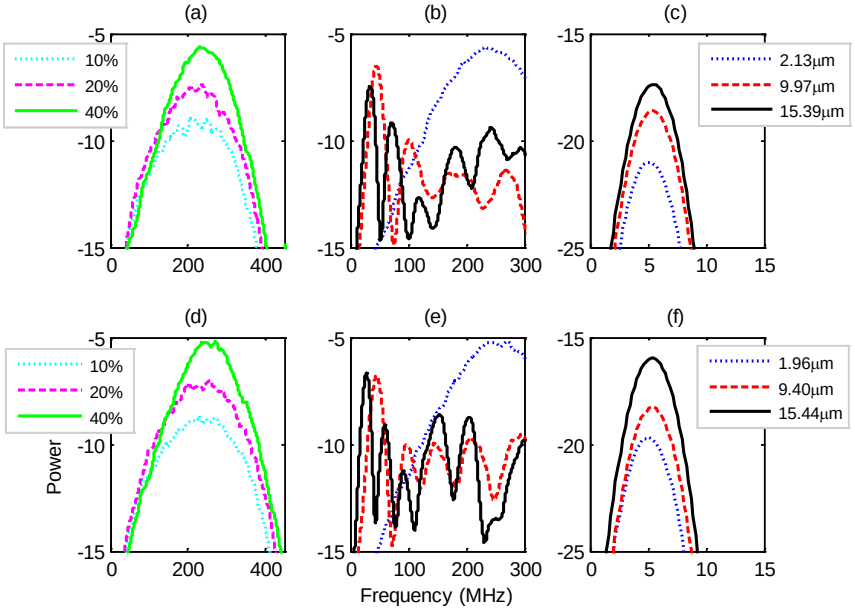


Figure 2-4: Simulated NBL and BL average spectra for NAG and AG RBCs. The top row shows the h-RBCs spectra and bottom row shows the p-RBCs spectra: (a) + (d) NBL NAG, (b) + (e) NBL AG and (c) + (f) BL AG.

### 2.3.2 Experimental results

The experimentally measured PA SA are shown in **Figure 2-5a** for h-RBCs and **Figure 2-5b** p-RBCs. In both cases, the SA followed a non-linear trend with increasing [Dex]. The maximum SA was achieved at a 3 % [Dex] with 1% and 8% concentrations having similar amplitude. For all [Dex], the signal amplitude of h-RBCs was ~1.5 times higher than p-RBCs ($p$ = 0.001). In the case of p-RBCs where the measurements were performed at various hematocrit levels, the SA increased linearly with increasing hematocrit for the NAG case as shown in **Figure 2-5b**. The increase was similar for the other [Dex]. The amplitude at the 3% [Dex] was ~1.6 times higher than the NAG case (0% [Dex]) ($p$ = 0.0002) and ~1.2 and ~1.5 times higher than the 1% and 8% [Dex] at all hematocrit levels ($p$ = 0.0009 and $p$ = 0.001), respectively.

The mean spectral power measured from the experimental PA power spectra are shown in **Figure 2-5c** for h-RBCs and **Figure 2-5d** for p-RBCs. For both cell types, it follows the same non-linear trend observed for the PA SA with increasing [Dex]. The mean spectral power for the h-RBCs at 3% [Dex] was ~5.6 dB higher than the NAG case at 40% hematocrit ($p$ = 0.0003) and ~7.5 dB

higher for p-RBCs at the same concentrations. Compared to 1% and 8% [Dex], the mean spectral power was ~2.3 dB higher for h-RBCs ($p$ = 0.008) and ~4.8 dB higher for p-RBCs ($p$ = 0.0001). For NAG p-RBCs (0% [Dex]), the mean spectral power increased monotonically with increasing hematocrit. A similar trend was observed for all other [Dex].

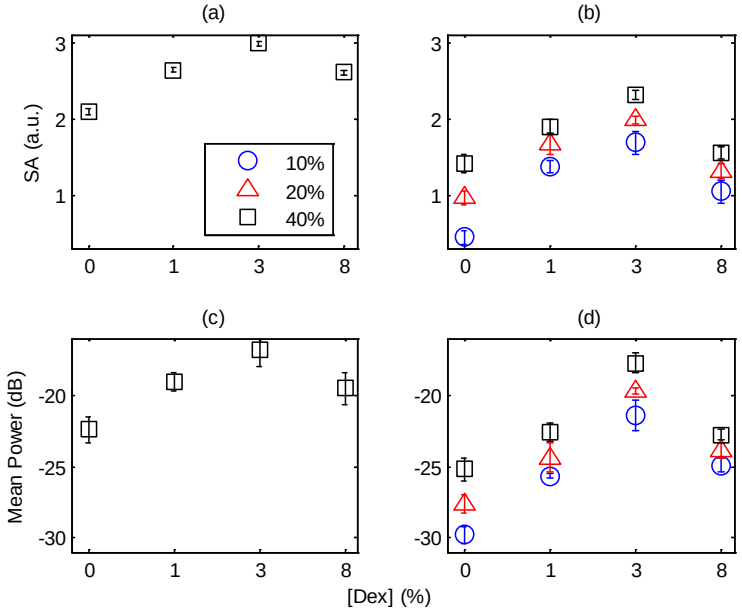


Figure 2-5: Experimental SA ((a) h-RBC and (b) p-RBC) and mean spectral power ((a) h-RBCs and (d) p-RBCs). The error bars represent the standard deviation of 20 PA signals and spectra.

The correlation between the PA SA and viscosity measurements was established by comparing the PA SA of h-RBCs with the viscosity measured at the lowest shear rate (0.05 $s^{-1}$). This is shown in **Figure 2-6** for all [Dex] used in this study. The linear regression of SA with viscosity resulted in a coefficient of correlation $R^2$ = 0.9931. This correlation was statistically significant ($p$ = 0.0069).

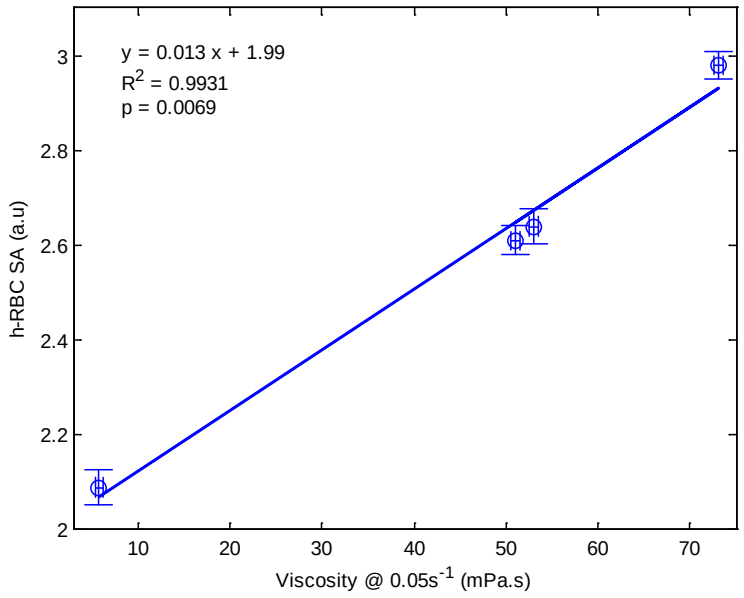


Figure 2-6: Comparison between the PA SA and viscosity of h-RBCs measured at the lowest shear rate (0.05 $s^{-1}$) for all [Dex] used in this study (0, 1, 3 and 8%). The error bars indicate the standard deviation of 20 PA signals and 1 minute of viscosity measurements at 0.05 $s^{-1}$.

## 2.4 Discussion and conclusions

A theoretical and experimental approach is presented here for investigating the potential of PA for detecting and monitoring RBC aggregation. The simulated NBL power spectra of NAG RBCs demonstrated the potential of PA for monitoring RBC samples. For both cell types in the NAG case the spectral power increased over all frequencies when the hematocrit increased (**Figure 2-4a** and **Figure 2-4c**). By increasing the RBC concentration, the SA and spectral power will increase linearly. This can be inferred by inspection of **Eq. (2-3)**: the PA spectral amplitude is computed by the linear superposition of the pressure wavelets that each RBC emits when uniformly irradiated by a laser source. A similar trend in the amplitude of the PA signals with increasing hematocrit has been observed in other experimental studies [124]. This is an advantage of PA over US for monitoring changes in RBC hematocrit. The relationship between US BSC and hematocrit is complex; determining the hematocrit from BSC measurements is difficult. Since the relationship between PA

SA (and spectral power) is linear, determining the hematocrit from the PA amplitude is less complicated.

The advantage of using PA to detect RBC aggregation becomes more apparent when considering the simulated NBL AG power spectra shown in **Figure 2-4b** and **Figure 2-4e** for h-RBCs and p-RBCs, respectively. The frequency of the highest peak of the power spectrum shifted towards lower frequencies (< 30 MHz) when the size of the aggregate increased. For the largest h-RBC aggregate (15.39 μm), the frequency of the peak decreased by ~ 205 MHz from the peak of non-aggregated RBCs (2.13 μm) which occurred at 230 MHz. For the equivalent p-RBC comparison, the frequency decreased by ~243 MHz from the NAG peak which occurred at 265 MHz. It appears as if during the aggregation process, the clustering of the individual RBCs causes the thermal diffusion length to be closer to the RBC separation length. The size of the entire aggregate rather than the individual RBCs controls the features of the power spectra as is apparent from the shift towards the low frequency regime of the peak frequency. Since the origin of the PA signal is the heat transfer between the absorbers and surrounding medium causing the frequencies where the peaks of the power spectra occur to be dependent on the size of the absorber relative to the thermal diffusion length [92].

The simulation results discussed above suggest that PA imaging is capable of differentiating between NAG and AG blood samples. By locating the frequency of the spectral peak, it is possible to monitor the hematocrit of NAG RBCs and formation of aggregates. However, in practice, the ultrasonic transducers used for PA measurements have a finite receiving bandwidth [103]. As shown in **Figure 2-4c** and **Figure 2-4f**, a finite bandwidth transducer significantly affects the PA power spectra (and signals) as it filters out frequencies outside of the transducer sensitivity region. For both cell types, the BL spectra for AG RBCs resemble the shape of the transducer frequency profile centered at 5 MHz regardless of the aggregate size. It is possible to distinguish between the

simulated aggregates as the mean spectral power at 5 MHz increased with increasing aggregate size. However, the significant shifts in the frequency of the peak observed for the NBL case are not present. The lack of the spectral features obtained in BL case indicates the importance of the receiving frequency of the ultrasonic transducer used for PA measurements. The mean spectral power for p-RBC was ~1.3 dB higher than h-RBCs at all aggregation levels since there are more p-RBCs than h-RBCs for any aggregation level. Therefore the signal strength is expected to be larger for p-RBCs than since the PA SA is proportional to the concentration of PA sources.

The experimental results indicate that PA imaging is capable of detecting changes that occur during RBC aggregation. For the NAG p-RBCs, the PA signal increases linearly with increasing hematocrit (**Figure 2-5b**). This behavior is predicted by the theoretical model since the hematocrit is a direct measure of RBC concentration. The non-linear trend in PA SA with increasing [Dex] suggests that PA can distinguish between aggregation levels. Independent measurements of the extent of RBC aggregation as a function of [Dex] have yielded a very similar non-linear trend in the degree of RBC aggregation [125]. The peak obtained in the PA SA and mean spectral power at 3% [Dex] reflects a maximum level of RBC aggregation for both types of RBCs as shown by the increased viscosity of the sample at low shear rates recorded in **Figure 2-1**. This [Dex] is attributed to the affinity of this polymer for inducing aggregation [24]. This was further confirmed by the excellent correlation between the PA SA and viscosity at each [Dex] used as shown in **Figure 2-6**. In comparing the extent of RBC aggregation between h-RBCs and p-RBCs, the PA SA and mean spectral power of h-RBCs is higher at all aggregation levels at 40% hematocrit. This increase is ~1.5 times and it correlates well with other independent studies which confirm that h-RBCs have a higher aggregation tendency than p-RBCs [22]. Analyzing the mean spectral power for both types of RBCs supports the results obtained from the simulation study (**Figure 2-4c** and **Figure 2-4f**) and reinforces the importance of receiving transducer bandwidth in PA measurements.

To the best of our knowledge, PA imaging has never been investigated for detecting and monitoring changes that occur during RBC aggregation. In this study we demonstrate that PA imaging can be used for detecting RBC aggregation. Theoretical simulations suggest that PA spectral analysis can differentiate levels of RBC aggregation and hematocrit. The feasibility of detecting these spectral changes was investigated by incorporating a finite transducer in detection of PA signals. Experimental results indicate that PA is indeed capable of assessing changes that occur during the aggregation process for two types of RBCs.

# Chapter 3 ON THE POTENTIAL OF PA-RFS FOR DETECTING RBC AGGREGATION AND OXYGENATION

## 3.1 Introduction

In this study, the feasibility of PA-RFS to detect changes that occur due to RBC aggregation and assess the oxygenation level of the blood samples is investigated. By using multiple wavelengths of laser illumination, the effect of hematocrit and aggregation level of porcine RBC samples is examined. PA-RFS parameters are computed for both the theoretical and experimental model in order to gain information about the size and concentration of RBC aggregates.

### 3.1.1 Theoretical model

The theoretical basis for the simulations carried out in this study is derived from the analytical solutions of the wave equation for simple geometries illuminated uniformly by a delta function laser pulse [90]. In this case, the RBC is approximated as a spherical absorber and the PA pressure wave emitted from a single sphere and detected at a distance $r$ in the surrounding medium can be written as

$$P_{\text{single}}(\hat{q}) = \frac{i\mu\beta I_0 v_s a^2}{C_P r} \times \frac{\left[\sin\hat{q} - \hat{q}\cos\hat{q}\right]\exp\left[ik_f(r-a)\right]}{\hat{q}^2\left[(1-\hat{\rho})(\sin\hat{q}/\hat{q}) - \cos\hat{q} + i\hat{\rho}\hat{v}\sin\hat{q}\right]} \tag{3-1}$$

**Eq. (3-1)** is written in terms of a dimensionless frequency $\hat{q}$ which is defined as $\hat{q} = \varpi a / v_s$. Here, $a$ is the radius of the spherical absorber, $\varpi$ is the angular frequency of the pressure wave and $v$ is the speed of sound. The subscript $s$ and $f$ denote the sphere and surrounding fluid medium properties, respectively. The dimensionless quantities $\hat{\rho}$ and $\hat{v}$ represent the ratios of the sphere's density and the speed of sound to the surrounding medium's density and speed of sound, respectively. Similarly, $\mu$ is the optical absorption coefficient of the illuminated sphere, $\beta$ is the isobaric thermal expansion coefficient, $C_P$ is the heat capacity per unit mass, $I_0$ is the optical

radiation intensity which varies sinusoidally in time and $k_f$ is the wave number of the surrounding fluid medium.

In the case of more than one absorber, the pressure field from collections of absorbers can be written as the superposition of the waves emitted from each absorber. This approach has been extensively used in modeling the interaction of ultrasonic waves with RBC aggregates [67], [69]. For modeling the PA pressure waves from collections of RBCs it is assumed that all the absorbers within a given ROI become illuminated simultaneously irrespective of their spatial position. When the pressure field of such collection is computed, multiple scattering of the laser illumination beam and the acoustic waves generated are not considered along with acoustic attenuation. With these assumptions, the PA pressure generated from a collection of RBCs can be written as the linear superposition of the spherical waves emitted by the individual absorbers

$$P_{collection}(\hat{q}) = \frac{i\mu\beta I_0 v_s a^2}{C_P} \times \frac{\left[\sin\hat{q} - \hat{q}\cos\hat{q}\right]}{\hat{q}^2\left[(1-\hat{\rho})(\sin\hat{q}/\hat{q}) - \cos\hat{q} + i\hat{\rho}\hat{v}\sin\hat{q}\right]} \times \sum_{n=1}^{N} \frac{\exp\left[ik_f\left(\left|\vec{r} - \vec{r}_n\right| - a\right]\right.}{\left|\vec{r} - \vec{r}_n\right|}. \quad (3\text{-}2)$$

The superposition of the spherical waves is accounted by the summation term of **Eq. (3-2)**. Here, $\vec{r}_n$ represents the position vector of the n$^{th}$ absorber in a ROI which contains $N$ absorbers. If the observation distance is large compared to the size of the ROI, **Eq. (3-2)** can be written as

$$P_{collection}(\hat{q}) = \frac{i\mu\beta I_0 v_s a^2}{C_P} \times \frac{\left[\sin\hat{q} - \hat{q}\cos\hat{q}\right]\exp(ik_f(r-a))}{\hat{q}^2\left[(1-\hat{\rho})(\sin\hat{q}/\hat{q}) - \cos\hat{q} + i\hat{\rho}\hat{v}\sin\hat{q}\right]} \times \sum_{n=1}^{N} \exp\left[-i\vec{k}_f \bullet \vec{r}_n\right]. \quad (3\text{-}3)$$

In practice, PA signals are detected by an ultrasonic transducer that has a finite bandwidth which inherently filters out many of the frequency components of the PA signal. **Eq. (3-3)** does not take into account this finite transducer bandwidth (i.e. it is NBL). This can be accomplished by modeling the transducer frequency response profile by a Gaussian function which resembles the response of typically used transducers [71]. **Eq. (3-3)** then becomes the expression for the BL PA

pressure field for a collection of RBCs by multiplying its pressure by the Gaussian function representing the transducer frequency profile

$$P_{collection}^{BL}(\hat{q}) = P_{collection}^{NBL}(\hat{q}) \times \exp\left[-\frac{(\varpi - \varpi_0)^2}{2\sigma^2}\right]. \quad (3\text{-}4)$$

Here, $P_{collection}^{NBL}(\hat{q})$ is the pressure field computed by **Eq. (3-3)**, $\omega_0$ is the center frequency of the transducer and the width of the Gaussian function $\sigma$ is related to the -6 dB receiving bandwidth of the transducer (chosen to be 60%) by $2\sigma\sqrt{2\log(2)} = 0.6\omega_0$. The PA pressure in the time domain can be derived by taking the inverse Fourier transform of **Eq. (3-3)** and **Eq. (3-4)**.

## 3.2 Methods

### 3.2.1 Simulation methods

The detailed description of the simulation methods employed to generate the PA signals from NAG and AG RBC samples is described in detail in recent reports by our group [122], [123]. For the sake of completeness, the framework of the simulation methods will be discussed here in brief followed by a more detailed account of the modifications of the model for the purposes of this study.

In this study, 2D simulations were performed to investigate the dependence of the PA signals and their respective power spectra on RBC aggregation and oxygenation level. The size of the ROI was chosen to be 200 μm by 200 μm. This can be thought of as a 2D cross-section of a 3D sample containing RBCs. The contributions of the white blood cells and platelets were ignored due to their much smaller concentration and negligible optical absorption compared to RBCs [103]. The spatial locations of the NAG RBCs were generated using a Monte Carlo based technique known as random sequential adsorption [126]. The spatial coordinates of the RBCs were randomly proposed within the 2D ROI and were accepted only if they did not overlap with existing cells under periodic

boundary conditions. This procedure was repeated until all the RBCs at a given hematocrit (defined as the ratio of the area of occupied by the cells to the total area of the ROI) had a fixed position. For generating AG RBC samples, a regular packing scheme was used to arrange individual RBCs into aggregates. Specifically, a hexagonal close packing scheme formed aggregates by positioning the individual RBCs in a hexagonal packing arrangement. The aggregate was then randomly and repeatedly placed within the ROI. For each cluster, the radius of gyration ($Rg$) was computed as a means for quantifying the mean aggregate size. It was calculated by using the square of the distances of the cells from the center of the cluster. Once the spatial positioning of the NAG and AG RBCs was completed, the inverse Fourier transform of **Eq. (3-3)** was computed to obtain the PA signals whose power spectra was then computed for both the NBL and BL case as outlined by **Eq. (3-3)** and **Eq. (3-4)**.

The RBCs simulated in the study were porcine RBCs. They were approximated as fluid spheres with a volume of $68\mu m^3$ and radius $a = 2.53\mu m$ [127]. The density of the cell and the surrounding fluid (water) were taken as $\rho_s = 1078 kg/m^3$ and $\rho_f = 1005 kg/m^3$, respectively. The speed of sound inside the cell was $v_s = 1628 m/s$ and $v_f = 1498 m/s$ in the medium. The thermal parameters and the intensity of the incident optical irradiation were all chosen to have a value of 1 since they only control the amplitude of the signals and not the spectral features.

The PA SA is heavily dependent on the optical absorption of the RBC samples (NAG and AG). The optical absorption depends on the concentration of Hb protein inside the RBC and most importantly on the protein's oxygenation state. Since approximately 189 million Hb molecules reside within a single porcine RBC, the concentration of Hb inside a single cell was calculated to be $[Hb] = 4.62 \times 10^{-3} mol/L$. Hb can be either bound up to 4 molecules of oxygen or none and its

optical absorption coefficient can be estimated by employing the following relationship: $\mu = [OHb]\varepsilon(OHb) + [DHb]\varepsilon(DHb)$, where $\varepsilon$ is the extinction coefficient for each Hb molecule (depending on its oxygenation level) [128]. For this study, the samples of blood simulated (NAG and AG) were assumed to be either entirely oxygenated or entirely deoxygenated. By taking into account the extinction coefficients at 750 and 1064 nm for both OHb and DHb, the optical absorption coefficients were calculated and utilized in computing the pressure field given by **Eq. (3-3)**. **Table 3-1** presents the estimated absorption coefficients used in this simulation study [128].

| **Wavelength (nm)** | **$\mu_{OHb}$ ($m^{-1}$)** | **$\mu_{DHb}$ ($m^{-1}$)** |
|---|---|---|
| 750 | 260.57 | 702.24 |
| 1064 | 405.17 | 49.90 |

Table 3-1: Absorption coefficients for oxygenated and deoxygenated RBCs.

The effect of hematocrit and aggregation level was examined in addition to the oxygenation state of the samples at both wavelengths. For each hematocrit level, three different levels of aggregation were simulated. The smallest $Rg$ value corresponds to the NAG case. Since the simulations were based on a Monte Carlo method, placing the exact same number of RBCs within a given aggregate becomes difficult so the $Rg$ values for each hematocrit level are not identical. **Table 3-2** summarizes the aggregation levels (characterized by $Rg$) for each hematocrit level simulated in this study.

| **Hematocrit (%)** | **Radius of gyration (μm)** | | |
|---|---|---|---|
| 10 | 1.96 | 7.15 | 10.96 |
| 20 | 1.96 | 7.65 | 10.96 |
| 40 | 1.96 | 7.65 | 10.51 |

Table 3-2: Hematocrit and aggregation levels simulated in this study.

### 3.2.2 Blood sample preparation

The guidelines on handling the blood were followed in accordance to the recommendations of the International Society for Clinical Hemorheology and the European Society for Clinical Hemorheology and Microcirculation [27]. Fresh porcine blood from the femoral vein of Yorkshire pigs (Comparative Research, Toronto, ON) was drawn into spray-coated potassium EDTA vacutaners (Becton, Dickinson and Company, Franklin Lakes, NJ). The blood was centrifuged (1500g, 6 min at room temperature) to separate the plasma and the buffy coat. Isotonic photsphate buffered saline (PBS) was used to wash the RBCs two times. The packed RBCs were then suspended in PBS in order to achieve 3 hematocrit levels (10, 20 and 40%). For each hematocrit level, aggregation was induced by replacing PBS with a solution of Dextran-70 (Sigma-Aldrich, St. Louis, MO) dissolved in PBS. By changing the concentration of the Dextran-PBS ([Dex]) solution, varying degrees of aggregation were achieved. For this study, the [Dex] used were 1, 3 and 8% (wt/vol). The presence of aggregation was assessed using an Olympus CKX41 optical microscope (Olympus Canada Inc., Markham, ON) at 40X magnification. Representative images of NAG and AG RBCs (at 3% [Dex]) are shown in **Figure 3-1**. All blood samples were kept in contact with air prior to experimentation and all experiments were completed within 4 hours of blood sampling.

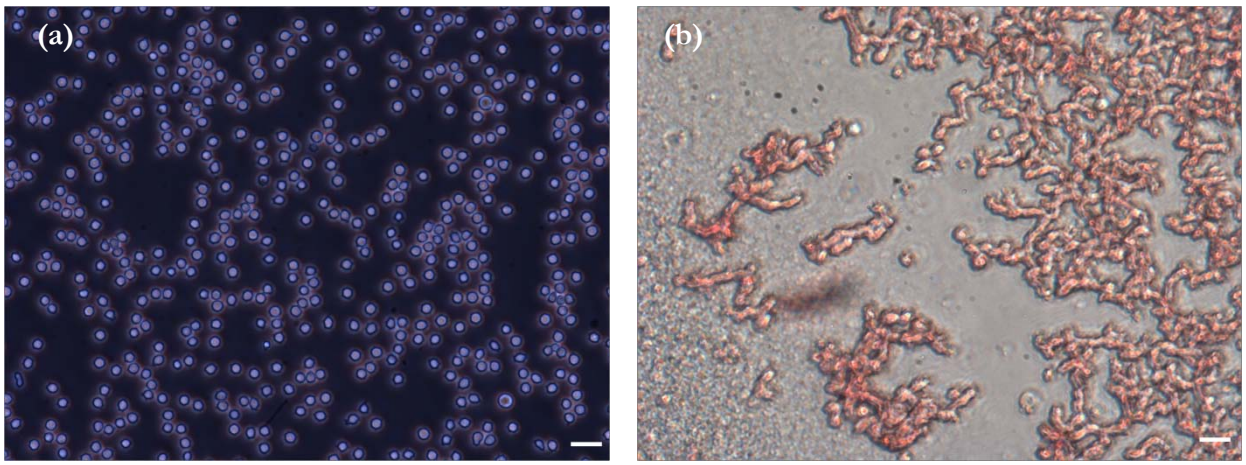


Figure 3-1: (a) NAG p-RBCs suspended in PBS and (b) AG p-RBCs suspended in 3% [Dex]. The scale bar denotes 10 μm.

### 3.2.3 Experimental setup

The Imagio Small Animal PA imaging device (Seno Medical Instruments, Inc., San Antonio, TX) was used to measure all the PA signals analyzed in this study. The system consisted of a Q-switched, pulsed Nd:YAG laser delivered through an articulated arm (beam width 9 mm, pulse width 6 ns, pulse repetition rate 10 Hz, maximum fluence 25 $mW/cm^2$/pulse). The acoustic receiver consisted of a 4 channel, annular array transducer with a center frequency of 5 MHz and a -6 dB bandwidth of 60%, as measured by using a hydrophone as the source of sound. The transducer was mounted 60 mm coaxially to the laser allowing for raster scanning over the entire ROI.

The blood samples were loaded into cylindrical tubes (Norton Performance Plastic, Akron, OH) with 0.5 mm inner diameter. A vertical raster scan was performed over the entire tube length (10 cm). At each location, the laser fired 4 pulses which were averaged to produce a single PA RF line. A total of 20 signals were recorded for each blood sample irradiated at 750 and 1064 nm. The PA signal from columns filled with distilled water was also recorded in order to confirm that the signals analyzed were from the presence of RBCs and not the sample container (which produced sub-noise signal).

In order to obtain the transducer frequency response profile for PA measurements, a 200 nm thick gold film was used. The film was deposited onto a thin microscope cover slide with no annealing. The gold film was used because it has a broad PA power spectrum as well as a flat response in the known bandwidth of the transducer thus providing a good measure of the transducer response in PA measurements. The laser was raster scanned over an area of ~0.25 $cm^2$ at both 750 and 1064 nm wavelengths using the same power settings as the PA measurements of the blood samples. A total of 20 PA signals were recorded for each wavelength.

### 3.2.4 Data analysis

The analysis methodology described here was applied to both the theoretical and experimental signals. Each PA signal recorded was multiplied by a Hamming window in order to localize the signal either in the theoretical model (ROI 200 μm by 200 μm) or the sample holder (0.5 mm) and to minimize spectral leakage. For each signal (250 simulated signals and 20 experimental signals), the SA was computed by integrating the envelope of each signal (obtained by taking the Hilbert transform). The average and standard deviation of the SA was then computed. For each PA signal, the Fourier transform was computed using the Fast Fourier Transform algorithm before converted to a logarithmic (dB) scale.

The power spectra for each signal were then normalized to the frequency response of the transducer used. The theoretical spectra were subtracted from the Gaussian function (converted to dB scale) used to model the transducer frequency response as shown by **Eq. (3-4)**. The experimental spectra were subtracted from the gold film spectrum for the appropriate wavelength of illumination. Linear regression was performed on the quasi-linear, normalized power spectra over the -6 dB bandwidth of the transducer. The SS and MBF were computed from the linear fit of each normalized spectrum. Averages of each of these parameters along with the standard deviations were computed. The normality of the data was confirmed using a Shapiro-Wilk test with $W > 0.05$ used as the criterion for normality. An unpaired t-test was used to compare the PA SA and spectral parameters obtained from NAG and AG RBCs at each respective oxygenation level. A $p$-value of 0.05 or less was used to establish statistically significant differences.

3.2.5 Estimation of oxygen saturation

The oxygen saturation ($SO_2$) for a sample of blood can be estimated by illuminating the sample with two optical wavelengths ($\lambda_1$ and $\lambda_2$) and measuring the PA SA at each wavelength [103]. Assuming that OHb and DHb are the dominant absorbers at the two wavelengths, the $SO_2$ was calculated by

$$SO_2 = \frac{[OHb]}{[OHb]+[DHb]} = \frac{SA(\lambda_2)\times\varepsilon(DHb,\lambda_1) - SA(\lambda_1)\times\varepsilon(DHb,\lambda_2)}{SA(\lambda_1)\times\Delta\varepsilon(\lambda_2) - SA(\lambda_2)\times\Delta\varepsilon(\lambda_1)}. \quad (3\text{-}5)$$

Here, $\Delta\varepsilon(\lambda) = \varepsilon(OHb,\lambda) - \varepsilon(DHb,\lambda)$ is the difference in the extinction coefficients for each wavelength of illumination ($\lambda_1 = 750nm$ and $\lambda_2 = 1064nm$). $SA$ represents the average amplitude of the experimental PA signals. The $SO_2$ was calculated for all measured PA signals and reported as percentage.

## 3.3 Results

3.3.1 Simulated power spectra

**Figure 3-2** shows the average power spectra obtained from the PA signals of 250 NAG (top row) and AG (bottom row) RBC random configurations illuminated. The RBC samples were fully oxygenated and were illuminated at 750 nm. As seen in **Figure 3-2a** for the NAG NBL case, the spectral power generally increases over all frequencies when the hematocrit was increased. As expected by inspection of **Eq. (3-3)**, all frequencies generated by the NAG RBCs were present in the power spectra and the dominant peak of each spectrum was observed at ~260 MHz. The spectral power increased by ~2.3 dB per doubling hematocrit level at 260 MHz. When the effect of a finite bandwidth transducer was taken into account, most frequencies present in the NBL spectra were filtered out as shown in **Figure 3-2b**. Using the frequency response of a 5 MHz center frequency transducer to filter the NBL spectra resulted in NAG BL power spectra which resembled

the transducer frequency profile. The spectral power increased by 1.7 dB per doubling hematocrit level at 5 MHz. In order to normalize the power spectra, the BL spectra were divided by the Gaussian-shaped transducer frequency response and the spectra in **Figure 3-2c** were obtained. The normalized spectra were linear around the 5 MHz, -6 dB transducer sensitivity region and a linear regression line was fitted in order to obtain the SS and MBF.

The AG, NBL power spectra are shown in **Figure 3-2d** for samples at 40% hematocrit and for different aggregate sizes. As the size of the aggregates (measured by $Rg$) increased, the frequency at the peak of the spectrum decreased. Specifically, the frequency of the peak for the NAG case (1.96 μm) was 260 MHz, 45 MHz for the 7.15 μm and 30 MHz for the 10.96 μm aggregates. The BL spectra for the AG samples are shown in **Figure 3-2e**. The spectral shifts present in the NBL case were no longer identifiable and the overall shape resembled the transducer frequency profile (similar to the NAG case (**Figure 3-2b**). At 5 MHz, the spectral power increased by 1.8 dB and 3.3 dB for the 7.15 and 10.96 μm aggregates compared to the NAG sample. The normalized spectra for the AG samples shown in **Figure 3-2f** were fitted to a linear regression line and the spectral parameters were obtained.

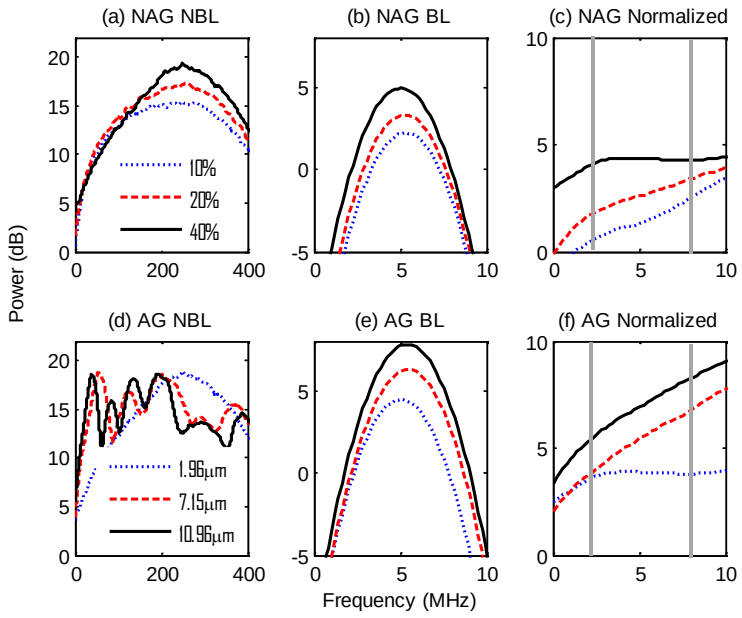


Figure 3-2: Simulated power spectra for oxygenated NAG and AG RBC configurations illuminated at 750 nm. Top row: (a) NBL power spectra for NAG RBCs at 3 hematocrit levels, (b) BL and (c) normalized power spectra of (b). Bottom row: (d) NBL power spectra for AG RBCs at 3 aggregation levels and 40% hematocrit, (e) BL and (f) the normalized power spectra of (e). The lines on (c) and (f) represent the usable transducer bandwidth over which linear regression was performed.

### 3.3.2 Quantitative parameters for simulated samples

A quantitative summary of the SA, SS and MBF for the simulated exposures at 750 nm is shown in **Figure 3-3**. All graphs are plotted as a function of hematocrit for each aggregate size (Rg of 2, 8 and 11 μm) and oxygenation state (oxy and deoxy). As shown in **Figure 3-3a**, the SA increases monotonically with increasing hematocrit for all aggregation and oxygenation levels. Specifically, the increase is ~1.5x per doubling hematocrit level. The SA for all deoxygenated samples is ~2.7x higher than oxygenated ones ($p$ = 0.0004). An increase of >2x is observed for AG samples compared to NAG ones at both oxygenation states and all hematocrit levels ($p$ = 0.0002).

The SS (obtained from the line of best fit to the normalized spectra) is shown in **Figure 3-3b** for the 750 nm exposure. As the hematocrit increased, the SS did not change in a statistically significant manner when comparing the NAG with AG samples ($p$ = 0.08). The trend was similar

for both oxygenated and deoxygenated samples. In addition, there was no statistically significant change when comparing the NAG samples with AG samples (8 and 11 μm) ($p$ = 0.8). For the NAG samples, the average SS over all hematocrit levels was ~0.35 dB/MHz.

In the case of the MBF, there was a monotonic increase with increasing hematocrit level in a very similar manner to the increase in PA SA (**Figure 3-3c**). The MBF increased by ~1.3 dB per doubling hematocrit level for all aggregation levels and both oxygenation states. AG samples had an MBF >4.3 dB than NAG samples at all hematocrit and oxygenation states ($p$ = 0.0005).

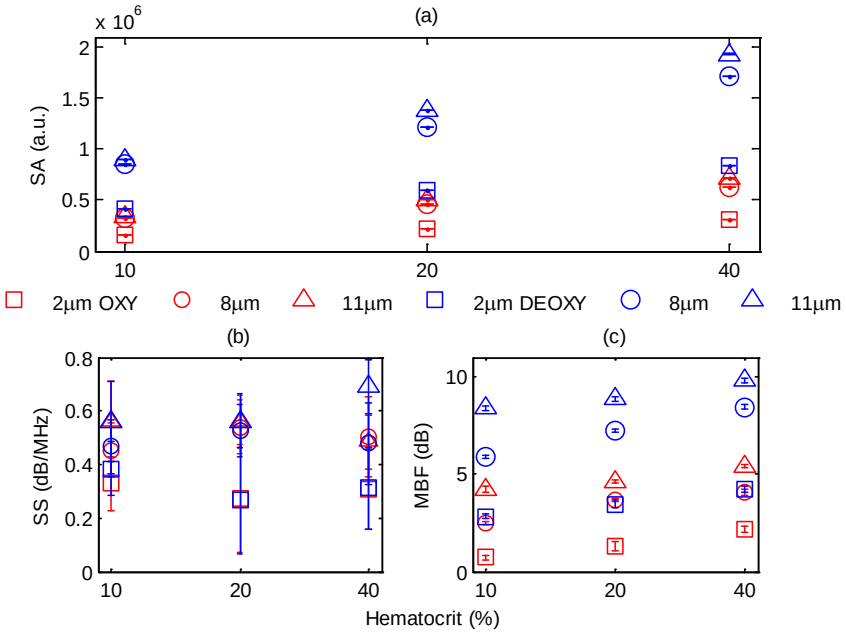


Figure 3-3: (a) SA, (b) SS and (c) MBF for the 750 nm laser exposure as a function of hematocrit, aggregate size and oxygenation level. The error bars (too small to be seen in (a)) denote the standard deviation for 250 PA signals or spectra.

The quantitative summary of the SA, SS and MBF for the 1064 nm exposure are shown in **Figure 3-4**. All oxygenated samples had a SA ~8x greater than the deoxygenated samples ($p$ = 0.0001) and increased by ~1.5x per doubling hematocrit level for all aggregate sizes (**Figure 3-4a**). The AG samples were > 2x higher in SA compared to NAG samples for all hematocrit and oxygenation levels ($p$ = 0.0006). Compared to the 750 nm exposure, the oxygenated RBC samples at

1064 nm had a SA ~1.6x greater at all aggregation and hematocrit levels ($p$ = 0.0008). The trend was reversed for the deoxygenated samples with the SA being ~14.1x greater for the 750 nm exposure ($p$ = 0.0001).

The SS (shown in **Figure 3-4b**) followed similar trends to the 750 nm exposure with no statistically significant changes between NAG and AG samples when the hematocrit increased from 10 to 40% ($p$ = 0.8). Oxygenated and deoxygenated samples were not statistically significantly different from one another ($p$ = 0.1). The average SS over all hematocrit levels was ~0.35 dB/MHz.

For every doubling of the hematocrit level, the MBF increased by ~1.2 dB for all aggregation and oxygenation states at 1064 nm laser exposure (**Figure 3-4c**). An increase > 4.3 dB was observed when comparing the AG with NAG samples at all hematocrit and oxygenation ($p$ = 0.0007). The MBF of the oxygenated RBC samples at 1064 nm was ~2 dB higher than the 750 nm ($p$ = 0.0009) while the MBF of deoxygenated samples at 1064 nm was ~11 dB lower than the 750 nm counterpart ($p$ = 0.0001). The trend was true for all hematocrit and aggregation levels.

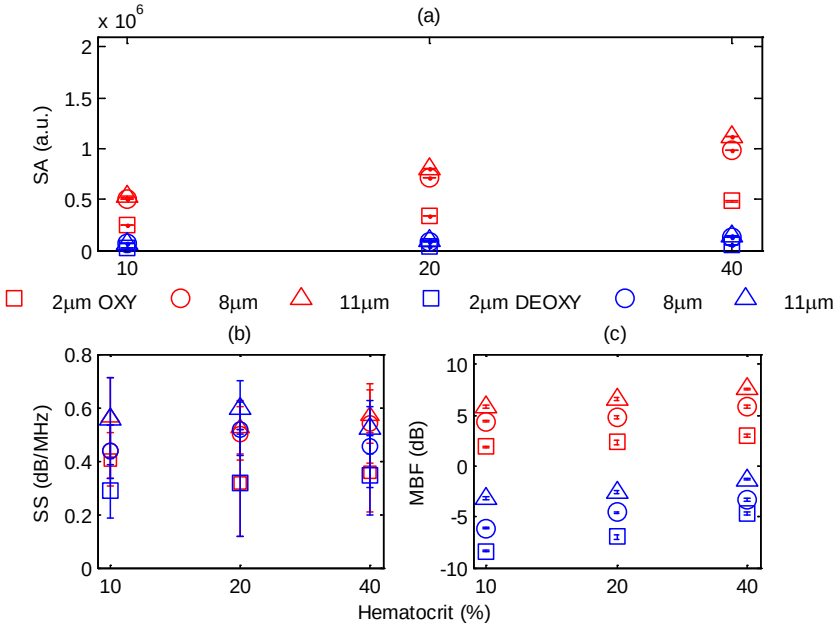


Figure 3-4: (a) SA, (b) SS and (c) MBF for the 1064 nm laser exposure as a function of hematocrit, aggregate size and oxygenation level. The error bars (too small to be seen in (a)) denote the standard deviation for 250 PA signals or spectra.

### 3.3.3 Experimental SA and oxygenation level

The experimentally measured PA SA and oxygenation levels (calculated using **Eq. (3-5)**) for all samples is shown in **Figure 3-5**. For both wavelengths of illumination 750 nm (**Figure 3-5a**) and 1064 nm (**Figure 3-5b**), the SA increased monotonically with increasing hematocrit. The increase was ~1.3x per doubling hematocrit level. As the aggregation level was varied (by changing [Dex]), the PA SA exhibited a non-linear trend. The maximum SA was achieved for a [Dex] of 3% for all hematocrit levels. The 1 and 8% [Dex] exhibited nearly identical SA ($p = 0.2$). The SA for NAG samples ([Dex] 0%) was at least 1.6x smaller than the AG samples at all hematocrit levels, for both wavelengths of illumination ($p = 0.001$). At the 750 nm exposure, the SA was ~1.3x greater than the 1064 nm exposure for all samples measured ($p = 0.003$).

**Figure 3-5c** shows the $SO_2$ calculated by utilizing Eq. (3-5) with both exposure wavelengths. $SO_2$ increased linearly with increasing hematocrit with an average increase of ~7% per doubling hematocrit level. At the 3% [Dex], $SO_2$ was at the highest level ~30% higher than the NAG case ($p = 0.00001$). The 1% and 3% [Dex] $SO_2$ levels were virtually identical at all hematocrit levels and ~20% higher than the NAG samples ($p = 0.00003$).

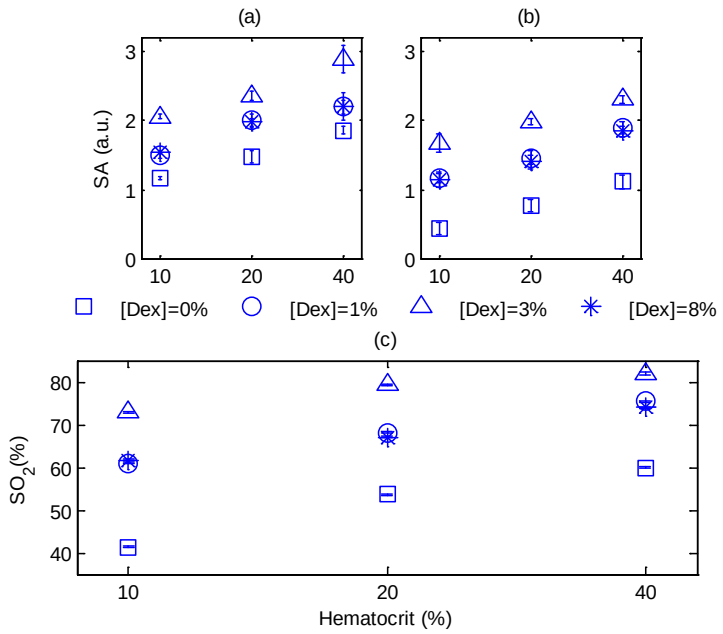


Figure 3-5: Experimentally measured PA SA and $SO_2$ levels for all RBC samples. The error bars denote the standard deviations of 20 PA signals. Top row: PA SA for the (a) 750 nm and (b) 1064 nm exposures. Bottom row: (c) $SO_2$ for all RBC samples illuminated at both wavelengths.

### 3.3.4 Experimental spectral parameters

The spectral parameters measured from the experimental power spectra at both exposure wavelengths are shown in **Figure 3-6**. As seen in **Figure 3-6a** and **Figure 3-6b**, the SS does not change with increasing hematocrit ($p$ = 0.3). At both wavelengths of illumination the SS values were approximately equal. The SS decreases by a factor of 9 when the [Dex] was 3% compared to the NAG case when [Dex] was 0% at all hematocrit levels ($p$ = 0.0002). The SS at 3% [Dex] is ~0.1 dB/MHz lower than the 1% and 8% [Dex] ($p$ = 0.001).

The MBF for both wavelengths of illumination is shown in **Figure 3-6c** and **Figure 3-6d**. It monotonically increased with increasing hematocrit and it reached a maximum value for the 3% [Dex]. For both wavelengths, the increase was ~1.2x per doubling hematocrit levels. At 3% [Dex] the MBF was ~6 dB higher than the NAG case ($p$ = 0.0004) and ~4 dB higher than the 1% and 8% [Dex] (which had approximately the same MBF) ($p$ = 0.0007). This trend was observed for both

wavelengths. The MBF for the 750 nm exposure was ~1.2x higher than the 1064 nm exposure at all hematocrit and aggregation levels ($p$ = 0.003).

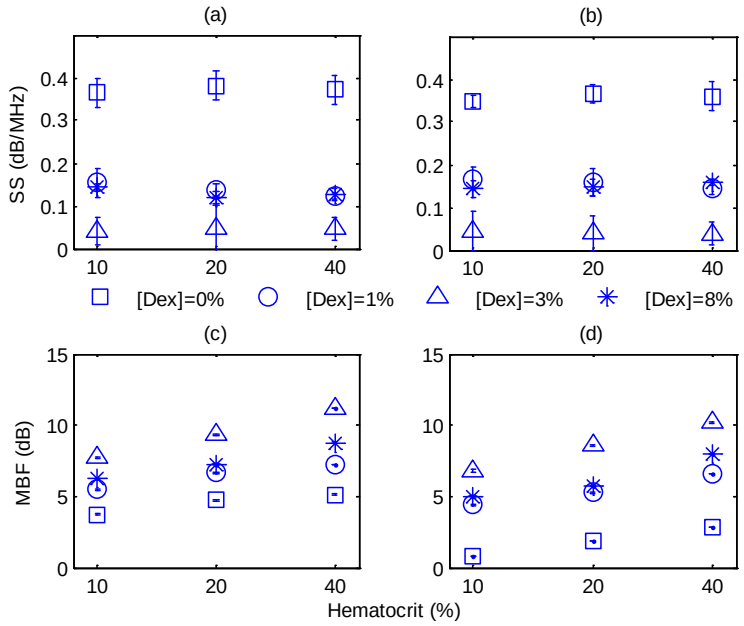


Figure 3-6: Experimentally measured SS and MBF for all RBC samples. The error bars denote the standard deviations of 20 PA spectra. Top row: SS for the (a) 750 nm and (b) 1064 nm exposures. Bottom row: MBF for the (c) 750 nm and (d) 1064 nm exposures.

## 3.4 Discussion and conclusions

The findings of this study demonstrate the potential of PA-RFS for detecting and monitoring changes due to the aggregation of RBCs while providing information on their oxygenation levels. The theoretical model developed here examined how the aggregation level and oxygenation status of RBCs affect the spectral features of the PA signals detected. By investigating both phenomena simultaneously, we have extended the theoretical model already developed for studying aggregation and oxygenation independently [122], [123]. The theoretical model was further improved by taking into account the effect of a finite transducer bandwidth on the PA signals and power spectra. This allows the model comparisons with experimental data with more fidelity since PA experiments are conducted using transducers with a finite frequency response. In addition, by utilizing a commonly

used experimental protocol [27], this study tests the capability of PA for detecting and monitoring changes that occur during RBC aggregation while providing information on the oxygenation status of the samples. Performing PA at multiple wavelengths also allows for simultaneous measurements of the oxygenation level of the RBCs during aggregation. Currently, no other available imaging modality is capable of detecting the aggregation of RBCs and measuring the $SO_2$ simultaneously. There has been significant evidence demonstrating decreased release of oxygen during the presence of RBC aggregation and its implications on tissue oxygenation [129–131]. Furthermore, by normalizing the power spectra with the transducer frequency response, the system dependencies on the detection process can be removed. By using spectroscopic methods of analysis derived from UTC [117], [115], a quantitative method that can be potentially used for assessing the size and concentration of RBC aggregates was developed.

The theoretical model developed here is part of the first ever study of the effect of RBC aggregation and oxygenation level on the PA RF signals and their respective power spectra. Beginning with the NAG RBCs (**Figure 3-2a**), the monotonic increase observed in the SA with increasing hematocrit has been confirmed by other experimental studies [124]. Increasing the number of optical absorbers increases the spectral power (and SA) linearly since it is calculated from the linear superposition of the spherical wavelets emitted from each individual RBC. The straightforward relationship between SA and hematocrit (**Eq. (3-3)**) is an advantage of PA imaging over its US counterpart for the study of RBC concentration. In US imaging, the backscattered power dependence on hematocrit resembles a Gaussian profile and it depends on the spatial distribution of the RBCs and the interrogating US frequency [74]. This renders US measurements of RBCs difficult since it is nearly impossible to assess the level of hematocrit from the backscattered US power alone. Being able to do that using PA presents significant advantages when it comes to measurements of

RBC aggregation, which is a hematocrit-dependent process. In PA the size of the optical absorber is responsible for controlling the dominant frequency of the power spectrum [90]. As shown in **Figure 3-2d**, PA spectra can differentiate RBC aggregates based on their sizes. When RBCs aggregate, the spatial separation of the individual RBCs approaches the thermal diffusion limit which is controlled from the physical parameters of the RBCs and surrounding medium [132]. This causes the entire aggregate to act as an individual PA source even though the generation of the PA signal is still due to the absorption and thermal expansion of the individual RBCs. It is highly advantageous to differentiate sizes of objects based on the spectral content of PA RF signals.

However, despite the fact that the NBL results presented in **Figure 3-2a** and **Figure 3-2c** suggest significant changes in power spectra due to the presence of RBC aggregation, they are simply ideal, theoretical scenarios of a more complex detection process. US transducers have a finite receiving bandwidth that inherently filters out many of the frequency components generated from PA sources [103]. The results presented in **Figure 3-2b** and **Figure 3-2e** strongly suggest that the transducer used clearly affects the PA signals received as the dominant spectral features predicted by the NBL equations are no longer present. Nevertheless, using a 5 MHz transducer that is commonly used for PA measurements demonstrates the ability to detect significant changes in the power spectra of NAG and AG RBCs. The experimentally measured power spectra also conducted with a 5 MHz center frequency transducer closely resembled the shape of the transducer frequency response, as predicted. Our group has also conducted PA measurements on single RBCs with high frequency transducers (center frequency 205 and 375 MHz) and the bandwidth of the transducer has been shown to significantly affect features of the recorded PA signals [133].

Normalizing the simulated and experimental power spectra by the transducer frequency response provides a means of obtaining quantitative parameters which are related to structural

features of the samples being interrogated. The normalized power spectra shown in **Figure 3-2c** and **Figure 3-2f** can be fitted to a linear curve over the usable transducer bandwidth and regression analysis can provide the SS and MBF. The results obtained could be interpreted using what is already known from UTC since both PA and US imaging share similarities in the detected signals. In UTC, the SS is primarily related to the scatterer size and shape. The MBF is a measure of the US backscatter and primarily depends on the scatter concentration [115]. In the case of PA imaging, the absorber size and concentration can also be related to parameters that can be obtained from the spectroscopic analysis of PA signals.

Despite the fact that the theoretical SS (**Figure 3-3b** and **Figure 3-4b**) was not statistically significantly different between NAG and AG samples, it would still be appropriate to compare the SS for simulated NAG RBC samples with experimental NAG samples in order to further validate the theoretical model. It was still possible to distinguish between the various hematocrit and aggregation levels using the MBF parameter despite no shifts in the frequency of the power spectra. The monotonic increase in the MBF with increasing hematocrit is in accordance to the trends followed by the PA SA. This is expected since the MBF is a measure of absorber (i.e. RBC) concentration. In addition, as the aggregation level increased, the MBF significantly increased compared to the NAG case. The increase corresponded to the fact that the signal strength for AG RBCs in the low frequency regime increases more than the NAG case as observed in the power spectral shifts of NBL spectra (**Figure 3-2c**). Experimental measurements of the spectral parameters also reveal significant differences between NAG and AG RBC samples (**Figure 3-5**). The decreases in the SS as the [Dex] increased can be interpreted by the increase in the aggregate sizes which are controlled by the [Dex]. At 3% [Dex] the SS is at a minimum for both wavelengths which suggests that the size of the aggregate is at a maximum (**Figure 3-5a** and **Figure 3-5b**). Such a result is expected since other experimental assessments of the effect of RBC aggregation on [Dex] have

resulted in the aggregates with the largest sizes forming with a [Dex] of 3% [125]. The SS parameter is a measure of the scatterer size in UTC and it decreases with increasing scatterer size [115]. In addition, the SS for the NAG case at all hematocrit levels is nearly identical to the SS predicted by the theoretical results (~0.3 dB/MHz). This suggests that the theoretical model developed here is accurately emulating experimental conditions. The comparison between the theoretical and experimental NAG SS parameter could be used to evaluate the ability of the theoretical model to simulate the PA signal from NAG RBCs. At the frequency regime where the experimental transducer is most sensitive (< 10 MHz), the experimental spectra and the NAG theoretical spectra are nearly identical since they are heavily affected by the transducer sensitivity curve. This gives rise to the good agreement between the experimental and theoretical SS parameter. Such agreement in SS could be due to the fact that the model used here takes into account a finite ROI filled with spherical absorbers at the appropriate concentration (i.e. hematocrit) which represent NAG RBCs. Experimentally, a collection of NAG RBCs inside a cylindrical container could be, to a good approximation, be seen as a collection of absorbing spheres much like what is simulated. For the AG case, the spectral parameters between the model and the experiment could not be directly compared. The presence of the largest aggregates was also confirmed by the significant increases in the MBF when comparing the NAG samples to the AG ones (**Figure 3-5c** and **Figure 3-5d**). The largest MBF was observed for the 3% [Dex] samples at all hematocrit levels in a very similar fashion to the SA trend. This is expected since the MBF is a direct measure of the PA SA and is dependent on the absorber concentration. In addition, since aggregation is a hematocrit dependent process, the observable changes in the MBF reflect the linear relationship that exists between RBC concentration and the strength of the PA signal measured. This is a clear advantage of PA imaging for measuring RBC aggregation since other techniques are not sensitive enough to measure hematocrit levels of aggregated RBC samples [47]. The theoretical SS parameter showed significant differences compared

to the experimentally measured one. Such deviation could be interpreted from the fact that the theoretical model for aggregation is forming spherical aggregating clusters by placing individual RBCs close to one another. This approach could be responsible for the discrepancy between the SS parameter which did not change for theoretical spectra as the aggregate size increased as shown in **Figure 3-3** and **Figure 3-4**. RBC aggregates observed experimentally showed both a combination of rouleux and spherical clusters of varying sizes as shown in **Figure 3-1**. It is thus expected that the detected signals will be a convolution of the PA response of the shapes of the varying aggregates and the transducer response. The theoretical model does not take into account the varying sizes of aggregates nor does it simulate the more realistic rouleaux or clusters that are observed experimentally. For direct comparisons with experiment, the theoretical model should be improved to take into account the more appropriate 3D shapes of aggregates.

PA-RFS is successful in measuring the oxygenation level of RBC samples in addition to monitoring their aggregation. The theoretical results obtained from fully oxygenated and deoxygenated samples at two illumination wavelengths strongly demonstrate the potential of PA for differentiating the oxygenation levels of RBC samples. The changes in SA and MBF are significant enough to differentiate between the two oxygenation levels (**Figure 3-3** and **Figure 3-4**). Differences between oxygenated and deoxygenated samples at both wavelengths correspond to the differences that exist between the absorption coefficients at each wavelength. The theoretical results on oxygenation suggest that two-wavelength PA allows to measure $SO_2$ while simultaneously assessing the presence of RBC aggregation. As seen in **Figure 3-5c**, the $SO_2$ increases by more than 20% when RBCs aggregate. This suggests that the presence of aggregation decreases the ability of RBCs to release oxygen to the surrounding environment. Such an observation has important implications for oxygen transfer from RBCs to surrounding tissues. In the presence of RBC

aggregation, the plasma layer surrounding the RBCs which helps reduce the frictional interaction with the endothelial cells of the blood vessels increases in thickness [130]. This impairs the diffusion of oxygen to the surrounding tissues thus increasing the $SO_2$ level. Such increases have been measured experimentally using a microscope system coupled with a spectrophotometer [129]. Enhancements in the $SO_2$ were found to be similar to the ones reported in this study and dependent on the aggregation and hematocrit level.

This study demonstrates for the first time the potential of PA-RFS to detect changes due to RBC aggregation and oxygenation. In this investigation, we have been able to demonstrate the PA detection of RBC aggregation for specific degrees of aggregation levels and hematocrit while simultaneously measuring the oxygen level for each sample. The PA-RFS techniques developed here suggest that it is possible to obtain quantitative measures of aggregate size and concentration. To the best of our knowledge, this is the first time that PA imaging has been used for the investigation of RBC aggregation and oxygenation. The results of this study suggest the potential of PA as a non-invasive tool for detecting RBC aggregation.

# Chapter 4 CONCLUSIONS AND FUTURE DIRECTIONS

## 4.1 Thesis conclusions

The focus of this thesis was to assess the feasibility of PA imaging for the detection and monitoring of RBC aggregation. All the thesis objectives outlined in the introduction were investigated. This work demonstrated for the first time that PA imaging has potential as a non-invasive tool for detecting RBC aggregation.

Specifically, it was shown that by monitoring the power spectra of PA RF signals one can obtain information that can be related to the presence of RBC aggregation. The theoretical model developed here elucidated on using the frequency-domain information contained in the PA RF signals for detecting RBC aggregates. The size of the aggregate dictated the dominant frequency content of the PA signals. The larger the size of the aggregate, the greater was the shift of the dominant frequency towards clinical frequencies (< 30 MHz). Such an observation suggested that PA measurements commonly performed using clinical US transducers can differentiate between NAG and AG RBCs. The feasibility of this technique was experimentally investigated using two types of RBCs (p-RBCs and h-RBCs) and significant changes were observed in the power spectra for varying aggregation and hematocrit levels.

The theoretical model was improved by taking into account the finite nature of the transducer bandwidth in order to simulate more realistic PA measurements. This allowed for the development of PA-RFS techniques whose basic premise is taking into account the transducer frequency response. In accomplishing the normalization of the simulated and experimentally measured PA power spectra, PA-RFS provided quantitative parameters that could be potentially related to structural properties of the RBC samples. The SS and MBF parameter extracted from the normalization procedure were related to the size and concentration of the optical absorbers as

shown by the phantom experiments. These two parameters were then used to monitor the changes occurring due to RBC aggregation. The SS decreased with increasing aggregate size while the MBF increased. It was possible to quantify the change in hematocrit and aggregation levels by extracting the spectral parameters. This was the first time that PA-RFS has been used to quantify RBC concentration during PA measurements.

Finally, two-wavelength PA-RFS was used in order to obtain the oxygenation level of RBC samples during aggregation. The presence of RBC aggregation has been associated to decreased oxygen transfer to surrounding tissues but no current techniques exist that are capable of detecting the presence of RBC aggregation and simultaneously provide the $SO_2$ level. The results of this study suggested that $SO_2$ level significantly increases during RBC aggregation in accordance to previously published studies [129]. This study demonstrates the potential of PA imaging for detecting morphological and functional changes occurring due to RBC aggregation.

## 4.2 Future directions

The results presented in this thesis are the first-ever observations on the PA detection of RBC aggregation. In order to further explore the potential of PA for detecting RBC aggregation several theoretical and experimental investigations are required. They are summarized below:

1. Establish the relationship between the spectral parameters extracted in PA-RFS and physical properties of samples being imaged: This will be required in order to obtain physically meaningful quantitative parameters that can be used to monitor size and concentration of optical sources in a similar fashion to UTC. A preliminary investigation is presented at the end of this section.

2. Extend the theoretical model to 3D: This will allow for more realistic representations of aggregates since in reality clusters of RBCs form during periods of decreased blood flow. Although the resulting model will have increased computational requirements, it will also provide more insight into the PA spectral signatures from more realistic aggregates. In addition, it would be noteworthy to simulate aggregates with sizes closely resembling the ones measured during experiments in order to allow for more accurate comparisons.
3. Perform measurements using various types of RBCs and aggregating conditions: This will test the sensitivity of PA techniques for detecting RBC aggregation. Various types of mammal RBCs (i.e. horse or rat) exhibit significantly different aggregation behaviours and it would be important to test the capabilities of PA in monitoring these changes. Furthermore, there are multiple ways to induce RBC aggregation *in-vitro* by changing the identity of the polymer used. It would be interesting to vary the aggregating conditions over a wider range of polymers and investigate the potential of PA for detecting the presence of aggregates of varying sizes or strengths.
4. Test the capabilities of commercial US imaging systems as PA devices: This will assess the potential of detecting RBC aggregation *in-vivo*. For translating the methods developed in this thesis to an *in-vivo* setting, it is likely that linear arrays will be employed for PA measurements. Many US imaging systems allow for synchronizations with the laser source and provide access to their pre-beamformed RF data. This would be advantageous for PA imaging since it would allow the user to perform signal/image processing algorithms directly on the acquired data. Further, it would be advantageous to image a flow phantom system resembling the *in-vivo* flow dynamics.

In order to demonstrate the potential of PA-RFS parameters (SS and MBF) to provide quantitative information about the physical properties of the samples being imaged, experiments

were conducted using tissue mimicking phantoms designed for PA imaging. The gelatin-based phantoms were constructed using black polystyrene beads as spherical absorbers. The gelatin powder was derived from porcine skin (Sigma-Aldrich Co., St. Louis, MO). The two types of black polystyrene beads (Polysciences Inc., Warrington, PA) had an average diameter of 0.9352 ± 0.0276 μm and 10.231 ± 0.344 μm (sizes supplied by the manufacturer). In order to prepare the phantoms, the beads were mixed with degassed water which was heated to ~80 °C prior to adding the gelatin powder. Once the powder was added, the solution was stirred until the entire gelatin had properly dissolved and a homogenous solution had formed. The solution was poured into a phantom mold container (4 cm by 4 cm by 2 cm) which was cooled to 4 °C for ~2.5 hours in order to solidify the phantom. For each phantom, 4 g of gelatin powder were mixed with 40 ml of degassed water. For each bead size, three different phantoms were made where the concentration of the beads was changed. Specifically, concentrations of 0.1, 0.2 and 0.3% (v/v) were achieved by mixing the appropriate amount of beads with the degassed water solution prior to heating. All PA measurements were performed using the Imagio small animal PA imaging device described in section 3.2.3.

The analysis of the entire dataset was performed using Matlab R2009b (The MathWorks, Inc., Natick, MA). Each PA signal recorded was multiplied by a Hamming window in order to localize the signal from the sample as well as minimize spectral leakage. The PA SA was calculated by integrating the envelope of each signal (obtained by taking the Hilbert transform). The average SA was then computed by taking the mean of all recorded signals along with the standard deviation for each phantom and the gold film. For each PA signal, the Fourier transform was computed using the Fast Fourier Transform algorithm before converted to a logarithmic (dB) scale.

The power spectra for each RF signal of each phantom were then normalized to the frequency response of the transducer. The normalization procedure was performed by subtracting

the gold film spectrum from each power spectrum. Linear regression was performed on the quasi-linear, normalized power spectra over the -6 dB bandwidth of the transducer. The SS and MBF were computed for each spectrum from the linear fit to the normalized spectrum. Averages and standard deviations of each of these parameters were computed. The normality of the data was confirmed using a Shapiro-Wilk test (with $W > 0.05$ used as the criterion for normality). An unpaired t-test was used to compare the PA signal amplitudes and spectral parameters obtained from the 1 μm and 10 μm phantoms for each concentration of beads. A *p*-value of 0.05 or less was used to establish statistically significant differences.

The PA signals and the average power spectra for the 1 and 10 μm bead phantoms are shown in **Figure 4-1**. The PA signals shown in **Figure 4-1a** and **Figure 4-1b** are representative signals from phantoms with 0.3% (v/v) bead concentration. The average power spectra of each phantom are shown in **Figure 4-1c** and the normalized average power spectra are shown in **Figure 4-1d** for 0.3% concentration. The PA signal for the 10 μm bead phantom had higher amplitude than the 1 μm bead phantom. This was reflected in the average power spectra for each phantom where the 10 μm phantom spectral power was significantly higher than the 1 μm bead phantom spectral power across all frequencies. The regression line for the normalized power spectra also showed significantly higher amplitude for the 10 μm phantom and a smaller slope.

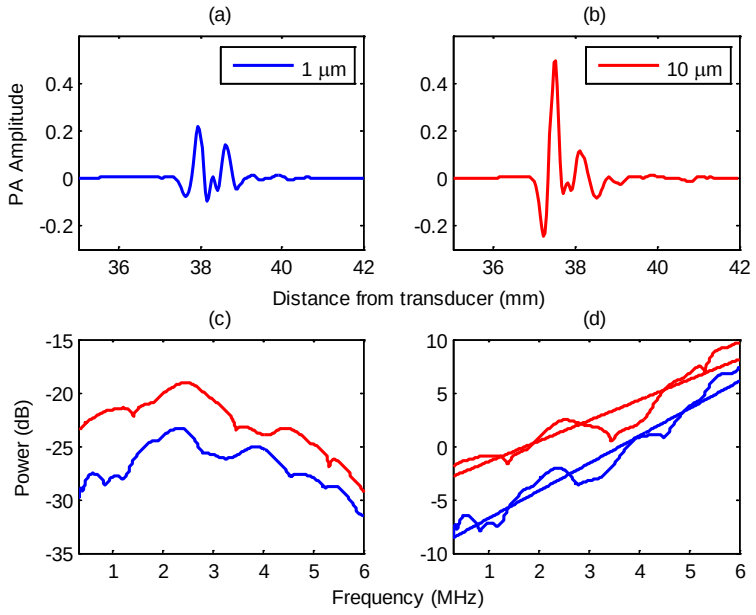


Figure 4-1: Representative PA signals for (a) 1 µm and (b) 10 µm black polystyrene phantoms along with (c) average power spectra and (d) normalized power spectra and the respective linear fits .The phantoms shown here had a 0.3% (v/v) bead concentration.

The PA SA and spectral parameters (SS and MBF) for all the phantoms constructed for this study are summarized in **Table 4-1**. For each phantom, the PA SA linearly increased with increasing concentration of beads. The PA SA was ~40% higher for the 10 µm phantom compared to the 1 µm phantom at all concentrations. This change was statistically significant ($p$ = 0.0001). The SS did not change significantly with increasing bead concentration for either phantom. The average value of the SS was 2.55 dB/MHz and 1.92 dB/MHz for the 1 and 10 µm phantoms, respectively. The decrease in SS with increasing bead size was statistically significant for all concentrations ($p$ = 0.0002). Further, the MBF linearly increased with increasing bead concentration for both phantoms. The MBF for the 10 µm phantom was statistically significantly higher than the MBF of the 1 µm phantom at all concentrations ($p$ = 0.002).

| Phantom / Parameter | 1 μm | | | 10 μm | | |
|---|---|---|---|---|---|---|
| | **0.1%** | **0.2%** | **0.3%** | **0.1%** | **0.2%** | **0.3%** |
| **SA (a.u)** | 0.13 ± 0.2 | 0.25 ± 0.1 | 0.49 ± 0.1 | 0.32 ± 0.1 | 0.63 ± 0.1 | 1.27 ± 0.3 |
| **SS (dB/MHz)** | 2.54 ± 0.1 | 2.55 ± 0.3 | 2.57 ± 0.3 | 1.93 ± 0.2 | 1.90 ± 0.1 | 1.92 ± 0.2 |
| **MBF (dB)** | -0.54 ± 0.1 | -1.04 ± 0.1 | -2.08 ± 0.2 | 0.52 ± 0.1 | 1.03 ± 0.1 | 2.05 ± 0.2 |

Table 4-1: Summary of the SA and spectral parameters (SS and MBF) for the phantom experiments.

This study demonstrates the potential of PA-RFS for monitoring the size and concentration of PA sources. The results indicate that the spectral parameters (SS and MBF) are sensitive to changes in size and concentration of the PA sources (black polyethylene beads). Although the relationship between spectral parameters and tissue properties is yet to be determined, the results from this study could be partially interpreted using what is already known from QUS characterizations of tissues [115].

As seen in **Figure 4-1** and confirmed from **Table 4-1**, the increase in the size of the optical absorber (black polyethylene beads) corresponds to an increase in the PA SA and MBF. As shown in **Eq. (1-6)**, the PA pressure in the frequency domain is proportional to the radius of the absorber squared. This suggests that larger spherical particles will emit PA pressure waves (calculated by the inverse Fourier transform of the frequency domain expression) with higher amplitude compared to smaller particles [90]. Such a trend is also observed experimentally since the PA SA for the 10 μm phantom is higher than the 1 μm phantom for all concentrations of beads (**Figure 4-1a** and **Figure 4-1b**). Furthermore, the trend of PA SA with particle size is also reflected in the MBF spectral parameter as seen by **Figure 4-1d**. The MBF increases as the particle size increases and such an increase is in accordance to the increase of PA SA. Specifically, for the 0.3% concentration, the MBF increases by ~4 dB as the size of the particle size increases. This corresponds to an increase in PA SA by a factor of ~2.6. A similar trend was observed for all other bead concentrations. This is in accordance with the relationship that exists between the structural properties of the sample and the

MBF parameter as used in UTC. In UTC, an increase in scatterer size results in increased backscatter and thus increased MBF [112]. In PA, it is the size of the absorber that dictates the increase in PA SA and MBF at the frequencies of interest. Despite the fact that the mechanism of US wave generation differs when comparing US and PA, the detection of the backscattered (US) and emitted (PA) signals is identical which suggests that spectroscopic analysis can reveal important information about the sizes and concentrations of PA sources.

As seen in **Figure 4-1d**, the SS of the line of best fit to the normalized average spectra decreases as the size of the absorber increases. This trend remains true for all concentrations of absorbers and no statistically significant changes between the SS of varying concentrations for the same absorber size were observed. Specifically, the SS decreases on average by 0.63 dB/MHz when the absorber size increases and the decrease was statistically significant for all 20 PA spectra measured for each concentration. This spectral parameter plays an important role in UTC for monitoring the size of the scatters during the presence of various types of carcinomas as well as during chemotherapeutic treatments of tumors [111], [118], [134]. A decrease in the SS parameter corresponds to an increase in the effective scatterer size. Since the size of the optical absorber dictates the frequency content of the PA power spectra, it is reasonable to expect that changes in PA SS could also be used to monitor changes in the size of the absorber [119]. This was apparent from **Figure 1-16** which showed the PA spectra for a 3 and 9 μm spheres. The peak frequency of the power spectra shifted towards the lower frequencies as the size of the sphere increased. It should be noted that **Eq. (1-6)** which predicted these PA spectra does not take into account the finite nature of the transducer bandwidth. By taking into account a transducer with a finite bandwidth, many of the frequencies present in the spectra will be filtered out due to the inherent filtering nature of US transducers [71]. Furthermore, by normalizing the spectra, transducer dependent settings during the measurement can be removed. This provides a set of parameters that can be quantitatively related to

tissue properties. The SS parameter computed in this study showed that it is a reliable parameter for monitoring the size of the optical absorber. As seen in **Table 4-1**, the SS decreased by a factor of ~0.75 when the size of the absorber increased. Such change is significant for successfully monitoring the changes in absorber size given that the concentration of absorber particles was not optimized for the resolution sensitivity of the transducer. In other words, even though the number of beads per resolution volume was not fixed to match the resolution volume of the transducer, analysis of the spectral parameters shows that PA-RFS has the potential to monitor the size and concentration of the optical absorber. Further work is required to determine the exact relationship between the PA spectral parameters and tissue microstructure, especially with regards to the geometry of the vasculature since the RBCs in blood provide the majority of the PA signals *in-vivo* [107].

The results presented here suggest that PA-RFS has the potential to monitor changes in absorber size and concentration. PA-RFS techniques are robust in the sense that they can remove all system dependencies that affect the acquisition of the PA signals and make it difficult to compare studies with different experimental conditions. The method developed here utilizes the spectral content of the PA signals and showed that the SS decreases by ~0.63 dB/MHz as the size of the absorber increased by 10 μm while the MBF increased by ~4 dB. This suggests that PA-RFS is capable of monitoring changes in size and concentration of optical absorbers and can be applied to monitor changes that occur during RBC aggregation.

# REFERENCES


[1] S. Freeman, *Biological Sciences: Second Edition*, pp. 999-1025, Pearson Education, Inc., Upper Saddle River, NJ (2005).

[2] J. E. Hall, *Guyton and Hall Textbook of Medical Physiology: Twelfth Edition*, pp. 411-413, Sanders Elsevier, Philadelphia, PA (2011).

[3] S. I. Fox, *Human Physiology: Tenth Edition*, pp. 388-431, The McGraw Hill Companies, Inc., New York, NY (2008).

[4] A. J. Vander, J. H. Sherman and D. S. Luciano, *Human Physiology: The Mechanisms of Body Function 6th Edition*, pp. 1-754, McGraw Hill, Inc., New York, NY (1997).

[5] F. T. H. Yu, "Paramétrisation de la rétrodiffusion ultrasonore érythrocytaire haute fréquence et pertinence comme facteur de risque de la thrombose veineuse ," PhD Thesis, Université de Montréal (2009).

[6] O. K. Baskurt, M. R. Hardeman, M. W. Rampling and H. J. Meiselman, *Handbook of Hemorheology and Hemodynamics*, pp. 1-455, IOS Press, Amsterdam (2007).

[7] J. H. Otto and A. Towle, *Modern Biology*, pp. 659-676, Holt, Rinehart and Winston, Inc., New York, NY (1973).

[8] G. D. O. Lowe and J. C. Barbenel, "Plasma and blood viscosity," in *Clinical Blood Rheology* Vol I, G. D. O. Lowe, Ed., pp 11-44, CRC Press, Boca Raton, FL (1988).

[9] Z.M. Ruggeri, "Platelets in atherothrombosis," *Nat Med* **8**, 1227-1234 (2002).

[10] A. Mailhac, J.J. Badimon, J.T. Fallon, A. Fernandez-Ortiz, B. Meyer, J.H. Chesebro, V. Fuster and L. Badimon, "Effect of an eccentric severe stenosis on fibrin(ogen) deposition on severely damaged vessel wall in arterial thrombosis. Relative contribution of fibrin(ogen) and platelets," *Circulation* **90**, 988-996 (1994).

[11] G.W. Schmid-Schonbein, S. Usami, R. Skalak and S. Chien, "The interaction of leukocytes and erythrocytes in capillary and postcapillary vessels," *Microvasc. Res.* **19**, 45-70 (1980).

[12] M.A. Lightman, "Rheology of leukocytes, leukocyte suspensions, and blood in leukemia. Possible relationship to clinical manifestations," *J. Clin. Invest.* **52**, 350-358 (1973).

[13] K. Rogers, ed, *Blood Physiology and Circulation*, pp. 1-233, Brittanica Education Publishing, New York, NY (2011).

[14] E. N. Marieb, ed, *Human Anatomy and Physiology*, pp. 678-943, Pearson Education, Ltd., New York, NY (2003).

[15] C. G. Caro, T. J. Pedley, R. C. Schroter and W. A. Seed, *The Mechanics of Circulation: Second Edition*, pp. 343-424, Cambridge University Press, New York, NY (2012).

[16] I. Cicha, Y. Suzuki, N. Taetishi and N. Maeda, "Changes of RBC aggregation in oxygenation-deoxygenation," *Am. J. Heart. Circ. Physiol.* **284**, H2355-H2342 (2003).

[17] CNS Clinic, Respiratory disorders, http://www.neuroicu.info/respiratorycare.htm, accessed January 10, 2012.

[18] L. Sun, H. Chen, S. Y. Zhang and H. L. Cheng, "Photodissociation of human oxy-hemoglobin studied by time-resolved photoacoustic calorimetry," *Sym. Thermophys. Properties* **15**, 1-7 (2003).

[19] Laboratory of Biorheology and Medical Ultrasonics, Ultrasonic characterization of erythrocyte aggregation, http://www.lbum-crchum.com/Web-lbum-projet%20agregation-anglais.pdf, accessed December 12, 2011.

[20] G. R. Cokelet and H. L. Goldsmith, "Decreased hydrodynamic resistance in the two phase flow of blood through small vertical tubes at low flow rates," *Circ. Res.* **68**, 1-19 (1991).

[21] O. K. Baskurt, B. Neu and H. J. Meiselman, *Red Blood Cell Aggregation*, pp. 1-304, CRC Press, Boca Raton, FL (2011).

[22] H. J. Meiselman, "Red blood cell aggregation: 45 years being curious," *Biorheology* **46**, 1-19 (2009).

[23] M. W. Rampling, H. J. Meiselman, B. Neu and O. K. Baskurt, "Influence of cell-specific factors on red blood cell aggregation," *Biorheology* **41**, 91-112 (2004).

[24] O. K. Baskurt and H. J. Meiselman, "Blood rheology and hemodynamics," *Semin. Thromb. Hemost.* **29**(5), 435-450 (2003).

[25] V. Windberger and O. K. Baskurt, "Comparative hemorheology," in *Handbook of Hemorheology and Hemodynamics*, O. K. Baskurt, M. R. Hardeman, M. W. Rampling and H. J. Meiselman, Eds. pp. 267-285, IOS Press, Amsterdam (2007).

[26] S. Shin, Y. Yang and J. S. Suh, "Measurement of erythrocyte aggregation in a microchip-based stirring system by light transmission," *Clin. Hemorheol. Micro.* **41**, 197-207 (2009).

[27] O. K. Baskurt, M. Boynard, G. C. Cokelet, P. Connes, B. M. Cooke, S. Forconi, F. Liao, M. R. Hardeman, F. Jung, H. J. Meiselman, G. Nash, N. Nemeth, B. Neu, B. Sandhagen, S. Shin, G. Thurston and J. L. Wautier, "New guidelines for hemorheological laboratory techniques," *Clin. Hemorheol. Micro.* **42**, 75-97 (2009).

[28] H. J. Meiselman, "Red-blood-cell role in RBC aggregation," *Clin. Hemorheol. Micro.* **13**, 575-592 (1993).

[29] N. Maeda, M. Seike, T. Nakajima, Y. Izumida, M. Sekiya and T. Shiga, "Contribution of gylcoproteins to fibrinogen-induced aggregation of erythrocytes," *Biochim. Biophys. Acta.* **1022**, 72-78 (1990).

[30] N. Maeda and T. Shiga, "Opposite effect of albumin on the erythrocyte aggregation induced by immunoglobulin G and fibrinogen," *Biochim. Biophys. Acta.* **855**, 127-135 (1986).

[31] M. J. Pearson and H. H. Lipowsky, "Effect of fibrinogen on leukocyte margination and adhesion in postcapillary venules," *Microcirculation* **11**, 295-306 (2004).
[32] S. Chien and K. M. Jan, "Ultrastructural basis of the mechanism of rouleaux formation," *Microvasc. Res.* **5**, 155-166 (1973).
[33] B. Neu, J. K. Armstrong, T. C. Fisher and H. J. Meiselman, "Aggregation of human RBC in binary dextran-PEG mixtures," *Biorheology* **38**, 53-68 (2001).
[34] M. Boynard and J. C. Levine, "Size determination of red blood cell aggregates induced by dextran using ultrasound backscattering phenomenon," *Biorheology* **27**, 39-46 (1990).
[35] J. K. Armstrong, R. B. Wesley, H. J. Meiselman and T. C. Fisher, "The hydrodynamic radii of macromolecules and their effect on red blood cell aggregation," *Biophys. J.* **87**, 4259-4270.
[36] F. J. Nordt, "Hemorheology in cerebrovascular diseases: approaches to drug development," *Ann. NY. Acad. Sci.* **416**, 651-661 (1983).
[37] P. Whittingstall, K. Toth, R. B. Wenby and H. J. Meiselman, "Cellular factors in RBC aggregation: effect of autologous plasma and various polymers," in *Hemorheologie et Aggregation Erythroccytaire*, J. F. Stoltz Ed. Editions Medicales Internationales, Paris (1994).
[38] D. E. Brooks, "Mechanism of red blood cell aggregation," in *Blood Cells, Rheology and Aging*, D. Platt, Ed. pp. 158-162, Springer Verlag, Berlin (1988).
[39] S. Chien, R. J. Dellenback, S. Usami, D. A. Burton, P. F. Gustavson and V. Magazinovic, "Blood volume, hemodynamic, and metabolic changes in hemorrhagic shock in normal and splenoctomized dogs," *Am. J. Physiol.* **225**, 866-879 (1973).
[40] H. Baumler, B. Neu, E. Donath and H. Kiesewetter, "Basic phenomena of red blood cell rouleaux formation," *Biorheology* **36**, 439-442 (1999).
[41] J. Janzen and D. E. Brooks, "A critical reevaluation of the nonspecific adsorption of plasma proteins and dextrans to erythrocytes and the role of these in rouleaux formation," in Interfacial Phenomena in Biological Systems, M. Bender, Ed. pp. 193-250, Marcel Dekker, New York, NY (1991). 25. B. Neu and H. J. Meiselman, "Depletion-mediated red blood cell aggregation in polymer solutions," *Biophys. J.* **83**, 2482-2490 (2002).
[42] B. Neu and H. J. Meiselman, "Sedimentation and electrophoretic mobility of human red blood cells in various dextran solutions," *Langmuir* **17**, 53-68 (2002).
[43] D. Lerche, "Electrostatic fixed charge distribution in the RBC-glycocalyx and their influence upon the total free interaction energy," *Biorheology* **21**, 477-492 (1984).
[44] M. W. Rampling, "Red cell aggregation and yield stress," in *Clinical Blood Rheology*, G. D. O. Lowe, Ed. pp. 45-64, Boca Raton, FL (1988).
[45] S. S. Raphael, *Practice of Hematology*, pp. 672-713, W. B. Saunders Co., Philadelphia, PA (1983).
[46] J. C. F. Poole and G. A. C. Summers, "Correlation of ESR in Anaemia: experimental study based on interchange of cells and plasma between normal anaemic subjects," *Brit. Med. J.* **1**, 353-356 (1952).
[47] M. Plebani and E. Piva, "Erythrocyte sedimentation rate: Use of fresh blood for quality control," *Am. J. Clin. Pathol.* **117**, 621-626 (2002).
[48] M. W. Rampling, P. Whittingstall and O. Linderkamp, "The effects of fibrinogen and its plasmin degradation products on the rheology of erythrocyte suspensions," *Clin. Hemorheol.* **4**, 533-543 (1984).
[49] M. R. Hardeman, P. T. Goedhart and N. H. Schut, "Laser-assisted optical rotational cell analyzer (LORCA); II red blood cell deformability: elongation index versus cell transit time," *Clin. Hemorheol.* **14**, 619-630 (1994).
[50] T. Alexy, R. B. Wenby, E. Pais, L. J. Goldstein, W. Hogenauer and H. J. Meiselman, "An automated tube-type blood viscometer: validation studies," *Biorheology* **42**, 237-247 (2005).
[51] O. K. Baskurt and H. J. Meiselman, "Red blood cell aggregability," *Clin. Hemorheol. Micro.* **43**, 235-247 (2009).
[52] M. W. Rampling and G. Martin, "A comparison of the Myrenne erythrocyte aggregometer with older techniques for estimating red blood cell aggregation," *Biorheology* **9**, 41-46 (1989).
[53] O. K. Baskurt and H. J. Meiselman, "Cellular determinant of low-shear blood viscosity," *Biorheology* **34**, 235-247 (1997).
[54] H. J. Meiselman and G. R. Cokelet, "Blood rheology: instrumentation and techniques," in *Flow: Its Measurement and Control in Science and Industry*, R. B. Dowdell, Ed. pp. 1337-1346, Instrument Society of America, Pittsburg, PA (1974).
[55] W. G. Zijlstra, "Syllectometry, a new method for studying rouleaux formation of red blood cells," *Acta. Physiol. Pharmacol. Neerl.* **7**, 153-154 (1958).
[56] M. R. Hardeman, J. G. G. Dobbe and C. Ince, "The laser-assisted optical rotational cell analyzer (LORCA) as red blood cell aggregometer," *Clin. Hemorheol. Micro.* **25**, 1-11 (2001).

[57] J. G. G. Dobbe, G. J. Streekstra, J. Strackee, M. C. M. Rutten, J. M. A. Stijnen and C. A. Grimbergen, "Syllectometry: the effect of aggregometer geometry in the assesment of red blood cell shape recovery and aggregation," *IEEE T. Bio-Med. Eng.* **50**, 97-106 (2003).
[58] O. K. Baskurt, M. Uyuklu, M. R. Hardeman and H. J. Meiselman, "Photometric measurements of red blood cell aggregation: light transmission versus light reflectance," *J. Biomed. Opt.* **14**(5), 054041-1-6 (2009).
[59] O. K. Baskurt, M. Uyuklu, P. Ulker, M. Cengiz, N. Nemeth, T. Alexy, S. Shin, M. R. Hardeman and H. J. Meiselman, "Comparison of three instruments for measuring red blood cell aggregation," *Clin. Hemorheol. Micro.* **43**, 283-298 (2009).
[60] A. Vaya, C. Falco, P. Fernandez, T. Contreras, M. Valls and J. Anzar, "Erythrocyte aggregation determined with the Myrenne aggregometer at two modes (M-0, M-1) and at two times (5 and 10 sec)." *Clin. Hemorheol. Micro.* **29**, 119-127 (2003).
[61] X. Xu, L. Yu and Z. Chen, "Velocity variation assessment of red blood cell aggregation with spectral domain doppler optical coherence tomography," *Ann. Biomed. Eng.* **38**(10), 3210-3217 (2010).
[62] G. Cloutier and Z. Qin, "Ultrasound backscattering from non-aggregating and aggregating erythrocytes – a review," *Biorheology* **34**(6), 443-470 (1997).
[63] J. A. Zagzebski, *Essentials of Ultrasound Physics*, pp. 1-20, Mosby Inc., St. Louis, MO (1996).
[64] K. K. Shung and G. A. Thieme, *Ultrasonic Scattering in Biological Tissues*, pp. 1-499, CRC Press, Boca Raton, FL (1993).
[65] Y. W. Yuan and K. K. Shung, "Ultrasonic backscatter from flowing whole blood I: dependence on frequency and fibrinogen concentration," *J. Acoust. Soc. Am.* **84**(4), 1195-1200 (1988).
[66] H. Kitamura and S. Kawasaki, "Detection and clinical significance of red blood cell aggregation in the human subcutaneous vein using a high frequency transducer (10 MHz): a preliminary report," *Ultrasound Med. Biol.* **23**(6), 933-938 (1997).
[67] F. T. H. Yu and G. Cloutier, "Experimental ultrasound characterization of red blood cell aggregation using the structure factor size estimator, " *J. Acoust. Soc. Am.* **122**(1), 645-656 (2007).
[68] G. Cloutier, Z. Qin, L. Durand and B. G. Teh, "Power doppler ultrasound evaluation of the shear rate and shear stress dependences of red blood cell aggregation," *IEEE T. Biomed. Eng.* **43**(5), 441-450 (1996).
[69] F. T. H. Yu, E. Franceschini, B. Chayer, J. K. Armstrong, H. J. Meiselman and G. Cloutier, "Ultrasonic parametric imaging of erythrocyte aggregation using the structure factor size estimator," *Biorheology* **46**, 343-363 (2009).
[70] E. Franceschini, F. T. H. Yu and G. Cloutier, "Simultaneous estimation of attenuation and structure parameters of aggregated red blood cell from backscatter measurements," *J. Acoust. Soc. Am.* **123**(4), EL85-EL91 (2008).
[71] T. L. Szabo, *Diagnostic Ultrasound Imaging: Inside Out*, pp. 97-135, Elsevier Academic Press, New York, NY (2004).
[72] V. Rouffiac, P. Peronneau, A. Hadengue, A. Barbet, P. Delouche, P. Dantan, N. Lassau and J. Leveson, "A new ultrasound principle for characterizing erythrocyte aggregation: in vitro reproducibility and validation," *Invest. Radiol.* **37**(8), 413-420 (2002).
[73] K. K. Shung, Y. W. Yuan, D. Fei and J. M. Tarbell, "Effect of flow disturbance on ultrasonic backscatter from blood," *J. Acoust. Soc. Am.* **75**(4), 1265-1272 (1984).
[74] R. S. C. Cobbold, *Foundations of Biomedical Ultrasound*, pp. 100-123, Oxford University Press, New York, NY (2007).
[75] M. Cabel, H. J. Meiselman, A. S. Popel and P. C. Johnson, "Contributions of red blood cell aggregation to venous vascular resistance in skeletal muscle," *Am. J. Physiol. Heart Circ. Physiol.* **272**, H1020-H1032 (1997).
[76] J. J. Bishop, P. R. Nance, A. S. Popel. M. Intaglietta and P. C. Johnson, "Effect of aggregation and shear rate on the dispersion of red blood cells flowing in venules," *Am. J. Physiol. Heart Circ. Physiol.* **283**, H1985-H1996 (2002).
[77] J. J. Durussel, M. F. Berthault, G. Guiffant and J. Dufaux, "Effects of red blood cell hyperaggregation on the rat microcirculation blood flow," *Acta. Physiol. Scand. 163*(1), 25-32 (1998).
[78] E. Piva, M. C. Sanzari, G. Servidio and M. Plebani, "Length of sedimentation reaction in undiluted blood (erythrocyte sedimentation rate): variations with sex and age and reference limits," *Clin. Chem. Lab. Med.* **39**, 451-454 (2001).
[79] H. Hammi, P. Perrotin, R. Gulliet and M. Boynard, "Determination of red blood cell aggregation in young and elderly subjects evaluated by ultrasound," *Clin. Hemorheol.* **14**, 117-126 (1994).
[80] A. Huisman, J. G. Aarnoudse, M. Krans, H. J. Huisjes, V. Fidler and W. G. Zijlstra, "Red-cell aggregation during normal-pregnancy," *Brit. J. Haematol.* **68**, 121-124 (1988).
[81] A. El-Bouhmadi, P. Boulot, F. Laffargue and J. F. Brun, "Rheological properties of fetal red cells with special reference to aggregability and dissaggregability analyzed by light transmission and laser backscattering techniques," *Clin. Hemorheol. Micro.* **22**, 79-90 (2000).
[82] O. Yalcin, A. Erman, S. Muratli, M. Bor-Kucukatay and O. K. Baskurt, "Time course of hemorheological alterations after heavy exercise in untrained human subjects," *J. Appl. Physiol.* **94**(3), 997-1002 (2003).
[83] E. Gruys, G. Toussaint, T. A. Niewold and S. J. Koopman, "Acute phase reaction and acute phase proteins," *J. Zhejiang Univ. Sc. B* **6**, 1045-1056 (2005).

[84] X. D. Weng, G. Cloutier, R. Beaulieu and G. O. Roederer, "Influence of acute-phase proteins on erythrocyte aggregation," *Am. J. Physiol. Heart Circ. Physiol.* **271**, H2346-H2352 (1996).
[85] H. J. Meiselman, "Hemorheologic alterations in hypertension: chicken or egg," *Clin. Hemorheol. Micro.* **21**, 195-200 (1999).
[86] A. B. Bell, "On the production and reproduction of sound by light," *Am. J. Sci.* **20**, 305 (1880).
[87] L. B. Kreuzer, "Ultralow gas concentration infrared absorption spectroscopy," *J. Appl. Phys.* **42**, 2934-2943 (1971).
[88] M. Xu and L. V. Wang, "Photoacoustic imaging in biomedicine," *Rev. Sci. Instrum.* **77**, 041101-1-22 (2006).
[89] C. Li and L. V. Wang, "Photoacoustic tomography and sensing in biomedicine," *Phys. Med. Biol.* **54**, R59-R97 (2009).
[90] G. J. Diebold, "Photoacoustic monopole radiation: waves from objects with symmetry in one, two and three dimensions", in *Photoacoustic Imaging and Spectroscopy*, L. V. Wang, Ed. pp. 3-17, CRC Press, Boca Raton, FL (2009).
[91] G. J. Diebold, M. I. Khan and S. M. Park, "Photoacoustic signatures of particulate matter: optical production of acoustic monopole radiation," *Science* **250**, 101-104 (1990).
[92] L. V. Wang and H. Wu, *Biomedical Optics Principles and Imaging*, pp. 1-347, John Wiley & Sons, Inc., Hoboken, NJ (2007).
[93] L. V. Wang, "Prospects of photoacoustic tomography," *Med. Phys.* **35**(12), 5758-2767 (2008).
[94] S. Y. Emelianov, P. Li and M. O'Donnell, "Photoacoustics for molecular imaging and therapy," *Phys. Today* **62**(5), 34-39 (2009).
[95] S. Hu and L. V. Wang, "Neurovascular photoacoustic tomography," *Front. Neuroenerg.* **2**(10), 1-7 (2010).
[96] G. Ku, X. Wang, G. Stoica and L. V. Wang, "Multiple-bandwidth photoacoustic tomography," *Phys. Med. Biol.* **49**, 1329-1338 (2004).
[97] L. V. Wang and S. Hu, "Photoacoustic tomography: in vivo imaging from organelles to organs," *Science* **335**, 1458-1462 (2012).
[98] R. Ma, A. Taruttis, V. Ntziachristos and D. Razansky, "Multispectral optoacoustic tomography (MSOT) scanner for whole-body small animal imaging," *Opt. Express* **17**(24), 21414-21426 (2009).
[99] T. Bowen, "Radiation-induced thermoacoustic soft tissue imaging," *Proc. IEEE Ultrasonics Symposium* **2**, 817-822 (1981).
[100] H. F. Zhang, K. Maslov, G. Stoica and L. V. Wang, "Functional photoacoustic microscopy for high-resolution and noninvasive in vivo imaging," *Nat. Biotechnol.* **24**(7), 848-851 (2006).
[101] Y. Lao, D. Xing, S. Yang and L. Xiang, "Noninvasive photoacoustic imaging of the developing vasculature during early tumor growth," *Phys. Med. Biol.* **53**, 4203-4212 (2008).
[102] R. I. Siphanto, K. K. Thumma, R. G. M. Kolkman, T. G. van Leeuwen, F. F. M. de Mul, J. W. van Neck, L. N. A. van Adrichem and W. Steenbergen, "Serial noninvasive photoacoustic imaging of neovascularization in tumor angiogenesis," *Opt. Express* **13**, 89–95 (2005).
[103] X. Wang, X. Xie, G. Ku, L. V. Wang and G. Stoica, "Noninvasive imaging of hemoglobin concentration and oxygenation in rat brain using high-resolution photoacoustic tomography," *J. Biomed. Opt.* **11**(2), 024015-1-9 (2006).
[104] R. O. Esenaliev, I. V. Larina, K. V. Larin, D. J. Deyo, M. Motamedi and D. S. Prough, "Optoacoustic technique for noninvasive monitoring of blood oxygenation: a feasibility study," *Appl. Optics* **41**(22), 4722-4731 (2002).
[105] R. O. Esenaliev, Y. Y. Petrov, O. Hartrumpf, D. J. Deyo and D. S. Prough, "Continuous, noninvasive monitoring of total hemoglobin concentration by an optoacoustic technique," *Appl. Optics* **43**(17), 3401-3407 (2004).
[106] S. Mallidi, G. P. Luke and S. Emelianov, "Photoacoustic imaging in cancer detection, diagnosis and treatement guidance," *Trends. Biotechnol.* **29**, 213-221 (2011).
[107] J. Zalev and M. C. Kolios, "Detecting abnormal vasculature from photoacoustic signals using wavelet-packet features," *Proc. SPIE* **7899**, 78992M-1-15 (2011).
[108] M. P. Patterson, C. P Riley, M. C. Kolios and W. M. Whelan, "Optoacoustic signal amplitude and frequency spectrum analysis laser heated bovine liver ex-vivo," *Proc. IEEE Ultrasonics Symposium*, 300-303 (2011).
[109] B. Soroushian, W. M. Whelan and M. C. Kolios, "Study of laser-induced thermoelastic deformation of native and coagulated ex-vivo bovine liver tissue for estimating their optical and thermomechanical properties," *J. Biomed. Opt.* **15**(6), 065002-1-10 (2010).
[110] E. Strohm, M. Rui, I. Gorelikov, N. Matsuura and M. C. Kolios, "Vaporization of perfluorocarbon droplets using optical irradiation," *Biomed. Opt. Express* **2**(6), 1432-1442 (2011).
[111] R. M. Golub, R. E. Parsons, B. Sigel, E. J. Feleppa, J. Justin, H. A. Zaren, M. Rorke, J. Sokil-Melgar and H. Kimitsuki, "Differentiation of breast tumors by ultrasonic tissue characterization," *J. Ultrasound Med.* **12**, 601-608 (1993).
[112] F. L. Lizzi, E. J. Feleppa, S. K. Alam and C. X. Deng, "Ultrasonic spectrum analysis for tissue evaluation," *Pattern Recogn. Lett.* **24**, 637-658 (2003).
[113] F. L. Lizzi, "Ultrasonic scatter-property images of the eye and prostate," *Proc. IEEE Ultrasonics Symposium* **17**, 1109-1117 (1997).

[114] F. L. Lizzi, M. Greenbaum, E. J. Feleppa, M. Elbaum and D. J. Coleman, "Theoretical framework for spectrum analysis in ultrasound tissue characterization," *J. Acoust. Soc. Am.* **73**(4), 1366-1373 (1983).
[115] F. L. Lizzi, M. Ostromogilsky, E. J. Feleppa, M. C. Rorke and M. M. Yaremko, "Relationship of ultrasonic spectral parameters to features of tissue microsctructure," *IEEE T. Ultrason. Ferr.* **33**(3), 319-329 (1986).
[116] E. J. Feleppa, F. L. Lizzi, D. J. Coleman and M. M. Yaremko, "Diagnostic spectrum analysis in ophthalmology: a physical perspective," *Ultrasound Med. Biol.* **12**(8), 623-631 (1986).
[117] E. J. Feleppa, "Ultrasonic tissue-type imaging of the prostate: implications for biopsy and treatment guidance," *Cancer Biomark.* **4**, 201-212 (2008).
[118] M. C. Kolios and G. J. Czarnota, "Potential use of ultrasound for the detection of cell changes in cancer treatment," *Future Oncol.* **5**(10), 1527-1532 (2009).
[119] A. G. Gertsch, N. L. Bush, D. C. C. Birtill and J. C. Bamber, "Towards characterizing the size of microscopic optical absorbers using optoacoustic emission spectroscopy," *Proc. SPIE* **7654**, 76541M1-10 (2010).
[120] R. Fahraeus, "The suspension stability of the blood," *Physiol. Rev.* **9**, 241-247 (1929).
[121] H. F. Harding and M. H. Kinsley, "Settling of sludge in human patients: a contribution to the biophysics of disease," *Angiology* **9**, 317-341 (1958).
[122] R. K. Saha and M. C. Kolios, "A simulation study on photoacoustic signals from red blood cells," *J. Acoust. Soc. Am.* **129**(5), 2935-2943 (2011).
[123] R. K. Saha and M. C. Kolios, "Effects of erythrocyte oxygenation on optoacoustic signals," *J. Biomed. Opt.* **16**(11), 115003-1-9 (2011).
[124] A. B. Karpiouk, S. R. Aglyamov, S. Mallidi, J. Shah, W. G. Scott, J. M. Rubin and S. Y. Emelianov, "Combined ultrasound and photoacoustic imaging to detect and stage deep vein thrombosis: phantom and ex vivo studies," *J. Biomed. Opt.* **13**(5), 054061-1-1-8 (2008).
[125] O. K. Baskurt., R. A. Farley and H. J. Meiselman, "Erythrocyte aggregation tendency and cellular properties in horse, human and rat: a comparative study," *Am. J. Physiol. Heart Circ. Physiol.* **273**, H2604 -H2612 (1997).
[126] E. L. Hinrichsen, J. Feder and T. Jossang, "Random packing of disks in two dimensions", *Phys. Rev. A* **41**, 4199-4209 (1990).
[127] Y. W. Yuan and K. K. Shung, "Ultrasonic backscatter from flowing whole blood I: dependence on shear rate and hematocrit," *J. Acoust. Soc. Am.* **84**(1), 52-58 (1988).
[128] J. G. Kim, M. Xia and H. Liu, "Extinction coefficients of hemoglobin for near-infrared spectroscopy of tissue," *IEEE Eng. Med. Biol.* **24**(2), 118-121 (2005).
[129] N. Tateishi, Y. Suzuki, I. Cicha and N. Maeda, "O2 release from erthrocytes flowing in narrow O2-permable tube: effects of erythrocyte aggregation," *Am. J. Physiol. Heart Circ. Physiol.* **281**, H448-H456 (2001).
[130] N. Tateishi, Y. Suzuki, M. Soutani and N. Maeda, "Flow dynamics of erythrocytes in microvessels of isolated rabbit mesentery: cell-free layer and flow resistance," *J. Biomech.* **27**(9), 1119-1125 (1994).
[131] N. Tateishi, N. Maeda and T. Shiga, "A method for measuring the rate of oxygen release from single microvessels," *Circ. Res.* **70**, 812-819 (1992).
[132] Y. S. Chen, W. Frey, S. Aglyamov and S. Emelianov, "Environment-dependent generation of photoacoustic waves from plasmonic nanoparticles," *Small* **8**(1), 47-52 (2012).
[133] M. Rui, W. Bost, E. C. Weiss, R. Lemor and M. C. Kolios, "Photoacoustic microscopy and spectroscopy of individual red blood cells," in *Biomedical Optics, OSA Technical Digest (CD) (Optical Society of America)*, paperBSuD93 (2010).
[134] J. Mamou, A. Coron, M. Hata, J. Machi, E. Yanagihara, P. Laugier and E. J. Feleppa, "Three-dimensional high-frequency characterization of cancerous lymph nodes," *Ultrasound Med. Biol.* **36**(3), 361-375 (2010).